

**COHERENCE PROPERTIES OF SUPERCONTINUUM GENERATED IN
HIGHLY NONLINEAR PHOTONIC CRYSTAL FIBERS**

A dissertation

submitted by

Yuji Zhang

In partial fulfillment of the requirements

for the degree of

Doctor of Philosophy

In

Physics

TUFTS UNIVERSITY

February 2015

ADVISOR:

Prof. Fiorenzo G. Omenetto

Tufts University, Department of Physics and Astronomy
and Department of Biomedical Engineering

RESEARCH COMMITTEE:

Prof. Peggy Cebe

Tufts University, Department of Physics and Astronomy

Dr. Daniel J. Kane

Mesa Photonics, LLC, Santa Fe, NM

Prof. Anthony W. Mann

Tufts University, Department of Physics and Astronomy

Prof. Austin Napier

Tufts University, Department of Physics and Astronomy

Prof. Krzysztof Sliwa

Tufts University, Department of Physics and Astronomy

Prof. Roger G. Tobin

Tufts University, Department of Physics and Astronomy

This page is intentionally left blank.

ACKNOWLEDGEMENTS

I would like to first of all thank my advisor Professor Fiorenzo Omenetto for his financial support, academic guidance, and also his help in experiment and in writing. Without those I would not have made my progress in research. He is so acute and fast in thinking, and discussing with him and listening to his discussion is the best part of the training I received in the graduate school. Looking at his bench work and his lab notebook, I saw a perfect example of a precise, careful, and neat style, which I have been trying to mimic. His influence on me has been more than just in research. He illustrates such a passionate and indulgent attitude in work, just like his words: “It’s not about here (pointing to his head) – it’s all about here (pointing to his heart).” It has been my privilege to work with him and learn science and beyond.

I would like to thank my committee members. Dr. Daniel Kane has been so kind to share his expertise and insights. I call him every several weeks and always benefit from his advice. Professor Roger Tobin gave me lessons about writing, presentation, and also generally about research. He read my thesis draft in short time and gave revision and comments before my defense, so that I could improve my defense based on this feedback. Professor William Oliver and Professor Krzysztof Sliwa spent their time to listen to my trial defense and gave me advice on presentation, especially about how to make it interesting to broader audience. As my academic advisor, Professor Krzysztof Sliwa helped in my academic and personal life in my first a few years in the States. Professor William Oliver sent me to ESL class. In those early days in the States when I was not so comfortable and confident, their help was invaluable. Professor Anthony Mann is the

person I always have casual talks with and learn from. Professor Peggy Cebe shared with me very useful tips about organizing and managing research. Professor Austin Napier revised my thesis so carefully and even found a missing paper in the reference. I feel lucky to have such smart and kind committee members who are willing to share and help.

My labmates are fun to work with and also helpful. Dr. Jason Amsden was my mentor when I started working in the lab. He shared his techniques and experience to get me started. Without his help, it would have taken me longer to figure out the hands-on techniques he taught me. Late Dr. Peter Domachuk also shared with me his expertise and experience. Dr. Jessica Mondia and Mr. Jason Bressner gave me good suggestions about research and about personal life. Dr. Hu “Tiger” Tao and Ms. Miaomiao “Mia” Tao have deep understanding about research, and I often discussed with them about the stories of papers. Mr. Matthew Applegate helped me a lot in writing. Writing in second language English has been challenging for me. I always ask him for help in revision. He probably has read my journal papers ten times. Other labmates are also nice to discuss with and willing to help, including Dr. Giovanni Perotto, Dr. Sunghwan Kim, Dr. Jana Kainerstorfer, Dr. Benedetto Marelli, Dr. Konstantinos Tsioris, Dr. Elijah Shirman, Mr. Alex Mitropoulos, Mr. Mark Brenckle, Mr. Jonas Osorio, and Mr. Joshua Spitzberg.

I also want to thank Professor David Kaplan and Dr. Guokui Qin in Department of Biomedical Engineering and Professor Subhas Kundu from Indian Institute of Technology Kharagpur for opportunities to collaborate, so that I could have chances to work with interesting rare materials and produce some publications. Dr. Martin Hunter in Department of Biomedical Engineering and my friends Dr. Robert Stegeman and Dr.

Guang-ming “Derek” Tao are experts in relevant fields. I often talk to them and benefit from the discussions.

Staff are sometimes less visible than professors, but are really indispensable. Ms. Milva Ricci, Ms. Keleigh Sanford, and Ms. Carmen Preda in Department of Biomedical Engineering and Ms. Gayle Grant, Ms. Shannon Landis-Amerault, Ms. Jacqueline DiMichele, and Ms. Jean Intoppa in Department of Physics and Astronomy helped me with all kinds of support. Mr. Scott MacCorkle and Mr. Denis Dupuis in the machine shop made me gadgets that made experiments easy and fun.

My parents Jianfa Zhang and Meifeng Fan Zhang always have so much love for me. They provided an atmosphere of study where I developed a will of pursuing more and deeper knowledge. And they have been so supportive during the years when I am away from them. My girlfriend Mengyi Liao is a pretty and smart girl. She has been supportive and also giving me good suggestions. I owe a lot of thanks and love to them.

This page is intentionally left blank.

ABSTRACT

In this dissertation, experimentally measured spectral and coherence evolution of supercontinuum (SC) is presented. Highly nonlinear soft-glass photonic crystal fibers (PCF) were used for SC generation, including lead-silicate (Schott SF6) PCFs of a few different lengths: 10.5 cm, 4.7 mm, and 3.9 mm, and a tellurite PCF of 2.7 cm. The pump is an optical parametric oscillator (OPO) at 1550 nm with pulse energy in the order of nanojoule (nJ) and pulse duration of 105 femtosecond (fs). The coherence of SC was measured using the delayed-pulse method, where the interferometric signal was sent into an optical spectrum analyzer (OSA) and spectral fringes were recorded. By tuning the pump power, power-dependent evolution of spectrum and coherence was obtained.

Numerical simulations based on the generalized nonlinear Schrödinger equation (GNLSE) were performed. To match the measured data, the simulated spectral evolution was optimized by iteratively tuning parameters and comparing features. To further match the simulated coherence evolution with the measurement, shot noise and pulse-to-pulse power fluctuation were added in the pump, and the standard deviation of the fluctuation was tuned.

Good agreement was obtained between the simulated and the measured spectral evolution, in spite of the unavailability of some physical parameters for simulation. It is demonstrated in principle that, given a measured spectral evolution, the fiber length, and the average power of SC, all other parameters can be determined unambiguously, and the spectral evolution can be reproduced in the simulations. Most importantly, the soliton fission length can be simulated accurately.

The spectral evolution using the 4.7- and the 3.9-mm SF6 PCFs shows a pattern dominated by self phase modulation (SPM). This indicates that, these fiber lengths are close to the soliton fission length at the maximum power. The spectral evolution using the 10.5-cm SF6 PCF and the 2.7-cm tellurite PCF shows a soliton-fission-dominated pattern, indicating these lengths are much longer than the soliton fission length at the maximum power.

For the coherence evolution using the SF6 PCFs, the simulations and the measurements show qualitative agreement, confirming the association between coherence degradation and soliton fission. For the case of the tellurite PCF, nearly quantitative agreement is shown, and it is shown that the solitonic coherence degrades slower than the overall coherence.

Fluctuation of coherence occurs at the regime where the coherence starts to degrade, in the measurement and the simulations of the SF6-PCF case. It is shown that the cause is the pulse-to-pulse power fluctuation in the pump.

The pulse-to-pulse stability of spectral intensity is another characterization of SC stability, other than the coherence. It is shown by simulations that these two exhibit different dynamics, and have low correlation.

TABLE OF CONTENTS

ACKNOWLEDGEMENTS.....	iii
ABSTRACT.....	vii
TABLE OF CONTENTS.....	ix
LIST OF TABLES.....	xii
LIST OF FIGURES.....	xiii
LIST OF APPENDICES.....	xix
ABBREVIATIONS AND ACRONYMS.....	xx
1. INTRODUCTION.....	1
2. SUPERCONTINUUM GENERATION AND COHERENCE.....	4
2.1 Photonic Crystal Fiber.....	5
2.2 Modeling of Supercontinuum Generation.....	6
2.2.1 The generalized nonlinear Schrödinger equation.....	6
2.2.2 The dispersion term.....	11
2.2.3 The Raman term.....	14
2.2.4 Implementation of numerical simulation.....	21
2.3 Major Physical Processes in Supercontinuum Generation.....	22
2.3.1 Kerr effect and self phase modulation.....	22
2.3.2 Dispersion.....	23

2.3.3 Soliton and soliton fission	26
2.3.4 Intrapulse Raman scattering	29
2.3.5 Dispersive wave (Cherenkov radiation) generation	31
2.4 Measurement of Coherence.....	32
2.4.1 Coherence of quasi-monochromatic light.....	32
2.4.2 Coherence of broadband light.....	35
2.4.3 Coherence of SC.....	37
3. BACKGROUND	39
3.1 Simulation Research of SC Coherence	40
3.2 Experimental Research of SC Coherence	46
3.3 My Research.....	50
4. METHODS	51
4.1 Experiment	52
4.2 Simulation	57
4.2.1 Introduction	57
4.2.2 The dispersion term	58
4.2.3 The Raman term	60
4.2.4 Simulation parameters	63
4.2.5 Modeling noise and coherence	64
5. RESULTS AND DISCUSSIONS.....	69

5.1 Results Using SF6 PCFs	70
5.1.1 Experimental results	70
5.1.2 Simulated spectral evolution and discussions	73
5.1.3 Simulated coherence and discussions	82
5.1.4 Conclusions	89
5.2 Using Tellurite PCF	90
5.2.1 Experimental data	90
5.2.2 Simulated spectral evolution and discussions	91
5.2.3 Simulated coherence evolution and discussions	95
5.2.4 Conclusions	99
6. CONCLUSIONS AND OUTLOOK	101
REFERENCES	104
APPENDIX A. SYSTEMATIC CHECK OF NUMERICAL SIMULATIONS	109
APPENDIX B. PARAMETERS FOR SIMULATIONS IN SECTION 2.3.....	110
APPENDIX C. COMPUTER CODE FOR DATA PROCESSING AND NUMERICAL SIMULATIONS	111

LIST OF TABLES

- 2.1 Comparison of media for supercontinuum (SC) generation.
- 2.2 Brief derivation of the generalized nonlinear Schrödinger equation (GNLSE).
- 2.3 Definition of the variables and the parameters in the GNLSE.
- 3.1 Summation of previous simulation research and their theories.
- 3.2 Key facts of previous experimental research on SC coherence.
- 4.1 Parameters of the PCFs and the pump used in the experiment, in comparison with a silica PCF and a SF6 PCF in literature.
- 4.2 Polynomial fitting of the $\beta_2(\omega-\omega_0)$ curve for the 3.6- μm -core SF6 PCF.
- 4.3 Polynomial fitting of the $\beta_2(\omega-\omega_0)$ curve for the tellurite PCF.
- 4.4 Comparison of two Raman gain spectra: g_{R1} reported in [Plotnichenko et al., 2005] and g_{R2} reported in [Stegeman et al., 2006; Qin et al., 2007; Yan et al., 2010], and calculation of the Raman term.
- 4.5 Values of parameters for simulation (subject to change in the optimization process).
- B.1 Parameter values for each simulation in Fig. 2.1 and 2.2.

LIST OF FIGURES

- 2.1 Spectral and temporal evolution when different GVD is added to SPM. (a) SPM + normal GVD. The normal GVD limits the spectral broadening. (b) SPM + anomalous GVD. The pulse swings back and forth between spectrally-broader-temporally-shorter and spectrally-narrower-temporally-longer. This is a higher-order soliton propagating periodically (see Section 2.3.3). (c) SPM + a particular value of anomalous GVD such that they perfectly balance each other. In this case the pulse keeps invariant in spectrum and in temporal profile. This is a fundamental soliton (see Section 2.3.3).
- 2.2 (a) Adding the Raman term causes soliton fission. The spectral trajectory and temporal trajectory of a soliton are marked. The soliton fission length $L_{fiss} = 0.48$ cm is marked with white arrows. It can be seen this distance is where the pulse reaches the maximum spectral width and the shortest duration before splitting, which is consistent with this empirical definition of soliton fission length. (b) Further adding 3rd-order dispersion causes dispersive wave (Cherenkov radiation) in addition to soliton fission. The dispersive wave is marked in spectral and temporal evolution.
- 2.3 Experiments of coherence measurement. (a) Young's double slit experiment, and (b) Michelson interferometry.
- 2.4 Methods to measure frequency-dependent coherence for broadband light. (a) Interference of broadband light yields overlapped fringes of all frequencies. (b) Spectrally resolve the signal along the direction of fringes (here vertically) to obtain a 2D pattern. At horizontal line is the fringe of a frequency. (c) Spectrally resolve the fringes in the direction perpendicular to the fringes (here horizontally), resulting in a spectrum with fringes. Prisms are used to conceptually illustrate spectrally resolving the signal.
- 3.1 Simulation results of SC coherence, excerpted from [Dudley et al., 2006]. (a) and (b): Spectral and coherence evolution using a 100-fs and a 150-fs pump, respectively. The pump peak power is 10 kW. The ZDW of the PCF is 780 nm, and the pump wavelength is 835 nm (anomalous GVD pump). (c) Contour plot of average coherence as a function of the pump wavelength and the pump pulse duration. The pump peak power is fixed to be 4 kW. The ZDW of the PCF is 780 nm (marked with a dash line). (d) Average coherence vs. soliton number N , summarized from multiple simulations using various parameter sets, in which the

- pump wavelength is ranged 790–900 nm, pump pulse duration is 30–200 nm, and pump peak power is 3–30 kW.
- 3.2 Simulated SC and its coherence, excerpted from [Türke et al., 2007]. A 410-fs pump at 775 nm was used, and the pump peak powers are (a) 0.09 kW, (b) 0.9 kW, and (c) 5.9 kW. The fiber length is 9 cm. The authors argued that in the case of (c), the MI-induced sidebands are weak when soliton fission happens, and the ejected solitons are coherent.
 - 4.1 SEM picture of the cross section of the highly nonlinear SF6 PCF. Inset is a close-up of the core. The core diameter is 3.6 μm .
 - 4.2 Microstructure and the dispersion of the Tellurite PCF. (a) Cross section of the fiber under an optical microscope. (b) and (c) are closeups of the core under SEM and under an optical microscope, respectively. (d) is the dispersion curve. The ZDW is 1380 nm. These figures are excerpted from [Domachuk et al., 2008].
 - 4.3 Experimental setup for the measurement of SC coherence.
 - 4.4 1-mm SF6 PCF mounted on a customized stage using tape.
 - 4.5 Calculation of the dispersion of the SF6 PCF. (a) Calculating the dispersion curve of the 3.6- μm -core PCF based on the dispersion curves of a 2.6- μm and a 4- μm -core SF6 PCFs, through linear interpolation. The 2.6- μm and the 4- μm -core curves are excerpted from [Kumar et al., 2002]. (b) Linear curve fitting of $\beta_2(\omega - \omega_0)|_{3.6\text{-}\mu\text{m}}$.
 - 4.6 Raman response function $h_R(t)$ of SF6. It is modeled as Eq. 2.2.61, with $\tau_1 = 5.5$ fs, $\tau_2 = 32$ fs, and $f_R = 0.13$.
 - 4.7 (a) Raman gain spectra $g_R(\omega)$ of tellurite glasses. The green curve g_{R1} was reported in [Plotnichenko et al., 2005], and the blue curve g_{R2} was reported in [Stegeman et al., 2006; Qin et al., 2007; Yan et al., 2010]. Both are calibrated for pump wavelength $\lambda_0 = 514.5$ nm. (b) Raman response function $h_R(t)$ calculated based on g_{R2} , using Eq. 2.2.57.
 - 5.1 Spectral evolution (a)–(c) and coherence evolution (d)–(f) of SC generated in three different lengths of SF6 PCFs (10.5-cm, 4.7-mm, and 3.9-mm). The red arrows in (a) mark soliton trajectories. The green arrow in (b) marks the Cherenkov peak. The spectral evolution is calibrated such that the maximum intensity is 0 dB. The lower limit of the color bar is set to -40 dB so that the 40-

dB bandwidth is visualized in the evolution; the upper limit is set for optimal visualization of features. (g)–(i) are line plots of representative spectra.

- 5.2 (a)–(c) Experimentally measured spectral evolution using three different lengths of SF6 PCF, respectively. (d)–(f) Corresponding simulation results. The vertical black line at 1700 nm helps visually comparing with the experimental data. (g) and (h): Simulated spectral and temporal evolution depending on the propagation length. $P = 77$ mW is used. It is shown graphically that soliton fission happens at ~ 9 mm. Analytically calculated soliton fission length is similar $L_{fiss} = 10.2$ mm. (i) GVD $D(\lambda)$ of the fiber. The red lines mark the zero dispersion wavelength (ZDW) and the pump wavelength (1550 nm). The ZDW is ~ 1370 nm. The GVD at the pump wavelength is ~ 38 ps/(nm·km).
- 5.3 Determining the duration of the pump pulses. Red curve: measured output spectrum at $P = 2$ mW and $L_{fiber} = 3.9$ mm. Black curves: simulated output spectrum using a pump of transform-limited sech^2 pulses of $T_{FWHM} = 100, 110,$ and 120 fs, respectively. $P = 2$ mW and $L_{fiber} = 3.9$ mm are used.
- 5.4 Optimization of the simulated spectral evolution. Each line includes four plots of spectral evolution: the beginning (low power) part of the 10.5-cm-fiber case, the 10.5-cm-fiber case, the 4.7-mm-fiber case, and the 3.9-mm-fiber case. (a) Experimental data. (b) Simulations with $T_{FWHM} = 105$ fs has been applied. (c) Simulations after further tuning P to $1.3*P$ and γ to $1.38*\gamma$. (d) Simulations after further tuning $\beta_2(\omega)$ to $2*\beta_2(\omega)$.
- 5.5 Simulated spectral evolution with varying initial chirps, in the case of the 4.7-mm SF6 PCF. Adding positive or negative initial chirps causes features in the spectra, and changes the power at which soliton fission happens. Emergence of the Cherenkov peak is marked with red lines to represent the powers at which soliton fission happens.
- 5.6 Comparison between (a) the measured spectral evolution and (b)–(d) corresponding simulations using varying initial chirps, for the case of the 3.9-mm SF6 fiber. (a) shows gaps (marked with arrows) between the central peak and the spectral lobes. (b) and (c) also have these gaps, while in (d) a positive chirp ($C = 0.1$) flattens the central parts of the spectrum and causes the gaps to disappear. Spectra at $P = 40$ mW are stacked in (e) to show the features clearly.
- 5.7 Comparison of the broadening trends at the beginning (low SC power) part of the spectral evolution. The case of 3.9-mm SF6 PCF is used. Output spectra at $P = 2, 4, 6, 8, 10, 12, 14, 16, 18,$ and 20 mW are stacked in each plot. The simulations

with initial chirp = -0.2 and -0.1 show narrowing or lack of broadening. This is not seen in the experiments. So the chirp in the experiment was > -0.1 .

- 5.8 Simulated coherence of SC generated in three different lengths of SF6 PCFs, in comparison with the experimental results. Column (a): three plots of measured spectral evolution using different fiber lengths. Column (b): measured coherence evolution. Column (c): simulated spectral evolution. Column (d): simulated coherence evolution. The simulation plots have black lines at 1700 nm to help visual comparison with experiments. In the experiment, radiation of relative intensity lower than about -40 dB was not measurable due to the sensitivity limitation; and in the simulations this part of radiation was also ignored. (e) and (f): spectrally-averaged coherence as functions of the average SC power. In the simulations, shot noise and 5% pulse-to-pulse power fluctuation in the pump were added. In (a), the color bars for the 10.5-cm and the 4.7-mm cases are omitted for clarity, and can be found in Fig. 5.1. In (b)–(d), each color bar works for three plots in the column.
- 5.9 Comparison between pulse-to-pulse stability of spectral intensity ($-C_V$) and coherence. (a) Power-dependent evolution of $-C_V$, using the 4.7-mm SF6 PCF. This can be compared with the 4.7-mm coherence evolution in Fig. 5.8 (d). (b) The spectral evolution, (c) the evolution of coherence $|g|$, and (d) the evolution of $-C_V$ depending on the propagation length, using a 5-cm SF6 PCF and an average power of 70 mW. (e) Averaged coherence $|g|$ (blue), phase stability $|g_{PHASE}|$ (red), and $-C_V$ (green) as functions of the propagation length. The soliton fission length (4.8 mm) is marked with a dashed line. (f) Distribution of SC radiation as a function of $|g|$ and $-C_V$, where the radiation at all the lengths in (b) is included. (g) Distribution of SC radiation as a function of $|g_{PHASE}|$ and $-C_V$.
- 5.10 (a) Measured coherence evolution of the 3.9-mm-fiber case. (b) Simulated coherence with independent noise at each power, including shot noise and pump power fluctuation Δ_P . (c) Simulation result by fixing shot noise (meaning using same shot noise at each power). (d) and (e) are two runs of simulation by fixing Δ_P (meaning using same set of Δ_P at each power). (d) and (e) use different sets of Δ_P (as in the histograms) and thus have different coherence. These results show that the randomness of Δ_P is the cause of the coherence fluctuation.
- 5.11 (a), (b): Measured spectral and coherence evolution of SC generated in a 2.7-cm tellurite PCF. (c) Spectrally-averaged coherence of the whole measured spectrum (800–1700 nm, red curve) and of the solitonic region (1550–1700 nm, blue curve). (d), (e): Closeup spectral and coherence evolution for the solitonic region. Solitons and corresponding high-coherence traces are marked with arrows (1–7).

Each pair of arrows is placed at the same places in the plots, showing the correspondence between the solitons and the high-coherence traces.

- 5.12 Optimization of the simulated SC spectrum by tuning the dispersion. (a) Measured SC spectrum, excerpted from [Domachuk et al., 2008]. 8-mm tellurite PCF was used. (b) Tests with varying slopes in the dispersion curve. The red-color part of the curve was experimentally measured [Domachuk et al., 2008]. The green circles mark estimated corner part (1600–2200 nm). The remaining parts are assumed to be linear (green lines). (c) Simulated SC spectra using the dispersion curves in (b). Changing the slope of the linear part of the dispersion in (b) causes shifting of some spectral peaks in (c) (see red arrows). (d) The dispersion curve for the optimized spectrum in (e). The dispersion at the pump wavelength is 76.2 ps/(nm·km). ZDWs are 1382 and 2528 nm. (e) Measured SC spectrum [Domachuk et al., 2008] vs. the optimized simulation using the dispersion curve in (d). The criterion of optimization is matching the reddest (~900 nm) and the bluest (~4700 nm) peaks, respectively. These two peaks are marked with red arrows. Green arrows mark some of the spectral features that match.
- 5.13 Comparison of (a), (c) measured and (b), (d) simulated spectral evolution using the 2.7-mm tellurite PCF. (c) and (d) are closeups of the beginning (low SC power) stage, showing the first a few solitons and the emergence of the Cherenkov radiation. The lower and the upper limits of the color bar are set for visualization of features.
- 5.14 (a)–(d) Measured and (e)–(h) simulated spectral and coherence evolution of SC generated in the 2.7-cm tellurite PCF. The plots in the second line ((c), (d), (g), and (h)) are closeups of the solitonic region (1550–1700 nm). The pump wavelength is marked with black lines. Arrow pairs 1–7 and A–E mark soliton trajectories (in (c) and (g)) and corresponding high-coherence traces (in (d) and (h)). (i) and (j) show spectrally-averaged coherence of the whole measured spectrum (800–1700 nm, red curves) and of the solitonic region (1550–1700 nm, blue curves). The dashed curves in (i) show average coherence based on the measured coherence and the simulated spectra. Shot noise and 5% pulse-to-pulse power fluctuation in the pump were used in the simulations.
- 5.15 Simulated spectral and coherence evolution of SC generated in a 2.7-cm tellurite PCF. (a) is a reminder of the GVD. (b) and (c) are evolution depending on the SC power. (d) and (e) are evolution depending on the propagation length ($P = 71.4$ mW). Shot noise and 5% fluctuations of the pump power were added.

A.1 A systematic check of the simulations of SC and its coherence. (a) and (b) are results excerpted from [Dudley et al., 2006]. (c) and (d) are my results using the same parameters.

LIST OF APPENDICES

- A Systematic check of numerical simulations
- B Parameters for simulations in Section 2.3
- C Computer code for data processing and numerical simulation

ABBREVIATIONS AND ACRONYMS

c.c.	complex conjugate
GVD	group velocity dispersion
GNLSE	generalized nonlinear Schrödinger equation
MI	modulation instability
OPO	optical parametric oscillator
OSA	optical spectrum analyzer
ODE	ordinary differential equation
PCF	photonic crystal fiber
RIFS	Raman-induced frequency shift
SC	supercontinuum
SMF	single mode fiber
SPM	self-phase modulation
XPM	cross-phase modulation
ZDW	zero (group velocity) dispersion wavelength

1. INTRODUCTION

Supercontinuum (SC) generation is the process by which narrow-band incident light spectrally broadens to typically hundreds of nm (40-dB bandwidths). It is usually a complex interaction of several linear and nonlinear processes, e.g., self phase modulation (SPM), dispersions especially group velocity dispersion (GVD), modulation instability (MI), soliton fission, the Raman effect, dispersive wave (Cherenkov radiation) generation. In order to stimulate nonlinear effects, the incident light must be very intense. Ultrafast lasers are usually used as the pump because of their high instantaneous intensity. Photonic crystal fibers (PCF) are popular media for SC generation, primarily because of their high nonlinearity and engineerable dispersion. A review of SC generation in PCFs can be found in [Dudley et al., 2006; Genty et al., 2007].

Whether the pulse-to-pulse coherence of the ultrafast laser can be maintained in the complex process of SC generation is an interesting topic, and is important for many applications such as frequency comb [Udem et al., 2002; Cundiff and Ye, 2003] and pulse compression [Dudley and Coen, 2004; Schenkel et al., 2005; Heidt et al., 2011].

Numerical and experimental studies have been carried out on SC coherence. Simulations have shown that noise can be amplified in SC generation, causing pulse-to-pulse fluctuation in phase, thus coherence degradation. Coherence properties depending on various parameters have been discussed. Spectral and coherence evolution has been useful for visualization. They are contour plots of intensity/coherence vs. wavelength vs. a tuning variable such as the SC power or the propagation length. Spectral evolution

visualizes various processes in SC generation, and corresponding coherence evolution visualizes coherence dynamics.

Most experimental research of SC coherence, however, has shown coherence measured under limited conditions (e.g., at several levels of SC power), which are unable to show evolving trends and some subtle features. This limits detailed discussion, for example, about the correspondence between coherence properties and broadening mechanisms. Discussions in a lot of previous experimental research are based on average coherence.

In this dissertation, experimentally measured spectral and coherence evolution of SC is presented. Numerical simulations were performed to match the measured data. Rich features in the spectral evolution allow for detailed comparison between measurement and simulation. By iteratively tuning parameters and comparing features, the simulations can be optimized to match the measurement.

PCFs of different lengths were used to investigate dependence of coherence on the fiber length. Previous simulations [Dudley et al., 2006] have shown that coherence degradation is associated with the process that the pulse splits into smaller pulses in time (soliton fission). This splitting process happens at a certain propagation length (soliton fission length). Using fibers shorter than this length, broadening is mainly based on SPM which is a coherence-maintaining process, hence coherent SC is produced.

Two types of highly nonlinear soft-glass PCFs were used: a lead-silicate (Schott SF6) PCF and a tellurite PCF. Many soft glasses have much higher nonlinear refractive indices than the conventional material fused silica, and have been used for ultrabroad SC generation [Price et al., 2007; Tao et al., 2012]. For example, a SF6 PCF of different

microstructure than the ones used in my experiment [Omenetto et al., 2006] and the same tellurite PCF as used here [Domachuk et al., 2008] were used to generate SC as broad as ~3000 nm and ~4000 nm, respectively. SC of smooth spectrum based mainly on SPM has been obtained using short fiber lengths [Omenetto et al., 2006; Moeser et al., 2007]. High coherence is expected in this SPM-dominating case, which would be tested in my experiment.

This thesis is organized as follows:

Ch 2 reviews the knowledge needed to understand this dissertation. It begins by introducing the PCF and its advantage in SC generation. Then modeling of SC generation is introduced, and various physical processes happening in SC generation are discussed. Lastly the fundamentals of coherence are reviewed.

Ch 3 reviews previous research about SC coherence, and then introduces the motivation of my research.

Ch 4 describes methods of experiment and simulation.

Ch 5 presents results and analysis. Experimental data are presented first. Then simulations are optimized to match the experimental results. The physical meaning of the results is then discussed.

Ch 6 concludes this dissertation and presents an outlook for future work.

2. SUPERCONTINUUM GENERATION AND COHERENCE

SUMMARY

This chapter refreshes the textbook knowledge needed for understanding the research in this dissertation.

Section 2.1 introduces the photonic crystal fiber (PCF), a popular medium for supercontinuum (SC) generation. Compared to other media, the advantages of the PCF are its enhanced light confinement, controllable dispersion, and single mode profile.

Section 2.2 introduces numerical modeling of SC generation using the generalized nonlinear Schrödinger equation (GNLSE). Derivation of this equation is briefly reviewed so that the physical meaning of each term is clear. Calculation of the dispersion term and the Raman term is discussed, because researchers usually need to calculate them for their specific fiber. Details of the implementation of numerical simulation are then introduced.

Section 2.3 discusses major processes that happen in SC generation. SC generation is usually a mixture and interaction of a few nonlinear and linear processes. It is possible to isolate each of them, and associate them to features in the spectrum and the temporal profile of SC.

Section 2.4 refreshes the theory and the experiments of coherence.

2.1 Photonic Crystal Fiber

The PCF [Russell, 2003; Knight, 2003; Russell, 2006] is an optical fiber with an array of air holes, usually periodic, surrounding its core and running along its length. Here we focus on the solid-core PCF. The microstructure area can be considered a cladding of an effective refractive index much lower than the core. Light is guided in the core based on modified total internal reflection [Birks et al., 1997].

The PCF is regarded as the “driving force” for SC generation [Dudley and Taylor, 2010]. It has some advantages compared to other media such as bulk material [Alfano and Shapiro, 1970a and 1970b.] and tapered fibers [Birks et al., 2000] (Table 2.1).

(1) It has enhanced light confinement and hence high nonlinearity. Bulk materials do not confine light tightly as fibers do. Self focusing is usually needed for SC generation in bulk materials, which requires high pulse energy usually in the order of mJ. Single mode fibers (SMF) confine light in a $\sim 8\text{--}10\ \mu\text{m}$ core. The cores of PCFs and the waists of tapered fibers are usually a few μm in diameter, yielding enhanced confinement.

(2) Dispersion plays an important role in SC generation (see Section 2.2 and 2.3). Generally, if the pulse spreads out in time too quickly, it becomes less intense, and then nonlinear broadening is limited. To prevent that, the medium should have either a small dispersion or a dispersion that counterbalances the chirp caused by nonlinear effects. Bulk material and SMFs often have unwanted dispersion properties; whereas dispersion properties are controllable by engineering the microstructure of the PCF or by precisely controlling the tapering geometry of the tapered fiber.

(3) SC generation in bulk material often shows complicated filament forms; while SMFs, PCFs, and tapered fibers are usually single mode.

Media Properties	Bulk material	Single mode fiber (SMF)	Tapered fiber	PCF
(1) Light confinement	Self-focusing required.	~8–10 μm core, Small Δn , Small N.A..	Usually a few μm core, Large Δn , Large N.A..	
(2) Dispersion	Not controllable		Controllable	Controllable (more degrees of freedom than tapered fiber)
(3) Mode	Usually filaments	Usually single mode		

Table 2.1 Comparisons of media for SC generation. Δn is the refractive index contrast between the core and the cladding. N.A. = numerical aperture.

2.2 Modeling of Supercontinuum Generation

2.2.1 The generalized nonlinear Schrödinger equation

The axial propagation of light in fibers is described by the generalized nonlinear Schrödinger equation (GNLSE). The brief derivation procedure is in Table 2.2. This section is reorganized from textbooks [Dudley and Taylor, 2010; Agrawal, 2006].

We begin by defining the electric field in the time domain:

$$\vec{E}(\vec{r}, t) = \hat{x}E(\vec{r}, t)\exp(-i\omega_0 t) \quad (2.2.1),$$

where $E(\vec{r}, t)$ is the slowly-varying complex amplitude. \hat{z} is the axis direction of the fiber and the propagation direction of light. \hat{x} is the polarization direction, which can be omitted in the following, because all fields are in \hat{x} direction under the scalar assumption.

The frequency domain representation is

$$\tilde{E}(\vec{r}, \omega - \omega_0) = FT \{E(\vec{r}, t)\} = \int_{-\infty}^{\infty} E(\vec{r}, t) \exp[i(\omega - \omega_0)t] dt \quad (2.2.2).$$

Variable separation can be performed:

$$\tilde{E}(\vec{r}, \omega - \omega_0) = F(x, y, \omega - \omega_0) \tilde{A}(z, \omega - \omega_0) \exp(i\beta_0 z) \quad (2.2.3),$$

where $F(x, y, \omega - \omega_0)$ is the transverse mode distribution, $\tilde{A}(z, \omega - \omega_0)$ is the axial propagation envelope, and β_0 is the wave number at ω_0 .

The time domain representation of $\tilde{A}(z, \omega - \omega_0)$ is

$$A(z, t) = FT^{-1} \{ \tilde{A}(z, \omega - \omega_0) \} = \frac{1}{2\pi} \int_{-\infty}^{\infty} \tilde{A}(z, \omega - \omega_0) \exp[-i(\omega - \omega_0)t] d\omega \quad (2.2.4).$$

Through the process in Table 2.2, the GNLSE in the time domain is obtained:

$$\frac{\partial A}{\partial z} + \frac{\alpha}{2} A - \sum_{k \geq 2} \frac{i^{k+1}}{k!} \beta_k \frac{\partial^k A}{\partial T^k} = i\gamma \left(1 + i\tau_{shock} \frac{\partial}{\partial T} \right) \left(A(z, T) \int_{-\infty}^{\infty} R(T') |A(z, T - T')|^2 dT' \right) \quad (2.2.30).$$

Electromagnetic field:		the Maxwell's equations	
For light:			
$\nabla \times \nabla \times \vec{E} = -\frac{1}{c^2} \frac{\partial^2 \vec{E}}{\partial t^2} - \mu_0 \frac{\partial^2 \vec{P}}{\partial t^2}$ (2.2.5), in which $c^2 = \frac{1}{\mu_0 \epsilon_0}$ (2.2.6)			
Linear polarization: under scalar assumption	Nonlinear polarization: $\vec{P} = \epsilon_0 (\chi^{(1)} \cdot \vec{E} + \chi^{(2)} : \vec{E}\vec{E} + \chi^{(3)} : \vec{E}\vec{E}\vec{E} + \dots)$ (2.2.12)		
$P(t) = \epsilon_0 \chi^{(1)} E(t)$ (2.2.7)	Under scalar assumption, only Kerr effect: $P(t) = \epsilon_0 \chi^{(1)} E(t) + \epsilon_0 \frac{3}{4} \chi_{xxxx}^{(3)} E(t) \cdot E(t) ^2$ (2.2.13)	further add delayed response (Raman): $P(t) = \epsilon_0 \chi^{(1)} E(t) + \epsilon_0 \frac{3}{4} \chi_{xxxx}^{(3)} E(t) \cdot \int_{-\infty}^t R(t-t_1) E(t_1) ^2 dt_1$ (2.2.26)	
Propagation equation: $\nabla^2 \tilde{E} + \frac{\epsilon(\omega)\omega^2}{c^2} \tilde{E}(\omega) = 0$ (2.2.8) $\epsilon(\omega) = 1 + \tilde{\chi}^{(1)}(\omega) = (n + i2\alpha/k)^2$ (2.2.9A) $\epsilon(\omega) = n^2(\omega)$ for lossless (2.2.9B)	Propagate equation: Same as (2.2.8) $\epsilon(\omega) = 1 + \tilde{\chi}^{(1)}(\omega) + \frac{3}{4} \chi_{xxxx}^{(3)} E ^2$ (2.2.14) $\epsilon_{NL} = \frac{3}{4} \chi_{xxxx}^{(3)} E ^2$ treated as a constant	Propagate equation: Same as (2.2.8) $\epsilon(\omega) = 1 + \tilde{\chi}^{(1)}(\omega) + \frac{3}{4} \chi_{xxxx}^{(3)} \int_{-\infty}^t R(t-t_1) E(t_1) ^2 dt_1$ (2.2.27)	
How to solve: Variable separation: $\tilde{E}(r, \omega - \omega_0) = F(x, y) \tilde{A}(z, \omega - \omega_0) e^{i\beta_0 z}$ Transverse: solve modes & get axial wave number $\frac{\partial^2 F}{\partial x^2} + \frac{\partial^2 F}{\partial y^2} + [\epsilon(\omega)k_0^2 - \tilde{\beta}^2] F = 0$ (2.2.10) $\epsilon(\omega) = n^2(\omega)$ for lossless $\tilde{\beta} = \beta$ for fundamental mode	How to solve: Use the linear lossless solution (left column), and add Kerr effect and loss as perturbations. Consider fundamental mode. The mode does not change with the perturbations. $\epsilon = (n + \Delta n)^2 \approx n^2 + 2n\Delta n$ (2.2.15) $\Delta n = n_2 E ^2 + \frac{i\tilde{\alpha}}{2k_0}$ (2.2.16) $\tilde{\beta}(\omega) = \beta(\omega) + \Delta\beta(\omega)$ (2.2.17) $\Delta\beta(\omega) = \frac{\omega^2 n(\omega)}{c^2 \beta(\omega)} \frac{\int \int_{-\infty}^{\infty} \Delta n(\omega) F(x, y) ^2 dx dy}{\int \int_{-\infty}^{\infty} F(x, y) ^2 dx dy}$ $= \frac{i}{2} \alpha + \gamma A ^2$ (loss + Kerr) (2.2.18) $\frac{\partial \tilde{A}}{\partial z} = i[\beta(\omega) + \Delta\beta(\omega) - \beta_0] \tilde{A}$ (2.2.19) meaning: phase shift depending on dispersion and nonlinearity. $\tilde{A}(z) = \tilde{A}(0) \exp\{i[\beta(\omega) + \Delta\beta(\omega) - \beta_0]z\}$ (2.2.20)	How to solve: Use the results in the middle column and add replace $ E ^2$ with $\int_{-\infty}^t R(t-t_1) E(t_1) ^2 dt_1$. $\Delta\beta(\omega) = \frac{i}{2} \alpha + \gamma(\omega) FT \left\{ \int_{-\infty}^t R(t-t_1) A(t_1) ^2 dt_1 \right\}$ (2.2.28)	
Axial: $2i\beta_0 \frac{\partial \tilde{A}}{\partial z} + (\tilde{\beta}^2 - \beta_0^2) \tilde{A} = 0$ (2.2.11)	Go back to time domain: Do inverse FT on propagation equation; Taylor expansion on $\beta(\omega), \Delta\beta(\omega), \alpha, \gamma$. $\beta(\omega) = \beta_0 + (\omega - \omega_0)\beta_1 + \frac{1}{2!}(\omega - \omega_0)^2 \beta_2 + \frac{1}{3!}(\omega - \omega_0)^3 \beta_3 + \dots$ (2.2.21)	Go back to time domain: Same as left + Add more terms of the Taylor series	

<p>iFT is equivalent to replacing $(\omega - \omega_0)$ with $i \frac{\partial}{\partial t}$</p> <p>iFT: $\Rightarrow \beta_0 + i \frac{\partial}{\partial t} \beta_1 - \frac{1}{2!} \frac{\partial^2}{\partial t^2} \beta_2 - \frac{1}{3!} i \frac{\partial^3}{\partial t^3} \beta_3 + \dots$</p> <p style="text-align: right;">(2.2.22)</p> <p>same for $\Delta\beta(\omega)$, α and γ.</p> $\frac{\partial A}{\partial z} = i \left(i \frac{\partial}{\partial t} \beta_1 - \frac{1}{2} \frac{\partial^2}{\partial t^2} \beta_2 \right) A + i \Delta\beta_0 A$ <p style="text-align: right;">(2.2.23).</p> <p>Change of variable</p> $T = t - \beta_1 z$ <p style="text-align: right;">(2.2.24),</p> <p>and then $\beta_1 \rightarrow 0$, yielding</p> $\frac{\partial A}{\partial z} = \left(-\frac{i}{2} \frac{\partial^2}{\partial t^2} \beta_2 \right) A - \frac{\alpha}{2} A + i\gamma A ^2 A$ <p style="text-align: center;">(for ps pulse)</p> <p style="text-align: right;">(2.2.25)</p>	$\frac{\partial A}{\partial z} = -\frac{1}{2} \left(\alpha_0 + i\alpha_1 \frac{\partial}{\partial t} \right) A$ $+ i \left(i\beta_1 \frac{\partial}{\partial t} - \frac{1}{2!} \beta_2 \frac{\partial^2}{\partial t^2} - \frac{i}{3!} \beta_3 \frac{\partial^3}{\partial t^3} + \dots \right) A$ $+ i \left(\gamma_0 + i\gamma_1 \frac{\partial}{\partial t} \right) \left(A \int_{-\infty}^t R(t-t_1) A(t_1) ^2 dt_1 \right)$ <p style="text-align: right;">(2.2.29)</p> <p>change of variable $T = t - \beta_1 z$, then $\beta_1 \rightarrow 0$ define $\gamma_1 \sim \gamma/\omega_0 = \gamma\tau_{shock}$, and neglect α:</p> $\frac{\partial A}{\partial z} + \frac{\alpha}{2} A - \sum_{k \geq 2} \frac{i^{k+1}}{k!} \beta_k \frac{\partial^k A}{\partial T^k}$ $= i\gamma \left(1 + i\tau_{shock} \frac{\partial}{\partial T} \right)$ $\times \left(A(z, T) \int_{-\infty}^{\infty} R(T') A(z, T - T') ^2 dT' \right)$ <p style="text-align: right;">(2.2.30).</p> <p>(for fs pulse. Good for pulses as short as a few optical cycles if enough higher-order β_k included)</p>
---	--

Table 2.2 Brief derivation of the GNLSE.

The definition of the variables and the parameters is in Table 2.3.

The frequency domain GNLSE is

$$\frac{\partial \tilde{A}'}{\partial z} = i\bar{\gamma}(\omega) \exp(-\hat{L}(\omega)z) FT \left\{ \bar{A}(z, T) \int_{-\infty}^{\infty} R(T') |\bar{A}(z, T - T')|^2 dT' \right\} \quad (2.2.31).$$

See Table 2.3 for definition of the variables and the parameters. Eq. 2.2.31 is equivalent to Eq. 2.2.30 through Fourier transform and changing of variables.

Variables and parameters in GNLSE	Definition
$A(z, T)$	Axial envelope of the electric field, in time domain.
$\bar{A}(z, T)$	$\bar{A}(z, T) = FT^{-1} \left\{ \frac{\tilde{A}(z, \omega)}{A_{eff}^{1/4}(\omega)} \right\}$.
$\tilde{A}(z, \omega)$	Frequency-domain representation of $A(z, T)$. $\tilde{A}(z, \omega) = FT \{ A(z, T) \}$.
$\tilde{A}'(z, \omega)$	$\tilde{A}(z, \omega)$ with the linear operator absorbed: $\tilde{A}'(z, \omega) = \tilde{A}(z, \omega) \exp(-\hat{L}(\omega)z)$
$A_{eff}(\omega)$	Effective mode area. $A_{eff}(\omega) = \frac{\left(\int_{-\infty}^{\infty} F(x, y, \omega) ^2 dx dy \right)^2}{\int_{-\infty}^{\infty} F(x, y, \omega) ^4 dx dy}$.
$\hat{L}(\omega)$	Linear operator, including dispersion and loss. $\hat{L}(\omega) = i[\beta(\omega) - \beta(\omega_0) - \beta_1(\omega_0)(\omega - \omega_0)] - \alpha(\omega)/2$.
n_0	Linear refractive index.
$n_2(\omega)$	Nonlinear refractive index. $n = n_0 + n_2 E ^2$. $n_2 = \frac{3}{8n} \text{Re} \{ \chi_{xxxx}^{(3)} \}$.
$n_{eff}(\omega)$	Mode effective refractive index. In the simulations $\sim n_0$.
$R(t)$	Nonlinear response function: $P_{NL}(\vec{r}, t) \propto E(\vec{r}, t) \int_{-\infty}^{\infty} R(t') E(\vec{r}, t - t') ^2 dt'$.
α	Loss: $A(z) = A(0) \exp(\alpha z/2)$.
β_k	Taylor expansion coefficient of wave number $\beta(\omega)$, representing dispersion $\beta(\omega) = \beta_0 + (\omega - \omega_0)\beta_1 + \frac{1}{2!}(\omega - \omega_0)^2 \beta_2 + \frac{1}{3!}(\omega - \omega_0)^3 \beta_3 + \dots$ Inverse FT to time domain $\Rightarrow \beta_0 + i \frac{\partial}{\partial t} \beta_1 - \frac{1}{2!} \frac{\partial^2}{\partial t^2} \beta_2 - \frac{1}{3!} i \frac{\partial^3}{\partial t^3} \beta_3 + \dots$
τ_{shock}	$\tau_{shock} = 1/\omega_0$.
γ	Nonlinearity coefficient. $\gamma = \frac{\omega_0 n_2(\omega_0)}{c A_{eff}(\omega_0)}$.
$\bar{\gamma}(\omega)$	Frequency dependent nonlinearity coefficient: $\bar{\gamma}(\omega) = \frac{n_2 n_0 \omega}{c n_{eff}(\omega) A_{eff}^{1/4}(\omega)}$.

Table 2.3. Definition of the variables and the parameters in the GNLSE.

The physical meaning of the GNLSE is as follows. In the time domain equation (Eq. 2.2.30), the term $+\frac{\alpha}{2}A$ shows the loss, and the term $-\sum_{k \geq 2} \frac{i^{k+1}}{k!} \beta_k \frac{\partial^k A}{\partial T^k}$ shows the dispersion expanded in Taylor series. At the right hand side, $i\gamma \cdot 1$ and $i\gamma \cdot i\tau_{shock} \frac{d}{dT}$ are the first and second terms of the Taylor expansion of $\gamma(\omega)$ (see Eq. 2.2.29 in Table 2.2). The term $\left(A(z, T) \int_{-\infty}^{\infty} R(T') |A(z, T - T')|^2 dT' \right)$ describes the nonlinear response, which is conceptually proportional to the cube of A .

In the frequency domain GNLSE (Eq. 2.2.31), the dispersion and the loss are included in $\hat{L}(\omega)$, and the nonlinearity coefficient is $\bar{\gamma}(\omega)$. These parameters are straightforwardly functions of the frequency. The nonlinear response term is still integrated in the time domain, and then transformed to the frequency domain.

More physical interpretation is in Section 2.3. In the following (Section 2.2.2 and 3), specific calculation of some terms is introduced in a mathematical perspective.

2.2.2 The dispersion term

Consider wave number $\beta(\omega)$

$$\beta(\omega) \equiv \frac{2\pi}{\lambda(\omega)} = \frac{\omega}{v_p(\omega)} = \frac{n(\omega)\omega}{c} \quad (2.2.32),$$

in which v_p is the phase velocity. The unit of $\beta(\omega)$ is 1/m.

The Taylor expansion of $\beta(\omega)$ is

$$\begin{aligned} \beta(\omega) = & \beta(\omega_0) + (\omega - \omega_0)\beta_1(\omega_0) + \frac{1}{2!}(\omega - \omega_0)^2\beta_2(\omega_0) + \frac{1}{3!}(\omega - \omega_0)^3\beta_3(\omega_0) \\ & + \frac{1}{4!}(\omega - \omega_0)^4\beta_4(\omega_0) + \dots \end{aligned} \quad (2.2.33).$$

The coefficients $\beta_k(\omega_0)$ are k^{th} -order dispersions

$$\beta_k(\omega_0) = \left. \frac{d^k \beta}{d\omega^k} \right|_{\omega_0}, \quad k = 0, 1, 2, \dots \quad (2.2.34).$$

β_1 is connected to the group velocity v_g :

$$\beta_1(\omega) = \frac{1}{v_g(\omega)} \quad (2.2.35).$$

β_2 is the group velocity dispersion (GVD):

$$\beta_2(\omega) = \frac{d^2 \beta(\omega)}{d\omega^2} = \frac{d}{d\omega} \left(\frac{1}{v_g(\omega)} \right) \quad (2.2.36).$$

There is an alternative GVD parameter

$$D(\omega) = -\frac{2\pi c}{\lambda^2} \beta_2(\omega) = \frac{1}{L} \frac{d}{d\lambda} \left(\frac{L}{v_g(\omega)} \right) \quad (2.2.37).$$

$\beta_k(\omega_0)|_{k \geq 3}$ are usually referred to as higher-order dispersions in the SC context.

The dispersion coefficient in the GNLSE is $\sum_{k \geq 2} \frac{i^{k+1}}{k!} \beta_k(\omega_0) \frac{\partial^k}{\partial T^k}$ in the time domain (Eq.

2.2.30) or equivalently $\sum_{k \geq 2} \frac{i^{k+1}}{k!} \beta_k(\omega_0) (\omega - \omega_0)^k = \beta(\omega) - \beta(\omega_0) - \beta_1(\omega_0)(\omega - \omega_0)$ in the

frequency domain (see Eq. 2.2.31 and the definition of $\hat{L}(\omega)$ in table 2.3). Here this term is notated as $B(\omega)$:

$$B(\omega) = \beta(\omega) - \beta_0(\omega_0) - (\omega - \omega_0)\beta_1(\omega_0)$$

$$= \frac{1}{2!}(\omega - \omega_0)^2 \beta_2(\omega_0) + \frac{1}{3!}(\omega - \omega_0)^3 \beta_3(\omega_0) + \frac{1}{4!}(\omega - \omega_0)^4 \beta_4(\omega_0) + \dots \quad (2.2.38).$$

$\beta_2(\omega_0)$ is the lowest order dispersion considered here. $\beta_1(\omega_0)$ has been eliminated when using the time frame that travels at the group velocity (Eq. 2.2.24).

There are two ways to calculate $B(\omega)$ based on $\beta_2(\omega)$.

(1) Considering

$$\beta_2(\omega) = \frac{d^2 \beta(\omega)}{d\omega^2} \quad (2.2.36)$$

$$= \beta_2(\omega_0) + (\omega - \omega_0)\beta_3(\omega_0) + \frac{1}{2!}(\omega - \omega_0)^2 \beta_4(\omega_0) + \dots \quad (2.2.39),$$

$\beta_k(\omega_0)|_{k \geq 3}$ can be obtained based on $\beta_2(\omega)$, and then $B(\omega)$ can be calculated using Eq. 2.2.38.

(2) Considering

$$\beta_2(\omega) = \frac{d^2 \beta(\omega)}{d\omega^2} \quad (2.2.36)$$

$$= \frac{d^2 B(\omega)}{d\omega^2} \quad (2.2.40),$$

there is:

$$B(\omega) = \iint \beta_2(\omega) d\omega^2 \quad (2.2.41).$$

This indefinite integral needs to be zeroed. Considering Eq. 2.2.38, there are:

$$B'(\omega)|_{\omega_0} = \int \beta_2(\omega) d\omega|_{\omega_0} = 0 \quad (2.2.42A)$$

$$\Rightarrow B'(\omega) = \int \beta_2(\omega) d\omega - \left[\int \beta_2(\omega) d\omega \right]_{\omega_0} \quad (2.2.42B),$$

and

$$B(\omega_0) = 0 \quad (2.2.43A)$$

$$\Rightarrow B(\omega) = \int B'(\omega) d\omega - \left[\int B'(\omega) d\omega \right]_{\omega_0} \quad (2.2.43B).$$

2.2.3 The Raman term

When only the Kerr effect (see Section 2.3.1) is concerned, the polarization is

$$P(t) = \varepsilon_0 \chi^{(1)} E(t) + \varepsilon_0 \frac{3}{4} \chi_{xxxx}^{(3)} E(t) \cdot |E(t)|^2 \quad (2.2.13).$$

When the Kerr effect and the Raman effect (see Section 2.3.4) are considered, the polarization becomes

$$P(t) = \varepsilon_0 \chi^{(1)} E(t) + \varepsilon_0 \frac{3}{4} \chi_{xxxx}^{(3)} E(t) \cdot \int_{-\infty}^t R(t-t_1) |E(t_1)|^2 dt_1 \quad (2.2.26)$$

$$= \varepsilon_0 \chi^{(1)} E(t) + \varepsilon_0 \frac{3}{4} (1-f_R) \chi_{xxxx}^{(3)} E(t) \cdot |E(t)|^2 + \varepsilon_0 \frac{3}{4} f_R \chi_{xxxx}^{(3)} E(t) \cdot \int_{-\infty}^t h_R(t-t_1) |E(t_1)|^2 dt_1 \quad (2.2.44),$$

in which the response function

$$R(t) = (1-f_R) \delta(t) + f_R h_R(t) \quad (2.2.45).$$

It is normalized as follows:

$$\int_{-\infty}^{\infty} h_R(t) dt = 1 \quad (2.2.46A),$$

$$\int_{-\infty}^{\infty} \delta(t) dt = 1 \quad (2.2.46B),$$

and

$$\int_{-\infty}^{\infty} R(t) dt = 1 \quad (2.2.46C).$$

In Eq. 2.2.44 (compare with Eq. 2.2.13), the first term is the linear response, the 2nd term is the Kerr effect, which is electronic response considered instantaneous, and the 3rd term is the Raman effect, which is a delayed response.

Consider Eq. 2.2.44 in the frequency domain and we can see more physical meaning:

$$\tilde{P}(\omega) = \varepsilon_0 \chi^{(1)} \tilde{E}(\omega) + \varepsilon_0 \frac{3}{4} (1 - f_R) \chi_{xxxx}^{(3)} |\tilde{E}(\omega)|^2 \tilde{E}(\omega) + \varepsilon_0 \frac{3}{4} f_R \chi_{xxxx}^{(3)} \tilde{h}_R(\omega) |\tilde{E}(\omega)|^2 \tilde{E}(\omega) \quad (2.2.47),$$

in which $\tilde{h}_R(\omega) = FT\{h_R(t)\}$, and the convolution $\int_{-\infty}^t h_R(t-t_1) |E(t_1)|^2 dt_1$ in Eq. 2.2.44 has been transformed to $\tilde{h}_R(\omega) |\tilde{E}(\omega)|^2$ here. The 3rd term is the Raman term, which shows a complex susceptibility:

$$\frac{3}{4} f_R \chi_{xxxx}^{(3)} \tilde{h}_R(\omega) |\tilde{E}(\omega)|^2 = \frac{3}{4} |\tilde{E}(\omega)|^2 \left(f_R \chi_{xxxx}^{(3)} \operatorname{Re}\{\tilde{h}_R(\omega)\} + f_R \chi_{xxxx}^{(3)} \operatorname{Im}\{\tilde{h}_R(\omega)\} \right) \quad (2.2.48).$$

The real part is associated with the real refractive index, which will cause a phase delay in the solution field. The imaginary part is associated with the imaginary refractive index, which causes gain or loss. The Raman gain spectrum is

$$\begin{aligned} g_R(\omega) &= \frac{2\omega_0 n_2}{c} f_R \operatorname{Im}\{\tilde{h}_R(\omega)\} \\ &= \frac{4\pi n_2}{\lambda_0} f_R \operatorname{Im}\{\tilde{h}_R(\omega)\} \\ &= c1 \cdot f_R \operatorname{Im}\{\tilde{h}_R(\omega)\} \end{aligned} \quad (2.2.49).$$

In the last step $c1 = \frac{4\pi n_2}{\lambda_0}$ is used for clarity.

To obtain $h_R(t)$ or $\tilde{h}_R(\omega)$, usually $\operatorname{Re}\{\tilde{h}_R(\omega)\}$ and $\operatorname{Im}\{\tilde{h}_R(\omega)\}$ are needed. The Raman gain spectrum $g_R(\omega)$ can be measured experimentally, so that $\operatorname{Im}\{\tilde{h}_R(\omega)\}$ can be calculated. But $\operatorname{Re}\{\tilde{h}_R(\omega)\}$ is hard to obtain, because it requires measuring the wavelength-

dependent refractive index. There are two methods to calculate $\tilde{h}_R(\omega)$ based on $g_R(\omega)$ alone, without knowing $\text{Re}\{\tilde{h}_R(\omega)\}$.

(1) The Kramers-Kronig relation connects the real and the imaginary parts of susceptibility:

$$\text{Re}\{\chi(\omega)\} = \frac{2}{\pi} \int_0^\infty \frac{\omega' \text{Im}\{\chi(\omega')\}}{\omega'^2 - \omega^2} d\omega' \quad (2.2.50).$$

$f_R \chi_{xxxx}^{(3)} \tilde{h}_R(\omega)$ is proportional to the Raman-induced susceptibility:

$$\text{Re}\{\chi_{xxxx}^{(3) \text{ Raman}}(\omega)\} \propto f_R \chi_{xxxx}^{(3)} \text{Re}\{\tilde{h}_R(\omega)\} \quad (2.2.51A),$$

$$\text{Im}\{\chi_{xxxx}^{(3) \text{ Raman}}(\omega)\} \propto f_R \chi_{xxxx}^{(3)} \text{Im}\{\tilde{h}_R(\omega)\} \quad (2.2.51B).$$

So $\text{Re}\{\tilde{h}_R(\omega)\}$ and $\text{Im}\{\tilde{h}_R(\omega)\}$ are connected through the Kramers-Kronig relation too.

After calculating $\text{Im}\{\tilde{h}_R(\omega)\}$ based on $g_R(\omega)$, $\text{Re}\{\tilde{h}_R(\omega)\}$ can be calculated based on $\text{Im}\{\tilde{h}_R(\omega)\}$. And then $\tilde{h}_R(\omega)$ is obtained.

(2) Since $g_R(\omega)$ is connected with only the imaginary part of $\tilde{h}_R(\omega)$, the sine/cosine transforms can be used to replace the Fourier/inverse Fourier transforms. The sine/cosine transforms are defined as:

$$G_{\sin}(\omega) = ST\{g(t)\} = 2 \int_0^\infty g(t) \sin(\omega t) dt \quad (2.2.52A),$$

$$G_{\cos}(\omega) = CT\{g(t)\} = 2 \int_0^\infty g(t) \cos(\omega t) dt \quad (2.2.52B).$$

The inverse sine/cosine transforms have the same forms:

$$g(t) = ST \{G_{Sin}(\omega)\} = 2 \int_0^{\infty} G_{Sin}(\omega) \sin(\omega t) d\omega \quad (2.2.53A),$$

$$g(t) = CT \{G_{Cos}(\omega)\} = 2 \int_0^{\infty} G_{Cos}(\omega) \cos(\omega t) d\omega \quad (2.2.53B).$$

Note sine/cosine transforms are defined on $t \geq 0$ and $\omega \geq 0$.

Considering $h_R(t < 0) = 0$, the Fourier transform can be replaced by the sine/cosine transforms:

$$\tilde{h}_R(\omega) = FT \{h_R(t)\} = \frac{1}{2} CT \{h_R(t)\} + i \cdot \frac{1}{2} ST \{h_R(t)\} \quad (t \geq 0) \quad (2.2.54).$$

And because $h_R(t)$ is real, the imaginary part of the last equation is:

$$\text{Im}\{\tilde{h}_R(\omega)\} = \frac{1}{2} ST \{h_R(t)\} \quad (\omega \geq 0) \quad (2.2.55).$$

Thus Eq. 2.2.49 becomes

$$g_R(\omega) = c1 \cdot f_R \cdot \frac{1}{2} ST \{h_R(t)\} \quad (2.2.56).$$

Using the inverse sine transform:

$$\begin{aligned} h_R(t) &= \frac{2}{c1 \cdot f_R} ST \{g_R(\omega)\} \\ &= \frac{4}{c1 \cdot f_R} \text{Im}\{FT \{g_R(\omega)\}\} \quad (t \geq 0, \omega \geq 0) \end{aligned} \quad (2.2.57),$$

thus $h_R(t)$ is directly calculated based on $g_R(\omega)$.

$h_R(t)$ should be normalized by definition (Eq. 2.2.46A). Given absolute-valued (not relative-magnitude) $g_R(\omega)$, f_R is adjusted to guarantee that Eq. 2.2.57 holds.

A popular simplification of the Raman gain spectrum $g_R(\omega)$ is modeling it as a Lorentzian curve:

$$g_R(\omega) = g_0 \frac{(\Delta\omega/2)^2}{(\omega - \omega_0)^2 + (\Delta\omega/2)^2} \quad (2.2.58),$$

where ω_0 is the frequency of the peak, $\Delta\omega$ is the FWHM, and g_0 is the peak magnitude.

Under this approximation, the Raman response function $h_R(t)$ is a damping oscillation (normalized):

$$h_R(t) = \frac{\tau_1^2 + \tau_2^2}{\tau_1 \tau_2^2} \exp\left(-\frac{t}{\tau_2}\right) \sin\left(\frac{t}{\tau_1}\right) \Theta(t) \quad (2.2.59),$$

where $\Theta(t)$ is the Heaviside step function. Comparing Eq. 2.2.59 with the Fourier transform of Eq. 2.2.58, we see the oscillation period τ_1 is associated with the frequency of the peak in the gain spectrum

$$\tau_1 = \frac{1}{\omega_0} = \frac{1}{2\pi f_0} = \frac{1}{2\pi c \cdot \beta_0} \quad (2.2.60A),$$

and the damping rate τ_2 is associated with the width of the gain spectrum

$$\tau_2 = \frac{1}{\Delta\omega/2} = \frac{1}{\pi \cdot \Delta f} = \frac{1}{\pi c \cdot \Delta\beta} \quad (2.2.60B).$$

ω_0 , f_0 , and β_0 are the angular frequency, frequency, and wave number of the peak, respectively; and $\Delta\omega$, Δf , and $\Delta\beta$ are the FWHM of the gain spectrum in angular frequency, frequency, and wave number, respectively.

The Heaviside step function $\Theta(t)$ guarantees the causality relation that the induced nonlinearity at time T is caused by the field at time $-\infty < t < T$:

$$\begin{aligned} & \bar{A}(z, T) \int_{-\infty}^{\infty} \Theta(T') |\bar{A}(z, T - T')|^2 dT' \\ &= \bar{A}(z, T) \int_{-\infty}^0 |\bar{A}(z, T - T')|^2 dT' \\ &= \bar{A}(z, T) \int_{-\infty}^T |\bar{A}(z, t)|^2 dt \quad (\text{used } t = T - T') \end{aligned} \quad (2.2.61).$$

The model of Eq. 2.2.58 and 59 is not very accurate, especially when $g_R(\omega)$ has multiple dominant peaks. Modeling $g_R(\omega)$ as a sum of multiple Lorentzian functions has been reported [Hollenbeck and Cantrell, 2002; Qin et al, 2007]. One can simply use the approximation-free form of $h_R(t)$ calculated from the numerical curve of $g_R(\omega)$ when possible.

2.2.4 Implementation of numerical simulation

Two popular methods to numerically solve the GNLSE are: (1) split-step Fourier method based on Eq. 2.2.30, and (2) direct integration based on Eq. 2.2.31 since it is an ordinary differential equation (ODE).

The second method is used in my simulations. Ignoring the frequency dependence of $n_2(\omega)$, $n_{eff}(\omega)$, and $A_{eff}(\omega)$, Eq. 2.2.31 is simplified to

$$\frac{\partial \tilde{A}'}{\partial z} = i\gamma \frac{\omega}{\omega_0} \exp(-\hat{L}(\omega)z) F.T. \left\{ A(z, T) \int_{-\infty}^{\infty} R(T') |A(z, T - T')|^2 dT' \right\} \quad (2.2.62).$$

Here $A(z, T)$ has been used to replace $\bar{A}(z, T)$ in Eq. 2.2.31. $A_{eff}^{-3/4}(\omega)$ has been factored out. And $\bar{\gamma}(\omega) A_{eff}^{-3/4}(\omega)$ is simplified to $\gamma \frac{\omega}{\omega_0}$ under the approximation that $n_2(\omega) \sim n_2(\omega_0)$, $n_{eff}(\omega) \sim n_0$, and $A_{eff}(\omega) \sim A_{eff}(\omega_0)$.

The pump is firstly modeled in the time domain as a Gaussian or sech² pulse, and then transformed into the frequency domain.

In the implementation of the numerical simulations, there are two requirements on the numerical grids. (1) The temporal grid must cover the whole time duration that the pulse will spread to. (2) The frequency grid must cover 2× the highest frequency of the radiation.

The ‘‘ODE45’’ solver in MATLAB is used here to solve Eq. 2.2.62. The solver automatically finds optimal step lengths to satisfy user-specified precisions. The code

provided in [Dudley and Taylor, 2010] is used here, with some adjustment (see Appendix C).

2.3 Major Physical Processes in Supercontinuum Generation

2.3.1 Kerr effect and self phase modulation

The Kerr effect is the change of refractive index depending on the applied electric field:

$$n = n_0 + n_2 |\vec{E}|^2 = n_0 + n_2 I \quad (2.3.1),$$

where the nonlinear refractive index n_2 is related to the 3rd order susceptibility

$$n_2 = \frac{3}{8n_0} \text{Re}(\chi_{xxxx}^{(3)}) \quad (2.3.2),$$

which can be derived from Eq. 2.2.9A and 2.2.13 under some approximation.

The Kerr effect can cause self phase modulation (SPM), cross phase modulation (XPM), and some other phenomena. In SPM, the intensity-dependent refractive index and the temporal shape of the pulse cause phase shift, leading to frequency shift. New frequencies are generated continuously, and the spectrum is broadened.

SPM can be calculated analytically as follows. Consider the phase propagation

$$\phi = \omega_0 t - kx + \phi_0 = \omega_0 t - \frac{2\pi}{\lambda_0} nL + \phi_0 \quad (2.3.3),$$

in which ω_0 is the carrier frequency, k is the wave number, ϕ_0 is the initial phase, λ_0 is the carrier wavelength, and L is the propagation length.

The frequency is related to the phase by

$$\omega = \frac{d\phi}{dt} \quad (2.3.4).$$

Plugging Eq. 2.3.3 in Eq. 2.3.4 yields

$$\omega = \omega_0 - \frac{2\pi L}{\lambda_0} \frac{dn}{dt}$$

plugging in Eq. 2.3.1:

$$= \omega_0 - \frac{2\pi n_2 L}{\lambda_0} \frac{dI(t)}{dt} \quad (2.3.5),$$

which means the frequency shift depends on n_2 and the slope dI/dt . For optical pulses, there is $dI/dt > 0$ at the leading edge, yielding a red shift in frequency; at the trailing edge, there is $dI/dt < 0$, yielding a blue shift.

2.3.2 Dispersion

Optical dispersion refers to the phenomenon that the velocity of light depends on its frequency. Usually, the dispersion refers to the frequency dependence of the phase velocity v_p ; and the group velocity dispersion (GVD) refers to the frequency dependence of the group velocity v_g .

Dispersion is a linear effect, in which no new frequencies are generated, and no original frequencies are annihilated. It is a temporal redistribution of radiation of different frequencies, causing temporal broadening or compression and chirps.

According to Eq. 2.2.30, $\beta_2(\omega)$ is the lowest-order of dispersion considered in the SC generation context, also the dominant dispersion term in most cases. Along propagation, normal GVD ($\beta_2 > 0$, $D < 0$) causes up-chirp, because red light travels faster, and the leading edge becomes redder and the trailing edge bluer. In the opposite case, anomalous GVD ($\beta_2 < 0$, $D > 0$) causes down-chirp. The wavelength of zero GVD is called the zero dispersion wavelength (ZDW).

Recall SPM causes up-chirp, namely red shift at the leading edge and blue shift at the trailing edge. When normal GVD is added to SPM, the red-shifted radiation at the leading edge travels faster than the main pulse (frequency not shifted), and the blue-shifted radiation at the trailing edge travels slower than the main pulse. This causes the pulse to become longer in time, and lowers the peak power, and thus limits further spectral broadening.

When anomalous GVD is added to SPM, frequency-shifted radiation at the leading and the trailing edges tends to squeeze into the main pulse in time, making the pulse peak power higher. Generally speaking, the pulse tends to swing back and forth between spectrally-broader-temporally-shorter and spectrally-narrower-temporally-longer. This is the case of higher-order solitons introduced in the next section. Under certain circumstances, anomalous GVD and SPM perfectly balance each other, and the pulse

keep invariant in spectrum and in time. This is the case of a fundamental soliton as in the next section.

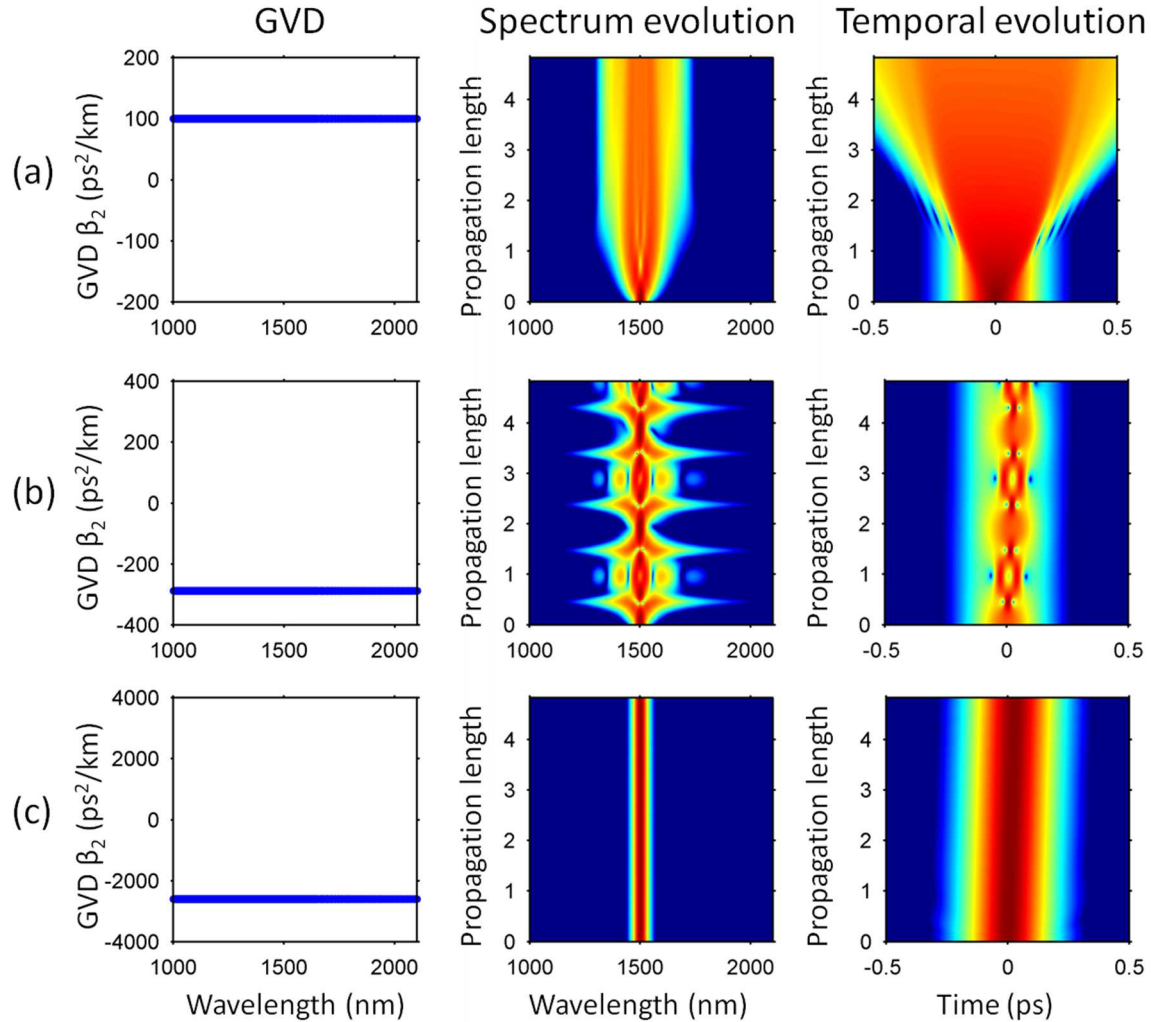


Fig. 2.1 Spectral and temporal evolution when different GVD is added to SPM. (a) SPM + normal GVD. The normal GVD limits the spectral broadening. (b) SPM + anomalous GVD. The pulse swings back and forth between spectrally-broader-temporally-shorter and spectrally-narrower-temporally-longer. This is a higher-order soliton propagating periodically (see Section 2.3.3). (c) SPM + a particular value of anomalous GVD such that they perfectly balance each other. In this case the pulse keeps invariant in spectrum and in temporal profile. This is a fundamental soliton (see Section 2.3.3).

2.3.3 Soliton and soliton fission

An optical soliton is an optical pulse that is temporally unbroadened and undistorted during propagation [Hasegawa and Tappert, 1973; Mollenauer et al., 1980]. Consider the GNLSE including the Kerr effect and GVD:

$$i \frac{dA}{dz} = \frac{\beta_2}{2} \frac{\partial^2 A}{\partial T^2} - \gamma |A|^2 A \quad (2.3.6).$$

The variables can be normalized as follows:

$$U = A/\sqrt{P_0}, \quad \xi = z/L_D, \quad \text{and} \quad \tau = T/T_0 \quad (2.3.7),$$

yielding

$$i \frac{dU}{d\xi} = \frac{\text{sgn}(\beta_2)}{2} \frac{\partial^2 U}{\partial \tau^2} - N^2 |U|^2 U \quad (2.3.8),$$

in which N is defined as

$$N^2 = \frac{L_D}{L_{NL}} = \frac{\gamma P_0 T_0^2}{|\beta_2|} \quad (2.3.9).$$

N is called soliton number, the meaning of which will be shown in the following. L_D and L_{NL} are the characteristic dispersion length and nonlinear length, respectively, which quantify the length scale over which the dispersion or the nonlinear effect becomes significant:

$$L_D = T_0^2 / |\beta_2| \quad (2.3.10A),$$

$$L_{NL} = 1/\gamma P_0 \quad (2.3.10B).$$

In the anomalous GVD regime where $\text{sgn}(\beta_2) = -1$, Eq. 2.3.8 becomes

$$i \frac{dU}{d\xi} = -\frac{1}{2} \frac{\partial^2 U}{\partial \tau^2} - N^2 |U|^2 U \quad (2.3.11).$$

This can be further simplified to the standard form of NLS equation:

$$i \frac{du}{d\xi} + \frac{1}{2} \frac{\partial^2 u}{\partial \tau^2} + |u|^2 u = 0 \quad (2.3.12)$$

by defining

$$u = NU = \sqrt{\gamma T_0^2 / |\beta_2|} A \quad (2.3.13).$$

For $N = 1$, the solution of Eq. 2.3.12 is

$$u(\xi, \tau) = \eta \text{sech}(\eta \tau) \exp(i\eta^2 \xi / 2) \quad (2.3.14).$$

Choosing $u(0,0) = 1$, it becomes the canonical form:

$$u(\xi, \tau) = \text{sech}(\tau) \exp(i\xi/2) \quad (2.3.15).$$

This is the fundamental ($N = 1$) soliton. Its spectrum and temporal profile do not change in propagation (see Fig. 2.1 (c)).

For $N \geq 2$, there is a subset of solutions with initial fields of

$$u(\xi = 0, \tau) = N \cdot \text{sech}(\tau) \quad (2.3.16).$$

These are higher-order (N^{th} -order) solitons [Shabat and Zakharov, 1972]. They can evolve periodically along the propagation direction [Stolen et al., 1983]. Fig. 2.1 (b) shows an example of $N = 3$.

If the initial pulse has a non-integer \tilde{N} (Eq. 2.3.9), it will evolve to a soliton of the closest integer N . When $\tilde{N} \leq 1/2$, no soliton will be formed. If the initial pulse is not a sech^2 pulse (note it is called sech^2 because $u \propto \text{sech}$ and $I = u^2 \propto \text{sech}^2$), it will evolve to the sech^2 shape. In the evolution of changing N , changing temporal shape, or changing both, the pulse adjusts its temporal shape, including the peak power and the duration, and in the end becomes a soliton that satisfies Eq. 2.3.9. A part of the pulse energy might disperse away in this process.

When more terms are added to Eq. 2.3.8, higher-order solitons may not propagate periodically, but instead break into N fundamental solitons [Kodama and Hasegawa, 1987]. These fundamental solitons are ejected from the main pulse one by one. This is called soliton fission which is one dominant process in SC generation in the anomalous GVD regime. In typical SC generation using a fs pump, major causes of soliton fission are intrapulse Raman scattering or higher-order dispersion.

Soliton fission length is the characteristic propagation distance at which soliton fission happens. It generally corresponds to where the higher-order soliton reaches its maximum bandwidth, or equivalently minimum temporal duration. A useful empirical expression of soliton fission length is [Dudley et al., 2006]:

$$L_{fiss} \sim \frac{L_D}{N} = \sqrt{L_D L_{NL}} = \sqrt{\frac{T_0^2}{|\beta_2| \gamma P_0}} \quad (2.3.17).$$

The initialization of soliton fission is interpreted as a process of modulation instability (MI) [Islam et al., 1989]. MI is a process whereby nonlinearity and anomalous GVD yields a gain spectrum on amplitude perturbations, causing amplification of spectral sidebands, and yielding modulation on the temporal profile and eventually breakup of the temporal profile into a train of sub-pulses.

2.3.4 Intrapulse Raman scattering

Raman scattering is inelastic scattering of photons. A photon interacts with a molecule, and causes it to transit to another vibration mode. Energy transfer thus happens between the photon and the molecule. When the molecule transits to a higher-energy mode and the photon has a red shift in its frequency, it is called Stokes Raman scattering; the opposite case is called anti-Stokes Raman scattering.

In the SC context, the specific mechanism based on the Raman effect is intrapulse Raman scattering [Gordon, 1986]. A pulse has a red shift, called Raman induced frequency shift (RIFS), because the blue edge of the pulse pumps the red edge. This can happen when the spectral bandwidth of the pulse is larger than $\omega_0 - \omega_s$ of the material. ω_0 is the pump frequency and ω_s is the Stokes frequency. Fig. 2.2 (a) shows typical soliton fission caused by the Raman effect.

If the pulse maintains a sech^2 shape, the RIFS can be calculated analytically:

$$\frac{d\Omega}{dz} \propto \frac{|\beta_2|}{T_0^4}, \quad (2.3.18),$$

in which Ω is the central frequency of the pulse, and T_0 is its duration. If the pulse has temporal broadening during propagation, the frequency shift saturates quickly due to the $\propto T_0^{-4}$ dependence. Fundamental solitons usually have big shifts because they maintain short duration. In the case of higher-order solitons, each ejected fundamental soliton has its own red shift after soliton fission. In a typical spectral evolution of SC in the anomalous regime, red-shifting soliton trajectories are obvious signatures. The shift is important in defining the bandwidth of SC at the long-wavelength side.

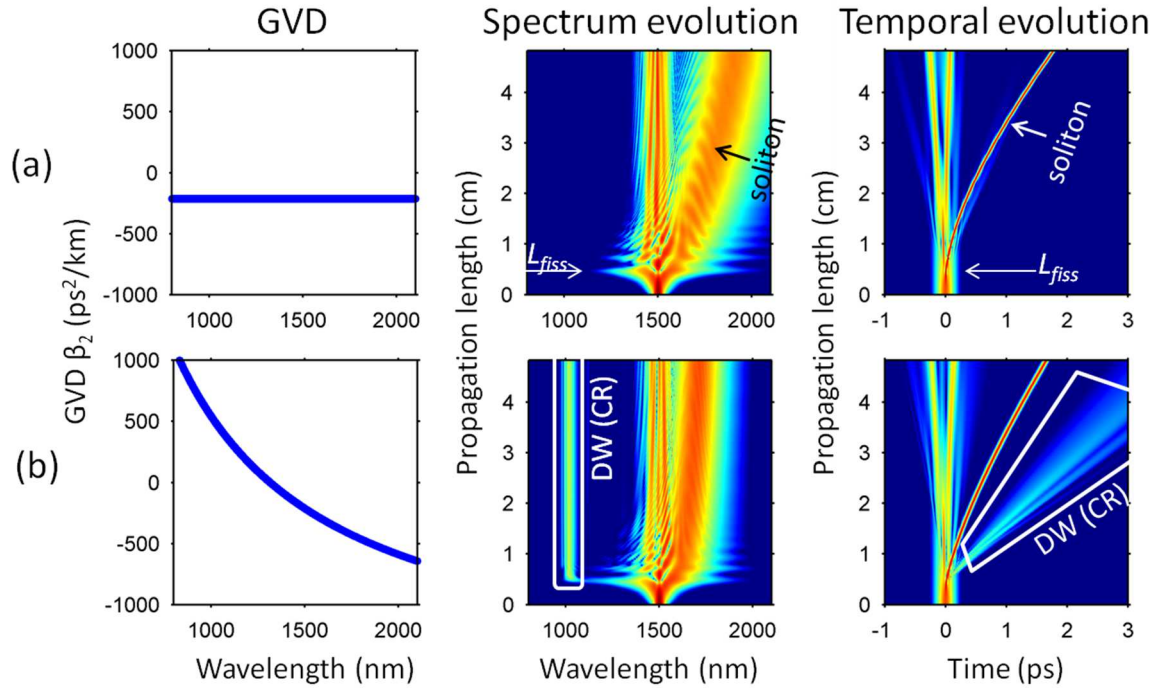


Fig. 2.2 (a) Adding the Raman term causes soliton fission. The spectral trajectory and temporal trajectory of a soliton are marked. The soliton fission length $L_{fiss} = 0.48$ cm is marked with white arrows. It can be seen this distance is where the pulse reaches the

maximum spectral width and the shortest duration before splitting, which is consistent with this empirical definition of soliton fission length. (b) Further adding 3rd-order dispersion causes dispersive wave (Cherenkov radiation) in addition to soliton fission. The dispersive wave is marked in spectral and temporal evolution.

2.3.5 Dispersive wave (Cherenkov radiation) generation

Under the perturbation of higher-order dispersions ($\beta_k |_{k \geq 3}$), solitons can induce resonant radiation in the normal GVD regime. The resonant radiation, called dispersive wave, has spectrally-narrow peaks with long temporal durations [Akhmediev and Karlsson, 1995]. The mechanism of dispersive wave generation was found to be equivalent to Cherenkov radiation. Thus is it often so called. Fig. 2.2 (b) shows typical graphical features of Cherenkov radiation in evolution plots.

The wavelength of the dispersive wave is determined by the phase-matching condition with the soliton. The dispersive wave defines the breadth of SC at the normal GVD side(s). In the soliton fission context, each ejected fundamental soliton has its own dispersive wave peak. If there are two ZDWs, which means two normal GVD regimes at both the red and the blue sides, each soliton can have two corresponding dispersive wave peaks in both of the normal GVD regimes [Skryabin et al., 2003].

2.4 Measurement of Coherence

2.4.1 Coherence of quasi-monochromatic light

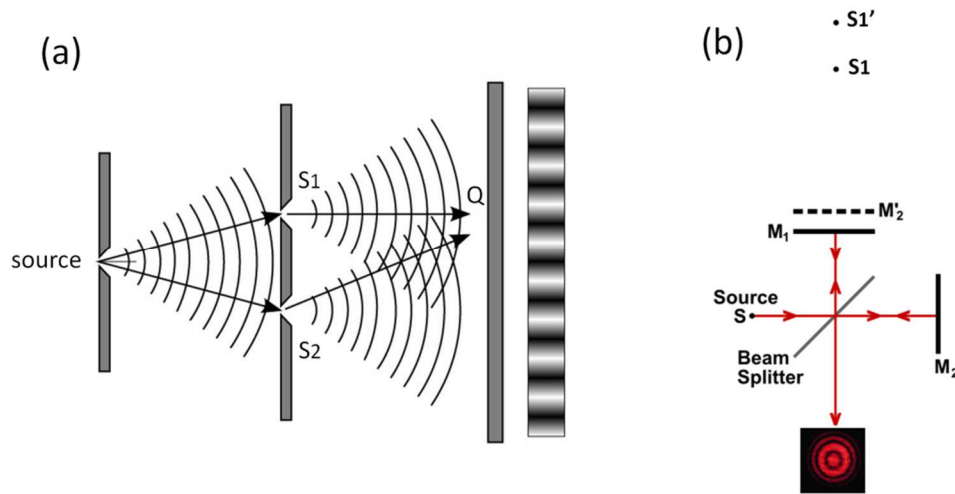


Fig. 2.3 Experiments of coherence measurement. (a) Young's double slit experiment; (b) Michelson interferometry. Source: (a) <http://www.physicsoftheuniverse.com/topics_quantum_quanta.html>; (b) <http://en.wikipedia.org/wiki/Michelson_interferometer>.

Coherence quantifies the phase correlation between two optical waves. Although SC is broadband, it is natural to start the discussion with the coherence of quasi-monochromatic light. This section is adopted and reorganized from textbooks [Alfano, 2005; Born and Wolf, 1999].

Young's experiment (Fig. 2.3 (a)) concerns secondary waves from two points in the primary field. Michelson's experiment (Fig. 2.3 (b)) considers the interference between a field and a delayed replica.

Suppose stationary fields at the slits of the Young's experiment are

$$E_1(t) = |E_1| \exp\{-i[\omega t + \phi_1(t)]\} \quad (2.4.1A),$$

$$E_2(t) = |E_2| \exp\{-i[\omega t + \phi_2(t)]\} \quad (2.4.1B),$$

where $|E_{1,2}|$ are real amplitudes, ω is the carrier frequency, and $\phi_{1,2}$ are initial phases.

The fields at point Q on the screen are

$$E_1(Q, t, L_1) = K_1 |E_1| \exp\{-i[\omega(t - L_1/c) + \phi_1(t - L_1/c)]\}$$

$$\Rightarrow E_1(Q, t) = |E_1(Q)| \exp\{-i[\omega t' + \phi_1(t')]\} = |E_1(Q)| \cdot E_1(t')/|E_1| \quad (2.4.2A),$$

$$E_2(Q, t, L_2) = K_2 |E_2| \exp\{-i[\omega(t - L_2/c) + \phi_2(t - L_2/c)]\}$$

$$\Rightarrow E_2(Q, t, \tau) = |E_2(Q)| \exp\{-i[\omega(t' - \tau) + \phi_2(t' - \tau)]\} = |E_2(Q)| \cdot E_2(t' - \tau)/|E_2| \quad (2.4.2B),$$

where L_1 and L_2 are the optical distances from S_1 and S_2 to Q, respectively. $t' = t - L_1/c$, and $\tau = (L_2 - L_1)/c$. K_1 and K_2 are constants containing the attenuation and the constant phase shift from the primary wave to the secondary waves.

The intensity on the screen is independent of time t :

$$\begin{aligned} I_{12}(Q, \tau) &= \left\langle [E_1(Q, t) + E_2(Q, t, \tau)]^* [E_1(Q, t) + E_2(Q, t, \tau)] \right\rangle_t \\ &= \left\langle |E_1(Q, t)|^2 \right\rangle_t + \left\langle |E_2(Q, t, \tau)|^2 \right\rangle_t + \left\langle E_1^*(Q, t) E_2(Q, t, \tau) + c.c. \right\rangle_t \\ &= I_1(Q) + I_2(Q) + \left\langle |E_1(Q)| |E_2(Q)| \exp\{-i[-\omega\tau + \phi_2(t' - \tau) - \phi_1(t')]\} + c.c. \right\rangle_t \\ &= I_1(Q) + I_2(Q) + 2|E_1(Q)| |E_2(Q)| \cdot \left\langle \cos[\omega\tau - (\phi_2(t' - \tau) - \phi_1(t'))] \right\rangle_t \quad (2.4.3). \end{aligned}$$

c.c. means the complex conjugate term. The time average with respect to t $\langle \rangle_t$ is added, because detectors are slow compared to the oscillation of the field. In the following the subscript t is omitted.

For coherent light, the difference in the initial phases $\phi_2(t' - \tau) - \phi_1(t')$ is constant and $\langle \rangle$ can be removed, yielding a term of cosine fringes (the last term of Eq. 2.4.3). Changing $\phi_2(t' - \tau) - \phi_1(t')$ causes the fringes to shift in the direction perpendicular to the fringes. Incoherent or partially coherent light has fast fluctuation of $\phi_2(t' - \tau) - \phi_1(t')$, lowering the contrast of the fringes. In this case, the last term of Eq. 2.4.3 can be evaluated by introducing the mutual coherence function

$$\Gamma_{12}(\tau) = \langle E_1^*(t')E_2(t' - \tau) \rangle = |\Gamma_{12}(0)| \exp\{i[\omega\tau + \Psi_{12}(\tau)]\} \quad (2.4.4),$$

where $\Psi_{12}(\tau) = \arg[\Gamma_{12}(\tau)]$. Note $E_{1,2}$ here are the fields at S_1 and S_2 as defined in Eq. 2.4.1, not the fields at the screen $E_{1,2}(Q)$ as in Eq. 2.4.2. The intensity at Q is measured to infer the coherence of fields at S_1 and S_2 . When subscript 1 = subscript 2, $\Gamma_{11}(\tau) = \langle E_1^*(t)E_1(t - \tau) \rangle$ is the autocorrelation function, or called self-coherence function.

When subscript 1 = subscript 2 and $\tau = 0$, $\Gamma_{11}(\tau = 0) = \langle E_1^*(t)E_1(t) \rangle = I_1$ is the intensity.

Using the definition in Eq. 2.4.4, Eq. 2.4.3 becomes

$$\begin{aligned} I_{12}(Q, \tau) &= I_1(Q) + I_2(Q) + 2 \frac{|E_1(Q)||E_2(Q)|}{|E_1||E_2|} \cdot |\Gamma_{12}(\tau)| \cos[\omega\tau + \Psi_{12}(\tau)] \\ &= I_1(Q) + I_2(Q) + 2 \frac{\sqrt{I_1(Q)I_2(Q)}}{\sqrt{I_1I_2}} \cdot |\Gamma_{12}(\tau)| \cos[\omega\tau + \Psi_{12}(\tau)] \end{aligned} \quad (2.4.5).$$

The coherence function $\Gamma_{12}(\tau)$ can be normalized by introducing

$$\gamma_{12}(\tau) = \frac{\Gamma_{12}(\tau)}{[\Gamma_{11}(0)\Gamma_{22}(0)]^{1/2}} = \frac{\Gamma_{12}(\tau)}{|E_1||E_2|} = \frac{\Gamma_{12}(\tau)}{\sqrt{I_1I_2}} \quad (2.4.6).$$

And Eq. 2.4.5 becomes

$$I_{12}(Q, \tau) = I_1(Q) + I_2(Q) + 2\sqrt{I_1(Q)I_2(Q)} \cdot |\gamma_{12}(\tau)| \cos[\omega\tau + \Psi_{12}(\tau)] \quad (2.4.7).$$

The term $I_1(Q) + I_2(Q)$ is the DC portion, and the last term is cosine fringes. The period of the fringes is

$$\Delta\tau = 2\pi/\omega \quad (2.4.8).$$

The visibility/contrast of the fringes is

$$V(\tau) = \frac{(I_{\max} - I_{\min})}{(I_{\max} + I_{\min})} = \frac{2\sqrt{I_1(Q)I_2(Q)}}{I_1(Q) + I_2(Q)} |\gamma_{12}(\tau)| \quad (2.4.9).$$

$|\gamma_{12}(\tau)|$ only depends on the phase correlation. $\frac{2\sqrt{I_1(Q)I_2(Q)}}{I_1(Q) + I_2(Q)}$ is a factor representing the intensity imbalance, which equals 1 when $I_1(Q) = I_2(Q)$. These two factors together determine the fringe contrast.

To apply the above discussion to Michelson interferometry, one just needs to replace subscript 2 with 1.

2.4.2 Coherence of broadband light

Broadband radiation can be expressed as a Fourier integral:

$$E(t) = \int \tilde{E}(\omega) d\omega/2\pi = \int |E(\omega)| \exp\{-i[\omega t + \varphi(\omega)]\} d\omega/2\pi \quad (2.4.10).$$

For interference of broadband radiation, the source fields $E_{1,2}(t)$ and the fields on the screen $E_{1,2}(Q, t)$ in Section 2.4.1 can all be expressed in this form. The interference signal

is thus the superposition of fringes of each frequency (Fig. 2.4 (a)). Because the overlapping fringes of each frequency have different periods: $\Delta\tau = 2\pi/\omega$ (Eq. 2.4.8), they become indistinguishable.

We can spectrally resolve the signal in the direction parallel to the fringes, and obtain 2D $I(x, \omega)$, as in Fig. 2.4 (b). For fringes at each frequency, it is reduced to a monochromatic interference problem. Eq. 2.4.9 can be used to calculate the coherence $|\gamma_{12}(\tau)|$ for each frequency, and combine the results to obtain $|\gamma_{12}(\tau, \omega)|$.

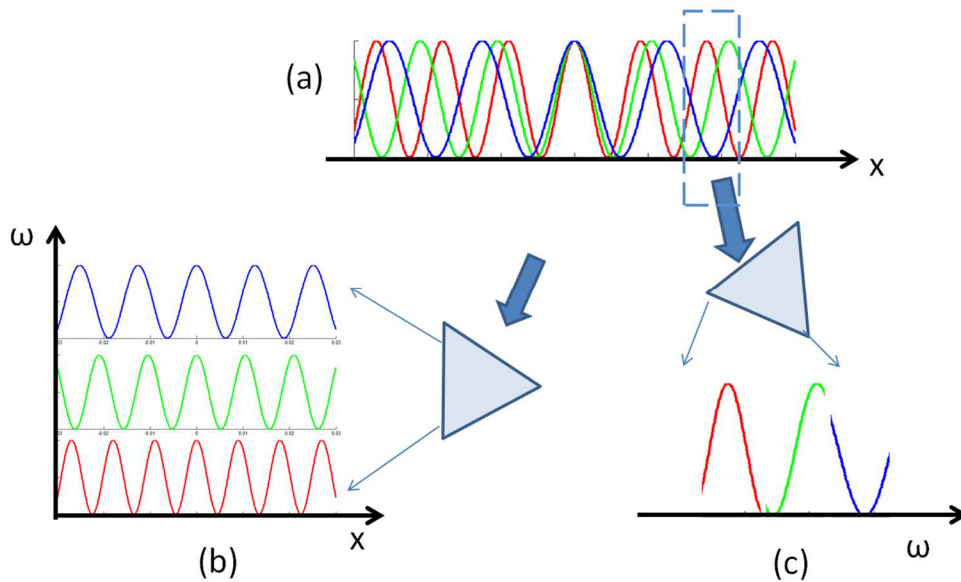


Fig. 2.4 Methods to measure frequency-dependent coherence for broadband light. (a) Interference of broadband light yields overlapped fringes of all frequencies. (b) Spectrally resolve the signal along the direction of fringes (here vertically) to obtain a 2D pattern. At horizontal line is the fringe of a frequency. (c) Spectrally resolve the fringes in the direction perpendicular to the fringes (here horizontally), resulting in a spectrum with fringes. Prisms are used to conceptually illustrate spectrally resolving the signal.

Or one can spectrally resolve the fringes in the direction perpendicular to the fringes (Fig. 2.4 (c)). The result can be described in the frequency domain:

$$I_{12}(Q, \omega) = I_1(Q, \omega) + I_2(Q, \omega) + 2\sqrt{I_1(Q, \omega)I_2(Q, \omega)} |g_{12}(\omega)| \cos[\omega\tau - \delta_{12}(\omega, \tau)] \quad (2.4.11),$$

in which $I_{1,2}(Q, \omega)$ are the spectra on the screen. And

$$g_{12}(\omega) = \frac{\langle \tilde{E}_1^*(\omega) \tilde{E}_2(\omega) \rangle}{\sqrt{I_1(\omega)I_2(\omega)}} \quad (2.4.12)$$

is the spectral degree of coherence. Eq. 2.4.11 has a similar form as Eq. 2.4.8, and also it can be obtained by performing the Fourier transform on Eq. 2.4.8.

In experiment, the interference signal is sent into a spectrometer, and a spectrum with fringes is shown. The fringe period is

$$\Delta\omega = 2\pi/\tau \quad (2.4.13).$$

And the visibility/contrast is

$$V(\omega) = \frac{(I_{max} - I_{min})}{(I_{max} + I_{min})} = \frac{2\sqrt{I_1(Q, \omega)I_2(Q, \omega)}}{I_1(Q, \omega) + I_2(Q, \omega)} |g_{12}(\omega)| \quad (2.4.14).$$

$|g_{12}(\omega)|$ involves only the phase correlation; and $\frac{2\sqrt{I_1(Q, \omega)I_2(Q, \omega)}}{I_1(Q, \omega) + I_2(Q, \omega)}$ represents the intensity imbalance. These two factors together determine the fringe contrast.

2.4.3 Coherence of SC

SC coherence usually refers to the pulse-to-pulse coherence, namely, $\tilde{E}_1(\omega)$ and $\tilde{E}_2(\omega)$ in Eq. 2.4.12 refer to two independently generated SC pulses. A popular experimental

scheme is to use two successive pump pulses to generate two SC pulses in the same medium, and these SC pulses yield interference. In the simulations, two independently generated SC pulses are modeled by repeatedly solving the GNLSE with independent noise seeds.

The pump for SC, usually a mode-locked laser, is coherent pulse-to-pulse. So the interest is: can this coherence be maintained during the SC generation process? Despite the complexity of SC generation, it has been shown that the coherence can be maintained in some circumstances. The mechanism of coherence degradation has been investigated by experiments and by simulations, as reviewed in Chapter 3.

3. BACKGROUND

SUMMARY

This chapter reviews previous research about supercontinuum (SC) coherence, and introduces the motivation for my research.

3.1 reviews simulation research of SC coherence. Coherence properties depending on various parameters were shown. And a few theories were developed based on them, as compiled in Table 3.1.

3.2 reviews experimental research of SC coherence (compiled in Table 3.2). Most of the experiments have shown coherence measured under a limited collection of conditions (e.g., at several levels of SC power), and are unable to show evolving trends and some subtle features. This limits detailed discussion about the coherence. Discussions in a lot of previous experimental research are based on spectrally-averaged coherence.

3.3 introduces the motivation of my research. Evolution of the spectrum and the coherence was measured by continuously tuning the SC power. These data are expected to visualize the dynamics and allow for detailed comparison with simulations. The dependence of coherence on the propagation length was investigated by using different lengths of fibers.

3.1 Simulation Research of SC Coherence

SC coherence can be modeled by repeatedly solving the GNLSE with independent noise seeds and then calculating the coherence using Eq. 2.4.12. Major noise sources include quantum-limited shot noise in the pump, spontaneous Raman noise along the propagation, and pulse-to-pulse fluctuation of the pump power (technical noise).

The Dudley group [Dudley and Coen, 2000a and 2000b; Dudley et al., 2006] used $|g_{12}|$ to quantify SC coherence. Quantum noise and Raman noise were added [Drummond and Corney, 2001]. Raman noise was found to have little impact on the coherence. Technical noise was not included.

Contour plots of $|g_{12}(\lambda, L)|$ were shown, in which L is the propagation distance (Fig. 3.1 (a) and (b)). These evolution data show changing trends of coherence along the propagation distance. Coherence evolution compared to corresponding spectral evolution can show connections between coherence properties and spectral behaviors. The dependence of coherence on pump pulse duration T_0 and pump wavelength λ_0 was investigated (Fig. 3.1 (c)).

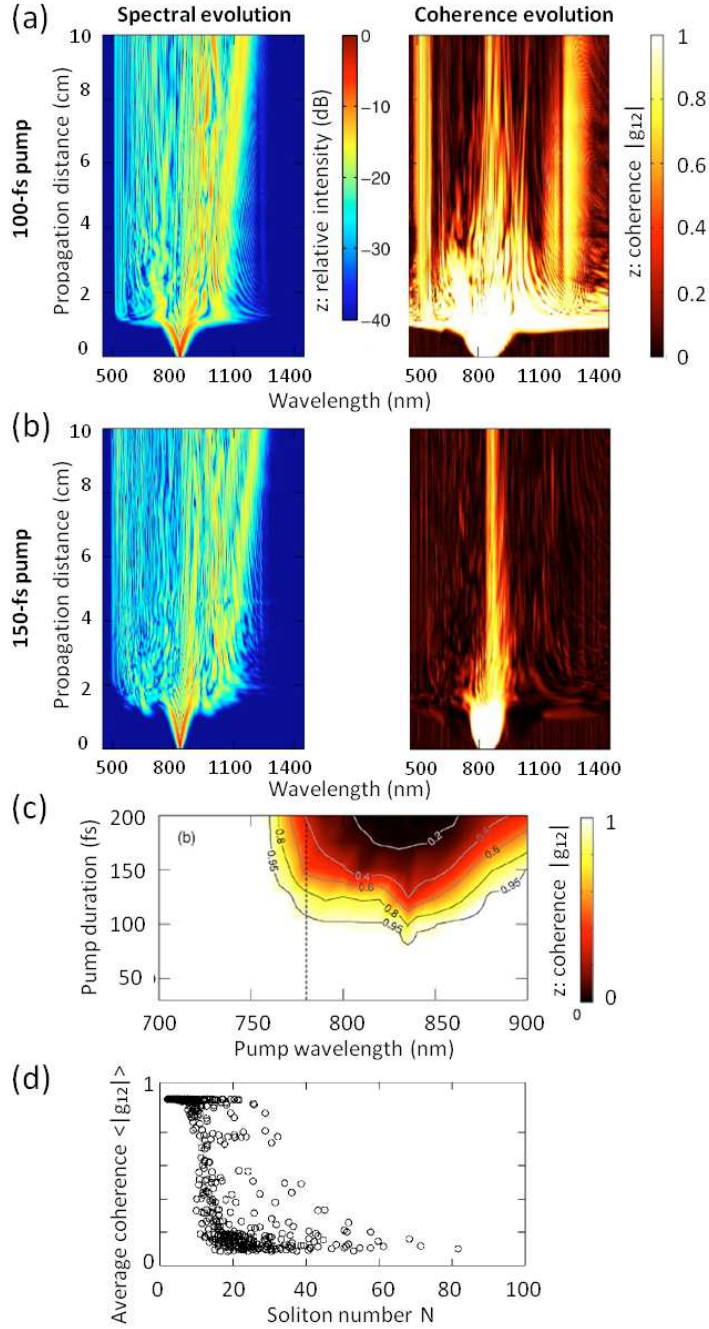


Fig. 3.1 Simulation results of SC coherence, excerpted from [Dudley et al., 2006]. (a) and (b): Spectral and coherence evolution using a 100-fs and a 150-fs pump, respectively. The pump peak power is 10 kW. The ZDW of the PCF is 780 nm, and the pump wavelength is 835 nm (anomalous GVD pump). (c) Contour plot of average coherence as a function of the pump wavelength and the pump pulse duration. The pump peak power is fixed to be 4 kW. The ZDW of the PCF is 780 nm (marked with a dash line). (d) Average coherence vs. soliton number N , summarized from multiple simulations using various

parameter sets, in which the pump wavelength is ranged 790–900 nm, pump pulse duration is 30–200 ns, and pump peak power is 3–30 kW.

The following dynamics were found from the results. (1) Shorter pump pulse duration produces higher coherence. This can be seen by comparing Fig. 3.1 (a) and (b). At a propagation distance $L \gg L_{fiss}$, 50-fs pump yields SC of nearly perfect coherence using the parameter set they used (Fig. 3.1 (a)).

(2) Soliton fission can cause dramatic coherence degradation, as in Fig. 3.1 (b).

(3) Pumping in the normal GVD regime generates SC of nearly perfect coherence. Moving the pump wavelength into the anomalous GVD regime yields coherence degradation; however, moving the pump wavelength further into the anomalous GVD regime restores the coherence. This can be seen in Fig. 3.1 (c).

These dynamics can be explained by a unified story. SPM is a coherence-maintaining process; while MI can amplify noise. In the normal GVD regime, MI is prohibited, and coherence is high. In the anomalous GVD regime, if MI is significant before the broadening spectrum covers the MI gain spectrum, MI amplifies the noise background, causing coherence degradation. If MI is significant after the pulse has broadened to cover the MI gain spectrum, MI amplifies coherent radiation, yielding coherent output. Because dramatic spectral broadening is associated with soliton fission, the criterion of coherence is based on comparing the characteristic length of MI (L_{MI}) with the characteristic length of soliton fission (L_{fiss}). Coherence is high when $L_{MI} \gg L_{fiss}$, or equivalently the soliton number

$$N \ll 16 \tag{3.1.1},$$

considering $L_{fiss} \sim L_D/N$ and $L_{MI} \sim 16L_{NL}$. Soliton number thus is a criterion of coherence. Average coherence vs. soliton number is plotted in Fig. 3.1. (d) by compiling results using various parameter sets. Each parameter set includes pump wavelength, pump pulse duration, and pump peak power.

Gu et al. (2003) simulated SC coherence to match with experiment. It was found that adding quantum noise alone causes almost no coherence degradation (because the short pump pulses used here $T_{FWHM} = 60$ fs). Adding 2% pump power fluctuation yields the same average coherence degradation as measured.

Türke et al. (2007) reported simulations of SC coherence using varying pump pulse duration T_0 and pump peak power P_0 , and compared them with experimental results. A fixed propagation length $L \gg L_{fiss}$ and a pump in the anomalous GVD regime were used. The experimental and the simulated results are similar to that in [Dudley and Coen, 2000a and 2000b; Dudley et al., 2006], if we replace the propagation distance L in Fig. 3.1 (a) and (b) with the pump power. With a 148-fs pump, the coherence remains high when the SC almost reaches its maximum span; after that, coherence degradation occurs. With a 410-fs pump, the coherence degrades as soon as the spectrum is relatively broad.

This paper [Türke et al., 2007] discussed the coherence of Cherenkov radiation, and argued that the coherence degradation of Cherenkov radiation is due to XPM with solitons. Specifically, although each Cherenkov peak is induced by one corresponding soliton, any Cherenkov peak interacts with the sum of all solitons through XPM. The parameters of the solitons vary pulse-to-pulse depending on noise, causing phase fluctuation in the Cherenkov radiation. Larger soliton number is associated with more

interference effect when adding solitons up. This explains why larger soliton numbers are associated with larger coherence degradation.

The authors also explained why coherence degradation of Cherenkov radiation should not be explained by Dudley's MI theory. In the 410-fs pump case in this paper (Fig. 3.2 (c)), the MI-induced sidebands are weak when soliton fission happens. The ejected solitons are coherent, but the corresponding Cherenkov radiation is incoherent. This needs to be explained by the XPM theory above.

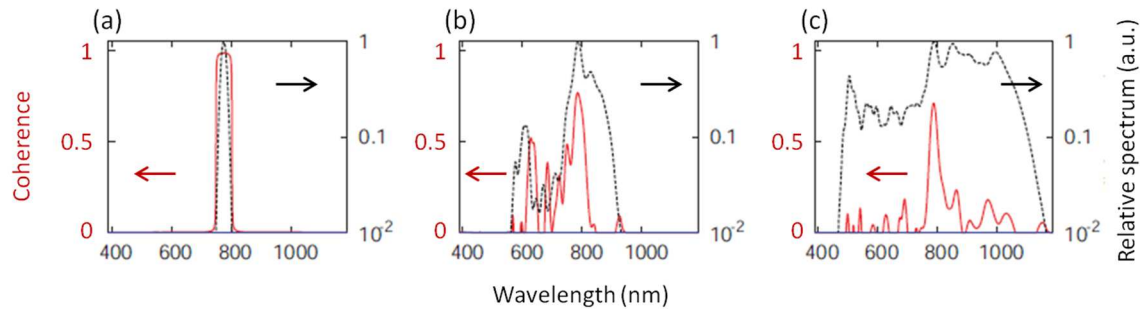


Fig. 3.2 Simulated SC and its coherence, excerpted from [Türke et al., 2007]. A 410-fs pump at 775 nm was used, and the pump peak powers are (a) 0.09 kW, (b) 0.9 kW, and (c) 5.9 kW. The fiber length is 9 cm. The authors argued that in the case of (c), the MI-induced sidebands are weak when soliton fission happens, and the ejected solitons are coherent.

I argue that this explanation needs more evidence. The solitons (radiation at the longer-wavelength side of the pump) in Fig. 3.2 (c) and even (b) appear to be incoherent. Also, the fact that MI-induced sidebands are weak does not guarantee that the soliton fission is coherent. There has not been investigation about how large MI-induced sidebands need to be in order to cause incoherent soliton fission, as far as I know.

Kobtsev et al. (2005) performed simulations to explain perfect soliton coherence and low non-solitonic coherence measured in their experiment. They argued low coherence is due

to fast spectral oscillations in the non-solitonic region. The simulations showed oscillation of periods $\Delta\omega \sim 0.5\text{--}1$ THz in the non-solitonic region of spectra, caused by interference between components of close frequencies in the SC. Fluctuation in the pump power causes these fine structures to shift, and the interference visibility/contrast is reduced when successive pulses have different intensities at a certain frequency. Note this intensity inequality cannot be factored out in the data processing (see Eq. 2.4.14), because the fast-changing fine structures are undetectable in the experiment, due to averaging.

	[Dudley et al., 2006]	[Türke, et al., 2007]	[Kobtsev et al., 2005]
Noise added	- Shot noise - Raman noise	- Shot noise - Pump power fluctuation	- Shot noise - Pump power fluctuation
Results	(1) Shorter pump duration yields higher coherence. (2) Coherence degradation is associated with soliton fission. (3) Coherence is restored when pump wavelength moves deep into anomalous GVD regime.	Solitons are coherent, and Cherenkov radiation has low coherence. (Their data did not explicitly demonstrate this.)	Solitons have perfect coherence, while non-solitonic region has low coherence
Theory	Coherence depends on whether MI is significant before soliton fission. A larger soliton number is associated with greater degradation of coherence.	Cherenkov radiation has coherence degradation because it interacts with the sum of all solitons through XPM.	Fine spectral structures cause coherence degradation in non-solitonic region.

Table 3.1. Summation of previous simulation research and their theories.

A summation of the simulation research and the theories is listed in Table 3.1.

Besides these papers, many experiment-based papers performed simulations to match and to interpret experimental results, as introduced in the following section. Most of them used theories similar to Dudley's.

3.2 Experimental Research of SC Coherence

Experimental research using various parameter sets exists in the literature. Most authors used the Young's or the Michelson interferometry set up (see Fig. 2.4). A brief summary is in Table 3.2.

paper	[Gu et al., 2003]	[Lu and Knox, 2004]	[Kobtsev et al., 2005]	[Zeylikovich et al., 2005]		[Nicholson and Yan, 2004]		[Türke, et al., 2007]	
λ_0 (nm)	800	780, 820, 860, 920	835, 795	1560	780	1550		800	
T_{FWHM} (fs)	60	100	50	120	90	2000	188	148	410
P_0 (kW)	14.7	12.3	52.8	0.5	0.062	0.025	0.093, 4.7	0.8, 2.5, 5.9, 7.6, 13	0.3, 0.9, 2.1, 2.7, 5.5
f_{rep} (MHz)	90	80	100	48	48	50	50	80	80
P_{ave} (mW)	90	112	300	3.3	0.3	2.8	1, 50	11, 34, 80, 102, 175	11, 34, 78, 101, 205
E_{pulse} (nJ)	1	1.4	3	0.068	0.0063	0.056	0.02, 1	0.14, 0.42, 1.0, 1.3, 2.2	0.14, 0.42, 1.0, 1.3, 2.6
ZDW (nm)	770	820	< 795	Two ZDWs: 740, 1700		(anomalous pump)	-	730	
L_{fiber}	18 cm	6 cm tapered fiber	30 cm	1.5 m		1km	6 m hybrid	30 cm tapered fiber	
Average $ g $	0.56	High, lower, 0.15, 0.7, Respectively	1 at solitons	0.98	High $ g $ only around λ_{pump}	~ 0.1	~ 0.9	Changes from high to low when power increases	becomes lower at lower powers
Conclusion	Simulations showed fluctuation in pump power is major source of noise	Coherence recovery when moving pump wavelength deep into anomalous GVD	Perfect coherence at solitons' central wavelengths. (small soliton number $N \sim 3$)	Similar to [Lu and Knox, 2004], with pumps of low peak powers		Short pump pulses yield high coherence.		Similar to [Nicholson and Yan, 2004]. Cherenkov radiation has low coherence.	

Table 3.2. Key facts of previous experimental research on SC coherence.

Bellini and Hansch (2000) measured the coherence between two independent SC generated at two separate points in a bulk material, using the Young's scheme. With a

grating, distinct fringes at all wavelengths were obtained (Fig. 2.4 (b)), qualitatively demonstrating the coherence of SC.

Gu et al. (2003) measured coherence of SC in a PCF for the first time, and performed simulations to show the main cause of coherence degradation is the pulse-to-pulse fluctuation of the pump power. In the experiment, replica pump pulses were used to generate SC in two identical PCFs. Interference was performed in the Young's scheme. Spectrally-resolved fringes were recorded (Fig. 2.4 (b)), and $|g_{12}(\lambda, \tau \square 0)|$ was calculated. Using a pump of 60-fs duration, the average coherence was 0.56. Numerical simulations were performed to match the experimental results. Adding quantum noise resulted in almost perfect coherence; further adding 2% fluctuation of pump power reproduced the average coherence in experiment. This showed that coherence degradation is mainly caused by the fluctuation of the pump power.

It is a limitation that the two-fiber scheme in [Gu et al., 2003] cannot guarantee identical $\tilde{E}_1(\lambda)$ and $\tilde{E}_2(\lambda)$ up to a normalization constant. In the two-fiber scheme, a beam splitter was used to split the pump, and the replica beams are coupled into two PCFs that were carefully made identical. But a beam splitter usually cannot make an exact 50/50 split. Specifically in [Gu et al., 2003], there was a large difference in the power coupled into each PCF: 0.25 and 0.58 nJ. Also it is hard to ensure the same coupling efficiency in two PCFs, the same fiber orientation of the two PCFs, etc. As a result, the independently generated SC $\tilde{E}_1(\lambda)$ and $\tilde{E}_2(\lambda)$ have quite different spectra, making the discussion of coherence complicated. For example in Fig. 4, radiation at 930 nm is a soliton in $\tilde{E}_1(\lambda)$

but is not a soliton in $\tilde{E}_2(\lambda)$, thus the physical meaning of $|g_{12}(\lambda=930 \text{ nm})|$ is complicated.

I think the difference between $\tilde{E}_1(\lambda)$ and $\tilde{E}_2(\lambda)$ might be responsible for part of the coherence degradation.

Lu and Knox (2004) showed the coherence recovery caused by moving the pump wavelength deep into the anomalous GVD regime. This result was later reproduced by simulations [Dudley et al., 2006]. In this experiment, a one-fiber scheme was used for SC generation. The pump was sent into a fiber for SC generation. Successive SC pulses $\tilde{E}_1(\lambda)$ and $\tilde{E}_2(\lambda)$ interfere in a Michelson interferometer, and the signal was measured with an OSA. This scheme ensures that $\tilde{E}_1(\lambda)$ and $\tilde{E}_2(\lambda)$ are SC generated under exactly the same condition, except for different noise seeds. The unequal beam splitting in the interferometer only yields different normalization constants on $\tilde{E}_1(\lambda)$ and $\tilde{E}_2(\lambda)$, which can be factored out in the data processing. Most of later experiments used this configuration to measure SC coherence.

Zeylikovich et al. (2005) showed similar results to [Lu and Knox, 2004], using a different parameter set.

Kobtsev et al. (2005) measured the coherence at the central wavelengths of solitons and at second harmonic wavelengths of the solitons. Using a 50-fs pump, the soliton number is small $N \sim 3$. Nearly perfect coherence was measured at the central wavelengths of the solitons, which is as expected according to Eq. 3.1.1. The second harmonic wavelengths of the solitons are in the non-solitonic region. Considerable coherence degradation was shown at these wavelengths. The paper explained that this is due to the fast spectral

oscillation in the non-solitonic region, as introduced in Section 3.1. Simulations showed pump power fluctuation of $\sim 0.5\%$ was enough to reproduce the experimental coherence degradation in the non-solitonic region.

[Nicholson and Yan, 2004] and [Nicholson et al., 2008] investigated the coherence of all-fiber-based SC using doped fibers. The 2004 paper showed that SC generated by a fs pump has much higher coherence than SC by a ps pump. Fibers of different dispersion properties were spliced together for dispersion management. A piece of SMF of a proper length was used to compress the pump pulse before it is coupled into the fiber for SC generation. The 2008 paper investigated optimization of the pulse compression to generate high-coherence SC.

Türke et al. (2007) measured the coherence of SC using two different pump pulse durations and selected pump powers. The shorter-duration pump produced higher coherence than the longer-duration pump, similar to [Nicholson and Yan, 2004].

A summary of the above experimental research is in Table 3.2. I think there are some limitations of these experiments. (1) The tuning of parameters is limited, due to practical difficulties. No gradually-changing evolution of the coherence was measured to compare with simulated evolution such as Fig. 3.1. (a) and (b). (2) No previous experiments investigated the effect of using different fiber lengths, especially short fibers approaching the soliton fission length.

3.3 My Research

My research focuses on the undone things mentioned in the last paragraph.

(1) Tune the SC power continuously to obtain evolution of spectra and of coherence. It is expected that the evolution visualize coherence dynamics and allow detailed comparisons with simulations. Detailed discussions about the coherence mechanisms are thus possible.

(2) Investigate the coherence properties depending on the fiber length, with especial attention on short PCFs of $L_{fiber} \sim L_{fiss}$. Simulations have shown that coherence degradation is associated with soliton fission. Using fiber lengths close to the soliton fission length is expected to clearly show the coherence degradation process, and to show what fiber length can yield SC of high coherence.

4. METHODS

SUMMARY

4.1 describes the experimental procedure. Based on the setups in previous research, some improvement is made by using the Mach-Zehnder interferometer and using wedge beam splitters (Fig. 4.3).

4.2 describes the methods of numerical simulation. Section 4.2.2 and 4.2.3 introduce how to obtain the dispersion term and the Raman term, respectively. A summary of all parameters for simulation is listed in Section 4.2.4. Section 4.2.5 introduces how to model noise and calculate coherence.

4.1 Experiment

The PCFs in my experiment are: highly nonlinear SF6 PCFs of different lengths: 10.5 cm, 4.7 mm, 3.9 mm, and 1.0 mm, and a highly nonlinear Tellurite PCF of 2.7 cm.

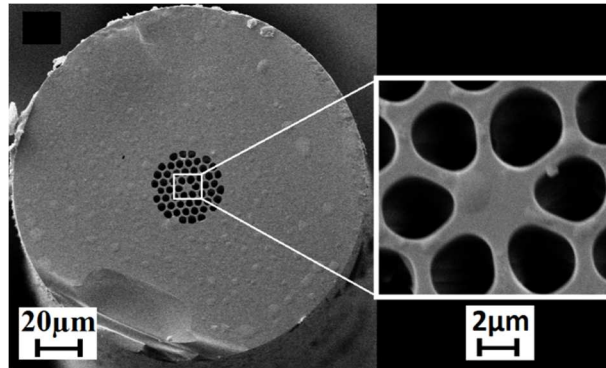


Fig. 4.1. SEM picture of the cross section of the SF6 PCF. Inset is a close-up of the core. The core diameter is 3.6 μm.

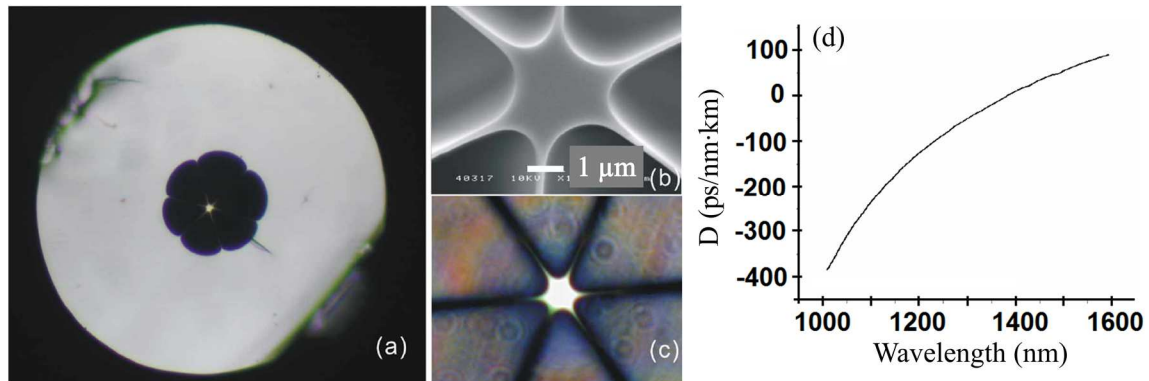


Fig. 4.2. Microstructure and the dispersion of the Tellurite PCF. (a) Cross section of the fiber under an optical microscope. (b) and (c) are closeups of the core under SEM and under an optical microscope, respectively. (d) is the dispersion curve. The ZDW is 1380 nm. These figures are excerpted from [Domachuk et al., 2008].

Key information about these PCFs is compiled in Table 4.1, in comparison with two silica PCFs and another SF6 PCF. The microstructures and the dispersion curve are shown in Fig. 4.1 and 4.2. How to calculate the dispersion curve of the SF6 PCF is

introduced in Section 4.2.2. The tellurite PCF was previously reported in [Kumar et al., 2003; Domachuk et al., 2008], where the dispersion curve was reported.

	Silica PCF	SF6 PCF	SF6 PCF	Tellurite PCF	Equations
Reported in	[Dudley et al., 2006; Ranka et al., 2000]	[Kumar et al., 2002; Omenetto et al., 2006; Moeser et al., 2007]	N.A.	[Kumar et al., 2003; Domachuk et al., 2008]	
d_{core} (μm)	1.6 (1.7 [Ranka])	2.6	3.6	2.5	
$n_2 \cdot 10^{-20}$ m^2/W	3	22	22	25	
γ (/km·W)	110	167.97	87.6	596	$\gamma = \frac{2\pi n_2}{\lambda_0 A_{eff}}$ A_{eff} = core area of fiber
ZDW (nm)	780 (767 [Ranka])	1300	~1300	1380	
β_2 (ps^2/km)	-11.83	-73.9248	-48.39	-92.19	
β_3 (ps^3/km)	0.081	0.2434	0.305	0.6411	
λ_0 (nm)	835 (790 [Ranka])	1550			
P_{ave} (mW)	70			50	
P_0 (kW)	7			5	
T_{FWHM} (fs)	110				$T_0 = T_{FWHM} / 1.763$
L_{NL} (mm)	1.3	0.85	1.6	0.34	$L_{NL} = 1/\gamma P_0$
L_D (mm)	329	52.7	80.4	42.2	$L_D = T_0^2 / \beta_2 $
N	15.9	7.9	7.02	11.2	$N = \sqrt{L_D / L_{NL}}$
L_{fiss} (mm)	20.7	6.7	11.5	3.8	$L_{fiss} = L_D / N$ $= \sqrt{L_D L_{NL}}$
L_{fiber} (mm)		5.7 17	1 3.9 4.7 105	27	
L_{fiber}/L_{fiss}		0.85 2.5	0.087 0.34 0.41 9.1	7.1	

Table 4.1. Parameters of the PCFs and the pump used in the experiment, in comparison with a silica PCF and a SF6 PCF in literature. In the column of the silica PCF, the parameters are for the fiber used in [Dudley et al., 2006] if not otherwise noted.

Note these parameters may need correction when matching simulations to experimental results.

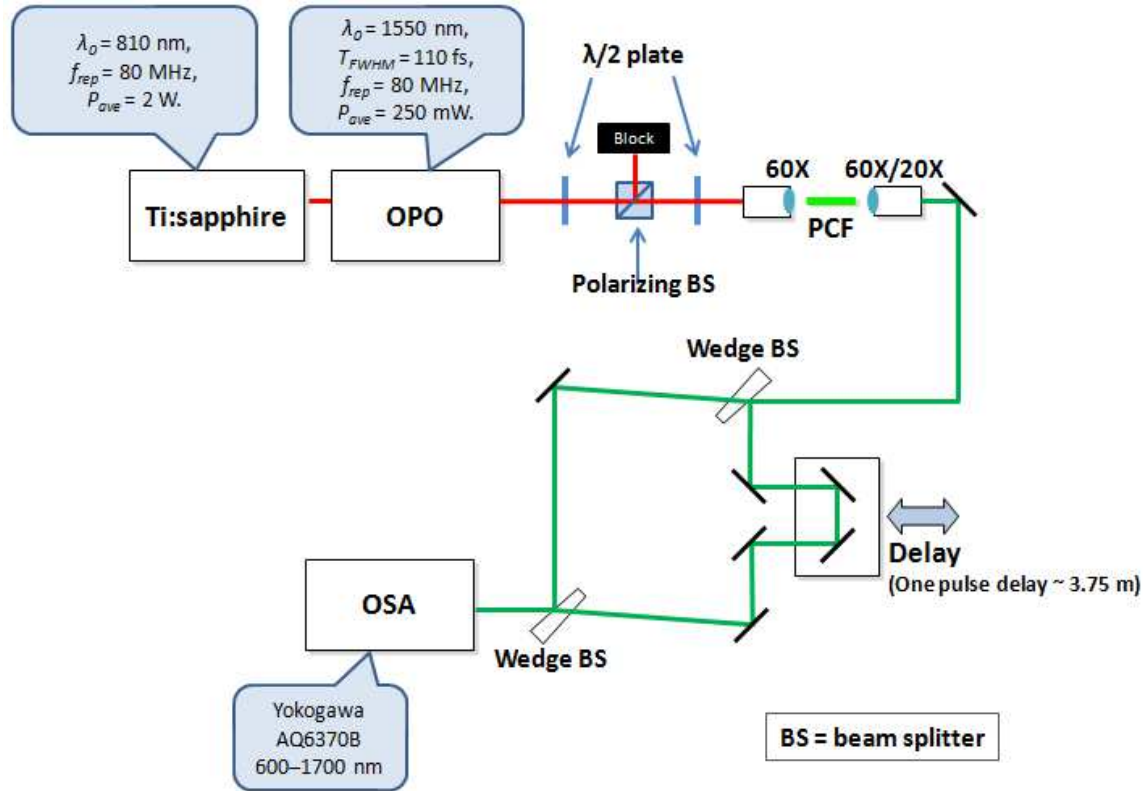


Fig. 4.3. Experimental setup for the measurement of SC coherence.

I used the delayed-pulse method to perform interference between successive SC pulses generated in one PCF, and measured the spectral fringes using an OSA. The setup (Fig. 4.3) is similar to that in [Lu and Knox, 2004]. An OPO pumped by a mode-locked Ti:sapphire laser generates laser pulses at $\lambda_0 = 1550$ nm, of duration $T_{FWHM} = 110$ fs, at a repetition rate $f_{rep} = 80$ MHz, and with an average power of 250 mW. $\lambda_0 = 1550$ nm is in the anomalous GVD regimes of the SF6 PCF and the tellurite PCF used in the experiment.

A combination of a half wave plate and a polarizer was used to continuously tune the laser power sent into the PCF. Another half wave plate was used to tune the polarization of the pump. A 60X aspherical lens was used to couple the laser into the PCF. And another 60X aspherical lens was used for collimation. The power efficiency of SC generation is ~30% for all fibers, when coupling loss and collimation loss are included.

The fibers were hand cleaved. In a usual hand cleave, one presses the fiber onto the blade with a finger, scratches the fiber gently with a scribe, and bends the blade to break the fiber. It becomes challenging to cleave sub-cm fibers because fingers easily touch and might damage the facets. I used narrow strips of tape to “press” the fiber onto the blade, and scratched the fiber carefully while monitoring it under microscope. The tape also helped to handle the fiber. I was able to cleave fibers as short as ~1 mm.

Sub-cm PCFs were mounted on customized stages of proper sizes; longer PCFs were mounted on commercial fiber clamps. Using tape to mount the sub-cm fiber onto the stage is usually better than using glue (Fig. 4.4). Glue usually dries fast and uncontrollably, while using tape allows fine adjustment of the position and especially the orientation of the fiber.

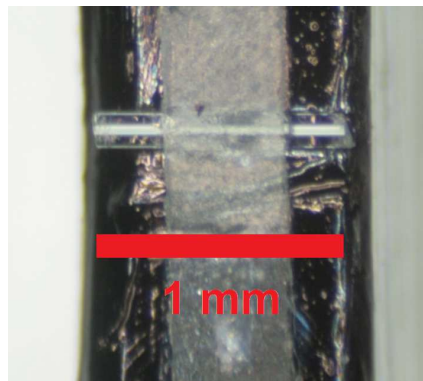


Fig. 4.4. 1-mm SF6 PCF mounted on a customized stage using tape.

A Mach–Zehnder interferometer with a one-pulse delay ($z = c/f_{rep} \sim 3.75$ m, with $f_{rep} = 80$ MHz) was built. By using wedge beam splitters, instead of plate, cube, or pellicle beam splitters, ghosting was mitigated. The Mach–Zehnder design balances the dispersion in two arms - each beam penetrates the splitter once. The interferometer output was measured with an OSA (Yokogawa AQ6370B) with a range of 600–1700 nm.

The interference signal $I_{12}(\omega)$ shows fringes with a contrast/visibility as in Eq. 2.4.14.

$I_1(\omega)$ and $I_2(\omega)$ were measured by blocking one of the two arms. Note $I_{12}(\omega)$, $I_1(\omega)$, and $I_2(\omega)$ here are radiation at the detector, which was denoted with “ Q ” in Chapter 2. In the data processing, I identified peaks and valleys of the fringes, and calculated the fringe visibility/contrast, and then calculated $|g_{12}(\omega)|$ according to Eq. 2.4.14.

The power-dependent coherence evolution $|g_{12}(\omega, P)|$ and spectral evolution $I_1(\omega, P)$ and $I_2(\omega, P)$ were obtained by repeating the above steps with varying power coupled into the fiber. Note P is the average power of SC output. The short-arm spectrum evolution $I_1(\omega, P)$ is used to represent the SC spectrum, because it has less divergence and higher intensity than the long-arm one. The spectrally averaged coherence

$$\langle |g_{12}^{(1)}(P)| \rangle = \frac{\sum |g_{12}^{(1)}(\omega, P)| \cdot I_1(\omega)}{\sum I_1(\omega)} \quad (4.1.1)$$

was calculated to represent the overall coherence.

4.2 Simulation

4.2.1 Introduction

SC generation is modeled using the frequency-domain GNLSE with approximation (Eq. 2.2.64). It can be directly solved using ordinary differential equation (ODE) solvers. “ODE45” solver in MATLAB is used here. The solver automatically finds optimal step lengths to satisfy user-specified precisions. The code provided in [Dudley and Taylor, 2010] is used, with some adjustment. This code does not include noise. How to model noise and calculate coherence is introduced in Section 4.2.5.

The pump is sech^2 pulses with an optional linear chirp:

$$A(z = 0, t) = \sqrt{P_0} \text{sech} \left(\frac{t}{T_0} \right) \exp \left(-i \frac{C}{2} \frac{t^2}{T_0^2} \right) \quad (4.2.1),$$

in which P_0 is the peak power of the pulses, $T_0 = T_{FWHM}/1.763$, and C represents a linear chirp. The frequency-domain representation is

$$\tilde{A}(z = 0, \omega) = FT \{ A(z = 0, t) \} \quad (4.2.2).$$

This is the initial state of the GNLSE. Noise should be added when needed.

Specific dispersion and Raman terms in the GNLSE can either be found in literature or be calculated as follows.

4.2.2 The dispersion term

The theory about the dispersion term is introduced in Section 2.2.2.

The dispersion curve of the SF6 PCF used in my experiment cannot be found in literature. It is thus estimated based on the dispersion curves of some other SF6 PCFs in [Kumar et al., 2002], and later corrected by comparing simulated SC spectra to experimental ones. The dispersion curve of the tellurite PCF used in my experiment was reported in [Kumar et al., 2003; and Domachuk et al., 2008] (Fig. 4.2 (b)).

To convert GVD $\beta_2(\omega)$ to the dispersion term $B(\omega)$ in the GNLSE, two methods were introduced in Section 2.2.2. Method (1) is used here, which is to calculate the expansion coefficients β_k based on $\beta_2(\omega)$, and then calculate $B(\omega)$. In this way the result $B(\omega)$ can be extended to any interested bandwidth. Using method (2) yields results only for the bandwidth that the original GVD curve covers.

Specifically, GVD reported in those papers are in terms of $D(\lambda)$, which is another representation of GVD other than $\beta_2(\omega)$. The numerical data of $D(\lambda)$ were extracted from the figure in the paper using an unofficial Matlab application “grabit” [Doke, 2007].

Using $\omega = 2\pi c/\lambda$ and

$$D(\omega) = -\frac{2\pi c}{\lambda^2} \beta_2(\omega) \quad (2.2.37),$$

$D(\lambda)$ can be converted to $\beta_2(\omega)$. Then considering

$$\beta_2(\omega) = \beta_2(\omega_0) + (\omega - \omega_0)\beta_3(\omega_0) + \frac{1}{2!}(\omega - \omega_0)^2 \beta_4(\omega_0) + \dots \quad (2.2.39),$$

curve fitting is performed to obtain β_2 and β_3 , and also higher-order dispersion if necessary.

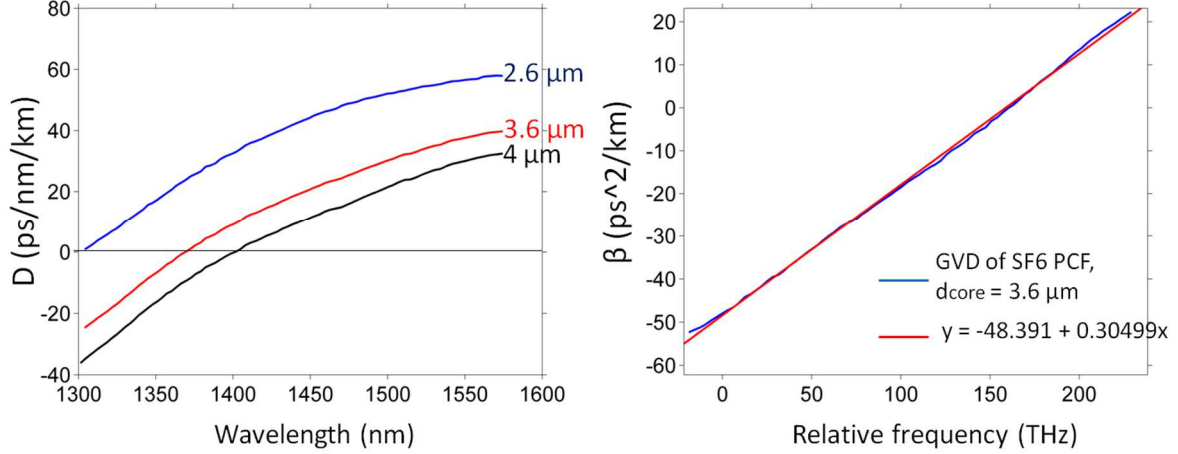


Fig. 4.5. Calculation of the dispersion of the SF6 PCF. (a) Calculating the dispersion curve of the 3.6- μm -core PCF based on the dispersion curves of a 2.6- μm and a 4- μm -core SF6 PCFs, through linear interpolation. The 2.6- μm and the 4- μm -core curves are excerpted from [Kumar et al., 2002]. (b) Linear curve fitting of $\beta_2(\omega-\omega_0)|_{3.6\text{-}\mu\text{m}}$.

Model	linear $y = p1*x + p2$	quadratic $y = p1*x^2 + p2*x + p3$
p1	0.305	0.0001266
p2	-48.39	0.2784
p3		-47.66
SSE	37.24	8.949
R-square	0.999	0.9998

Table 4.2. Polynomial fitting of the $\beta_2(\omega-\omega_0)$ curve for the 3.6- μm -core SF6 PCF.

Fig. 4.5 shows the process to calculate β_2 and β_3 of the SF6 PCF. Fig. 4.5 (a) shows the $D(\lambda)$ curve of the 2.6- μm -core and the 4- μm -core SF6 PCF reported in [Kumar et al., 2002], and $D(\lambda)$ curve of the 3.6- μm -core SF6 PCF calculated based on linear interpolation. Fig. 4.5 (b) shows the $\beta_2(\omega-\omega_0)$ curve converted from the $D(\lambda)$ curve. A linear curve fitting is chosen to reproduce the $\beta_2(\omega-\omega_0)$ curve, yielding $\beta_2 = -48.39$ ps²/km and $\beta_3 = 0.305$ ps³/km. The details of the curve fitting are in Table 4.2. Note the fibers of 2.6- μm -core and 4- μm -core in [Kumar et al., 2002] are SF6 PCFs of a different

micro pattern than the ones used in my experiment, so the validity of this calculated dispersion curve needs to be carefully tested by comparing simulations with experimental measurement. In fact, major modifications of the dispersion were made to match with experimental data (Section 5.1.2).

For the tellurite PCF, the $D(\lambda)$ curve (Fig. 4.2 (b)) was reported in [Domachuk et al., 2008]. Using the same method, the results of curve fitting were obtained as in Table 4.3. In this case, the quadratic fitting is chosen, yielding $\beta_2 = -92.19 \text{ ps}^2/\text{km}$, $\beta_3 = 0.6411 \text{ ps}^3/\text{km}$, and $\beta_4 = -0.59 \cdot 10^{-3} \text{ ps}^4/\text{km}$ ($\beta_4 = 2 \cdot p_1$). This fitting curve was later found to be inaccurate for wavelengths longer than about $2 \text{ }\mu\text{m}$. Major modifications were made to match with experimental data (see Section 5.2.2).

Model	Linear $y = p1 \cdot x + p2$	quadratic $y = p1 \cdot x^2 + p2 \cdot x + p3$	cube $y = p1 \cdot x^3 + p2 \cdot x^2 + p3 \cdot x + p4$
p1	0.4576	-0.000295	5.709e-07
p2	-75.07	0.6411	-0.0008276
p3		-92.19	0.767
p4			-97
SSE	1.136e+05	1.191e+04	547.8
R-square	0.9858	0.9985	0.9999

Table 4.3. Polynomial fitting of the $\beta_2(\omega - \omega_0)$ curve for the tellurite PCF.

4.2.3 The Raman term

The theory about calculating the Raman function was introduced in Section 2.2.3.

The Raman response function of SF6 has been reported [Heiman et al., 1979; Aber et al., 2000; Kalashnikov et al., 2007; and Moeser et al., 2007]. Here the model in [Kalashnikov

et al., 2007] is used, where the Raman response function is modeled as Eq. 2.2.61, with $\tau_1 = 5.5$ fs, $\tau_2 = 32$ fs, and $f_R = 0.13$ (Fig. 4.6).

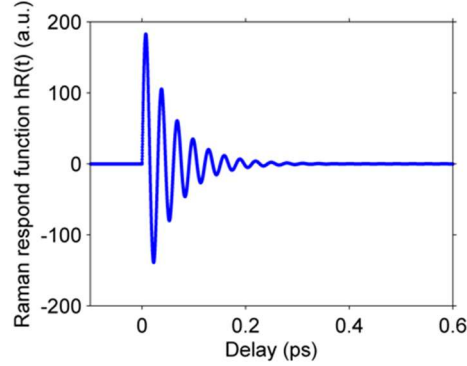


Fig. 4.6. Raman response function $h_R(t)$ of SF6. It is modeled as Eq. 2.2.61, with $\tau_1 = 5.5$ fs, $\tau_2 = 32$ fs, and $f_R = 0.13$.

The composition of my tellurite fiber is 75TeO₂–12ZnO–5PbO–3PbF₂–5Nb₂O₅. The Raman gain spectra of a few similar compositions have been reported. 77.1TeO₂–22.9ZnO was measured in [Plotnichenko et al., 2005], and the result is denoted here as Raman gain spectrum 1, g_{R1} . Stegeman et al. (2006) used TeO₂–TiO_{0.5}–PbO, and Qin et al. (2007) used TeO₂–Bi₂O₃–ZnO–Na₂O, showing similar results of Raman gain spectra (denoted here as Raman gain spectrum 2, g_{R2}). g_{R1} and g_{R2} have similar shapes, but different magnitudes. g_{R1} is $\sim 2.3\times$ higher than g_{R2} , according to the $\sim 735\text{-cm}^{-1}$ peak. As a result, g_{R1} yields an invalid $f_R = 1.37$. g_{R2} is used here, yielding $f_R = 0.55$ and $h_R(t)$ as in Fig.4.7 (b). A comparison of these two cases is in Table 4.4.

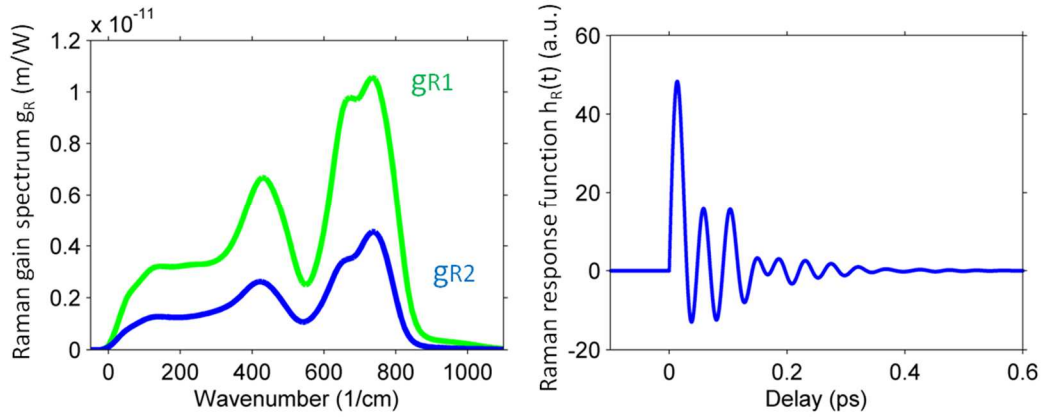


Fig. 4.7. (a) Raman gain spectra $g_R(\omega)$ of tellurite glasses. The green curve g_{R1} was reported in [Plotnichenko et al., 2005], and the blue curve g_{R2} was reported in [Stegeman et al., 2006; Qin et al., 2007; Yan et al., 2010]. Both are calibrated for pump wavelength $\lambda_0 = 514.5$ nm. (b) Raman response function $h_R(t)$ calculated based on g_{R2} , using Eq. 2.2.57.

	g_{R1}	g_{R2}
Reported	[Plotnichenko et al., 2005]	[Stegeman et al., 2006; Qin et al., 2007; Yan et al., 2010]
Composition	77.1TeO ₂ -22.9ZnO (material 1)	TeO ₂ -Bi ₂ O ₃ -ZnO-Na ₂ O [Qin] (material 2)
Pump λ_0 (nm)	514.5	632.8 (converted to 514.5 using $g_R \propto 1/\lambda_0$)
Major peak frequency (cm ⁻¹)	~430, ~660, ~735 (g_{R1} and g_{R2} have similar shapes)	
733-cm ⁻¹ peak value (10 ⁻¹³ m/W)	109 (= 57*peak value of g_R [SiO ₂])	38.5 (Converted to 47.2, which is 25*peak value of g_R [SiO ₂])
$h_R(t)$	Similar	
f_R	1.37	0.55

Table 4.4. Comparison of two Raman gain spectra: g_{R1} reported in [Plotnichenko et al., 2005] and g_{R2} reported in [Stegeman et al., 2006; Qin et al., 2007; Yan et al., 2010], and calculation of the Raman term.

4.2.4 Simulation parameters

The parameter values for simulation are listed in Table 4.5. Note they might need to be optimized in order to match simulations to experimental measurement (see Ch. 5).

Parameter	SF6 PCF	Tellurite PCF
Pump wavelength λ_0 (nm)	1550	
Pump pulse duration T_{FWHM} (fs)	110	
Pump chirp	0	
Pump power fluctuation (%)	2	
Fiber length L_{fiber} (mm)	105, 4.7, 3.9, 1	27
Loss (dB/m)	4	
Dispersion	$\beta_2 = -48.39 \text{ ps}^2/\text{km}$, $\beta_3 = 0.305 \text{ ps}^3/\text{km}$	$\beta_2 = -92.19 \text{ ps}^2/\text{km}$, $\beta_3 = 0.6411 \text{ ps}^3/\text{km}$, $\beta_4 = -0.59 \cdot 10^{-3} \text{ ps}^4/\text{km}$
Nonlinearity γ (/km·W)	87.6	596
Raman fraction f_R	0.13	0.55
Raman response function $h_R(t)$	$\tau_1 = 5.5 \text{ fs}$, $\tau_2 = 32 \text{ fs}$ (Eq. 2.2.61)	Numerical curve as in Fig.4.7 (b)

Table 4.5. Values of parameters for simulation (subject to change in the optimization process).

The nonlinearity γ can be calculated based on the assumption that the effective mode area is just the area of the fiber core:

$$\gamma = \frac{\omega_0 n_2}{c A_{eff}} = \frac{2\pi}{\lambda_0} \frac{n_2}{\pi d_{core}^2 / 4} = \frac{8n_2}{\lambda_0 d_{core}^2} \quad (4.2.3).$$

For our SF6 PCF, $\gamma = (8 \cdot 22 \cdot 10^{-20} \text{ m}^2/\text{W}) / (1.55 \cdot 10^{-6} \text{ m} \cdot (3.6 \cdot 10^{-6} \text{ m})^2) = 0.0876 \text{ /m} \cdot \text{W}$
 $= 87.6 \text{ /km} \cdot \text{W}$.

For our tellurite PCF, $d_{core} = 2.5 \text{ } \mu\text{m}$ was reported [Domachuk et al, 2008], so core area should be $\pi \cdot d_{core}^2 / 4 = 4.9 \text{ } \mu\text{m}^2$. But an effective mode area of $1.7 \text{ } \mu\text{m}^2$ was reported

[Domachuk et al, 2008]. Using this value, $\gamma = (2\pi \cdot 25 \cdot 10^{-20} \text{ m}^2/\text{W}) / (1.55 \cdot 10^{-6} \text{ m} \cdot 1.7 \cdot 10^{-12} \text{ m}^2) = 0.596 / \text{m} \cdot \text{W} = 596 / \text{km} \cdot \text{W}$.

4.2.5 Modeling noise and coherence

In the experiment, spectral interference fringes were measured, and then coherence was calculated using

$$V(\omega) = \frac{(I_{\max} - I_{\min})}{(I_{\max} + I_{\min})} = \frac{2[I_1(\omega)I_2(\omega)]^{1/2}}{I_1(\omega) + I_2(\omega)} |g_{12}(\omega)| \quad (2.4.14).$$

In the simulations, coherence was calculated directly using its definition:

$$g_{12}(\omega) = \frac{\langle \tilde{E}_1^*(\omega) \tilde{E}_2(\omega) \rangle}{\sqrt{I_1(\omega)I_2(\omega)}} \quad (2.4.12).$$

Considering

$$\tilde{E}(\vec{r}, \omega - \omega_0) = F(x, y, \omega - \omega_0) \tilde{A}(z, \omega - \omega_0) \exp(i\beta_0 z) \quad (2.2.3),$$

the modal distribution F can be ignored, and there is

$$|g_{12}(\omega)| = \left| \frac{\langle \tilde{A}_1^*(\omega) \tilde{A}_2(\omega) \rangle}{\sqrt{I_1(\omega)I_2(\omega)}} \right| \quad (4.2.4).$$

Simulations using the GNLSE were repeated for N (here 20) times with independent noise to generate SC fields $\tilde{A}_m(\omega)$, $m = 1, 2, \dots, N$. The noise includes: (a) quantum-limit shot noise in the pump, and (b) pulse-to-pulse fluctuation of the pump power.

Spontaneous Raman noise was not included here, because it has been found to cause coherence degradation two orders of magnitude smaller than shot noise does [Corwin et al., 2003; Dudley et al., 2006].

Specifically, the shot noise is one photon of a random phase in each frequency grid:

$$\tilde{A}_{noise}(\omega) = |A_{noise}(\omega)| \exp\{i\phi_R\} \quad (4.2.5).$$

The random phase ϕ_R obeys a uniform distribution between 0 and 2π :

$$\phi_R \in U(0, 2\pi) \quad (4.2.6),$$

where $U(a, b)$ is the uniform distribution between a and b .

Considering the energy of the photon

$$E = \hbar\omega = |A_{noise}(\omega)|^2 df \quad (4.2.7),$$

there is

$$|A_{noise}(\omega)| = \sqrt{\hbar\omega/df} \quad (4.2.8),$$

in which the frequency $f = \omega/2\pi$, and df is the increment of the frequency grid.

The pulse-to-pulse fluctuation of the pump power obeys a normal distribution with a certain standard deviation $x\%$ (e.g., $x = 2$). The peak power of a pulse is

$$P_0 = \bar{P}_0 \cdot \Delta_p \quad (4.2.9),$$

in which

$$\Delta_p \in N(\mu=1, \sigma=x\%) \quad (4.2.10).$$

$N(\mu, \sigma)$ is the normal distribution with a mean μ and a standard deviation σ .

\bar{P}_0 is the average peak power of pump pulses:

$$\bar{P}_0 = \frac{0.88P}{f_{rep} T_{FWHM}} \quad (4.2.11),$$

in which P is the average power of the laser, f_{rep} is the repetition rate, and T_{FWHM} is the duration of the pulse.

Eq. 4.2.4 was calculated as follows. The ensemble average $\langle \rangle$ is the average of all non-identical pairs: $m \neq n$, $m, n = 1, 2, \dots, N$. Writing the explicit form of $\langle \rangle$ in Eq. 4.2.4 yields

$$\begin{aligned} |g_{12}(\omega)| &= \frac{\left| \langle \tilde{A}_m^*(\omega) \tilde{A}_n(\omega) \rangle_{m \neq n} \right|}{\left[\langle |\tilde{A}_m(\omega)|^2 \rangle_m \langle |\tilde{A}_n(\omega)|^2 \rangle_n \right]^{1/2}} \\ &= \frac{\left| \sum_{m \neq n} \tilde{A}_m^*(\omega) \tilde{A}_n(\omega) / [N(N-1)] \right|}{\sum_m |\tilde{A}_m(\omega)|^2 / N} \end{aligned} \quad (4.2.12).$$

In the denominator,

$$I_1(\omega) = I_2(\omega) = \sum_m |\tilde{A}_m(\omega)|^2 / N \quad (4.2.13),$$

because m and n are from the same pool: $m, n = 1, 2, \dots, N$. $I_1(\omega)$ and $I_2(\omega)$ are average spectra of the short/long arm, respectively.

Eq. 4.2.12 and 4.2.13 are consistent with the practical experiment, where the photo detectors are slow. There is usually different attenuation in two arms of the interferometer. This intensity imbalance was factored out in the data processing (Eq. 2.4.14), so it does not need to be included here.

Suppose a fast detector is used and it can distinguish each pulse, and the single-shot coherence is

$$\begin{aligned} g_{12}(\omega)_{\text{single-shot}} &= \frac{\tilde{A}_1^*(\omega)\tilde{A}_2(\omega)}{[I_1(\omega)I_2(\omega)]^{1/2}} = \frac{\tilde{A}_m^*(\omega)\tilde{A}_n(\omega)}{[|\tilde{A}_m(\omega)|^2|\tilde{A}_n(\omega)|^2]^{1/2}} = \frac{\tilde{A}_m^*(\omega)\tilde{A}_n(\omega)}{|\tilde{A}_m(\omega)||\tilde{A}_n(\omega)|} \\ &= \exp\left\{-i\left[\arg(\tilde{A}_m(\omega)) - \arg(\tilde{A}_n(\omega))\right]\right\} \end{aligned} \quad (4.2.14),$$

in which $\arg(\)$ means the argument of a complex number: $\arg[\exp(i\phi)] = \phi$, $0 \leq \phi < 2\pi$.

In this case the averaged coherence (Eq. 4.2.4) becomes something that involves only the phase:

$$\begin{aligned} |g_{12_PHASE}(\omega)| &= \left| \left\langle g_{12}(\omega)_{\text{single-shot}} \right\rangle_{m \neq n} \right| \\ &= \frac{\left| \sum_{m \neq n} g_{12}(\omega)_{\text{single-shot}} \right|}{N(N-1)} \end{aligned}$$

$$= \frac{\left| \sum_{m \neq n} \exp \left\{ -i \left[\arg \left(\tilde{A}_m(\omega) \right) - \arg \left(\tilde{A}_n(\omega) \right) \right] \right\} \right|}{N(N-1)} \quad (4.2.15).$$

Its physical meaning is, as mentioned above, a fast detector is used and it can distinguish each pulse. As a result, the coherence involves only the phase, and not the intensity.

Eq. 4.2.12 is the practical experimental case where the intensity fluctuation in the spectrum and the phase correlation both contribute to the coherence. Eq. 4.2.15 involves only the phase. Some coherence degradation has been thought to be related to the intensity fluctuation of the SC spectrum, so these two definitions are used here to isolate the effects of the intensity fluctuation and the phase instability.

The pulse-to-pulse stability of spectral intensity is:

$$-C_v(\omega) = -\sigma_I / \langle I_m(\omega) \rangle = -\sqrt{\langle (I(\omega)_m - \langle I_m(\omega) \rangle)^2 \rangle} / \langle I_m(\omega) \rangle \quad (4.2.16),$$

in which C_v is the coefficient of variation, σ_I is the standard deviation of spectral intensity, $\langle \rangle$ is the mean with respect to all pulses, and $I_m(\omega) = |\tilde{A}_m(\omega)|^2$. The negative sign is used such that higher values of $-C_v$ correspond to higher stability. The maximum value of $-C_v$ is 0, meaning no pulse-to-pulse fluctuation in spectral intensity. Evolution $-C_v(\lambda, P)$ and spectrally-averaged curve $-C_v(P)$ were obtained similarly as coherence evolution and averaged coherence.

5. RESULTS AND DISCUSSIONS

SUMMARY

This chapter presents experimental and simulated results followed by analysis and discussions about the physics of supercontinuum (SC) and its coherence.

5.1 is about SC generated from different lengths of SF6 PCFs. In 5.1.1, measured spectral and coherence evolution is presented. In 5.1.2 and 5.1.3, simulation results are presented. Optimization of the simulations to match experimental measurements is demonstrated, and the physical meaning of the results is discussed. 5.1.4 concludes this section.

5.2 is about the results using the tellurite PCF. It is organized similarly as 5.1.

5.1 Results Using SF6 PCFs

5.1.1 Experimental results

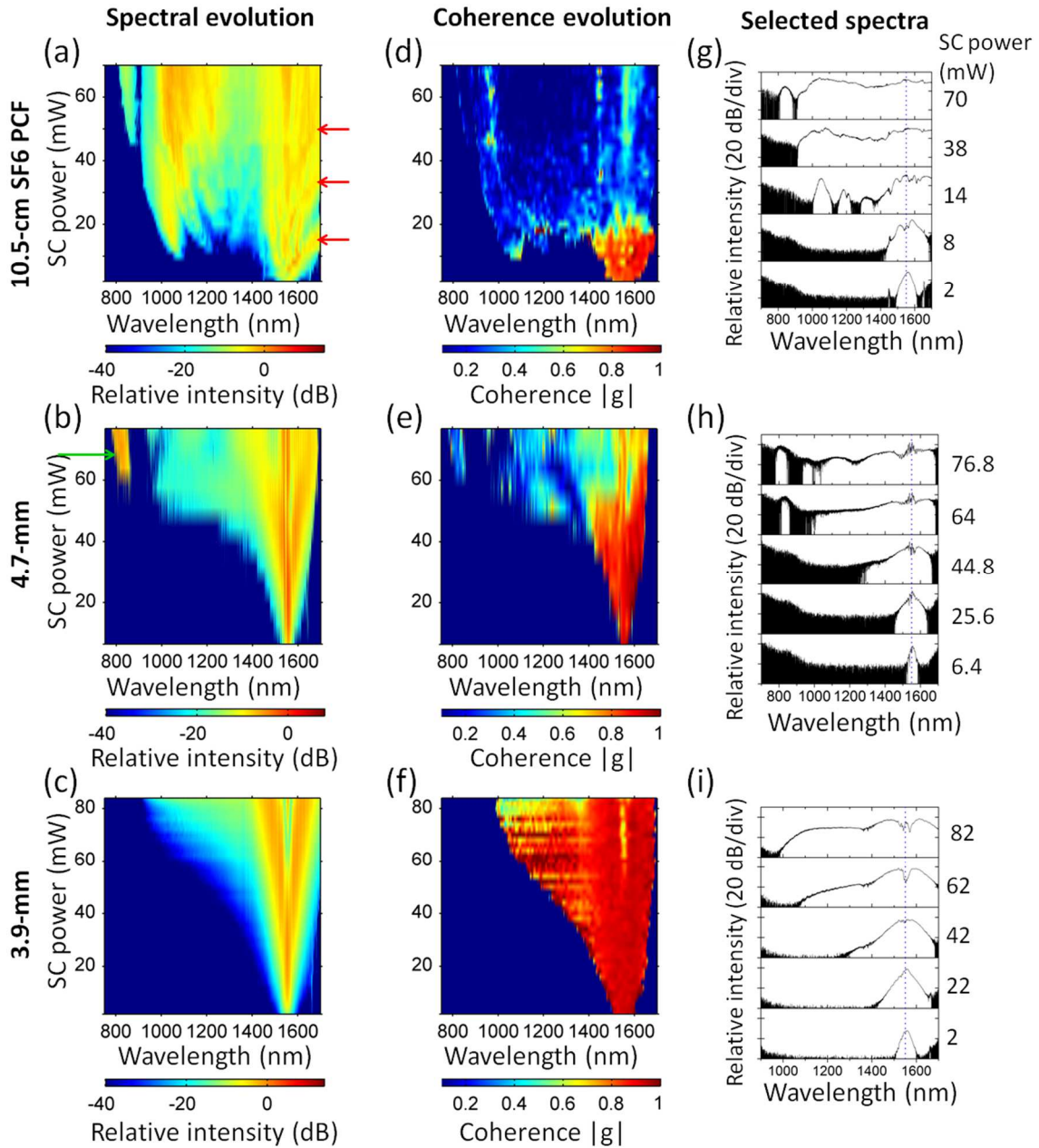


Fig. 5.1. Spectral evolution (a)–(c) and coherence evolution (d)–(f) of SC generated in three different lengths of SF6 PCFs (10.5-cm, 4.7-mm, and 3.9-mm). The red arrows in (a) mark soliton trajectories. The green arrow in (b) marks the Cherenkov peak. The spectral evolution is calibrated such that the maximum intensity is 0 dB. The lower limit of the color bar is set to -40 dB so that the 40-dB bandwidth is visualized in the

evolution; the upper limit is set for optimal visualization of features. (g)–(i) are line plots of representative spectra.

Fig. 5.1 shows measured spectral and coherence evolution of SC generated in different lengths (10.5-cm, 4.7-mm, and 3.9-mm) of SF6 PCFs, plotted in contour maps. The y axes of the contour maps are the average power of SC. Line plots of representative spectra are also shown (Fig. 5.1 (g)–(i)).

In the 10.5-cm-fiber case, the spectral evolution (Fig. 5.1 (a)) shows a soliton-fission-dominated pattern. Three solitons are marked with red arrows. Ejection of the first soliton occurs at ~ 10 mW, accompanied with the emergence of the Cherenkov peak at ~ 1070 nm. Solitons show Raman-induced red shift when the power increases. The coherence (Fig. 5.1 (d)) is high for only the initial stage of broadening, and degrades quickly after soliton fission.

The SC from the 4.7-mm fiber (Fig. 5.1 (b)) has two symmetric spectral lobes at both sides of the pump wavelength for power less than ~ 45 mW, indicating a SPM-dominated regime. At ~ 45 mW, strong spectral broadening occurs, indicating strong temporal compression, and soliton fission is about to happen. Although no soliton trajectory was captured due to the limited wavelength range of measurements, the Cherenkov peak (marked with a green arrow) emerging at ~ 850 nm ~ 60 mW is the evidence of a corresponding soliton. The coherence properties (Fig. 5.1 (e)) show association with soliton fission. High coherence (~ 0.9) was maintained for power less than ~ 45 mW (before soliton fission). For power higher than ~ 45 mW (after soliton fission), coherence degradation occurs at most parts of the spectrum.

For the 3.9-mm case, the story is less apparent by looking at Fig. 5.1 (c) and (f) alone. Fig. 5.1 (c) and (f) (0–84 mW) can be associated to the 0–~50 mW part of Fig. 5.1 (b) and (e), respectively. In Fig. 5.1 (c), the SC reaches ~1000 nm at the power ~75 mW, similar to the situation when the power is ~50 mW in the 4.7-mm case (Fig. 5.1 (b)). This indicates strong temporal compression, and soliton fission is just going to happen. At the same time, coherence degradation starts to occur at wavelengths far from the pump (at P ~75 mW in Fig. 5.1 (f)). If increasing the power above 84 mW, the consequent dynamics should be similar to what happen at powers greater than ~50 mW in the 4.7-mm case. Unfortunately, these dynamics were not measured, due to the limited power of the pump. The fluctuation of coherence at wavelengths below 1400 nm (Fig. 5.1 (f)) will be discussed later (Section 5.1.3).

SC in the 1.0-mm SF6 PCF shows a pure SPM pattern. It reaches a 40-dB bandwidth of about 250 nm at the maximum power. Since we are mostly interested in broad SC, discussion about this SC will be in a separate paper.

The above results show association between coherence degradation and soliton fission. Using a fiber slightly shorter than the soliton fission length, SC of almost perfect coherence can be generated with little sacrifice in bandwidth.

5.1.2 Simulated spectral evolution and discussions

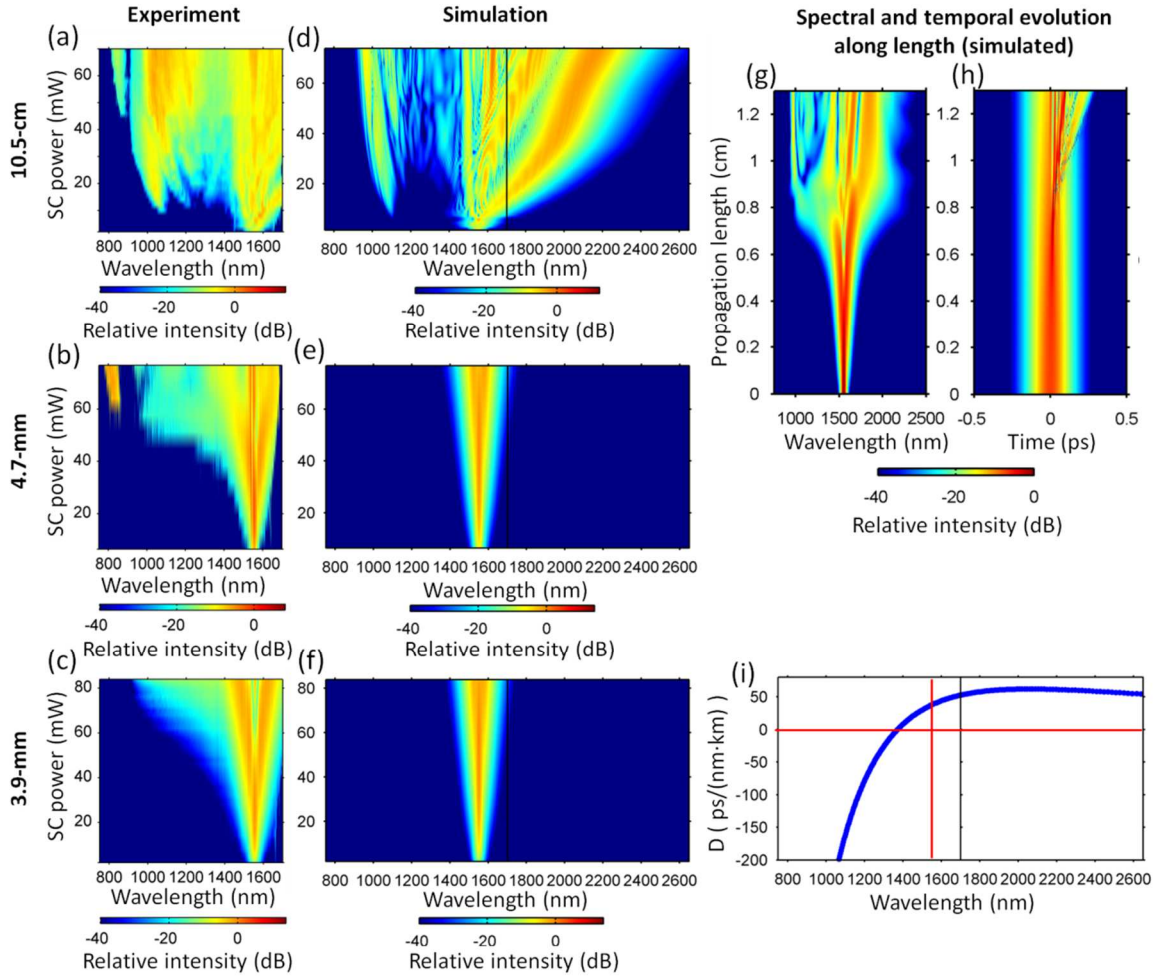


Fig. 5.2. (a)–(c) Experimentally measured spectral evolution using three different lengths of SF6 PCF, respectively. (d)–(f) Corresponding simulation results. The vertical black line at 1700 nm helps visually comparing with the experimental data. (g) and (h): Simulated spectral and temporal evolution depending on the propagation length. $P = 77$ mW is used. It is shown graphically that soliton fission happens at ~ 9 mm. Analytically calculated soliton fission length is similar $L_{fiss} = 10.2$ mm. (i) GVD $D(\lambda)$ of the fiber. The red lines mark the zero dispersion wavelength (ZDW) and the pump wavelength (1550 nm). The ZDW is ~ 1370 nm. The GVD at the pump wavelength is ~ 38 ps/(nm·km).

Simulated spectral evolution is plotted in Fig. 5.2, in comparison with the experimental results. For the short fibers (4.7 and 3.9 mm), the simulations show much “slower” evolution, which can be quantified by the soliton fission length L_{fiss} or the power at which

soliton fission happens. Specifically, the simulations (Fig. 5.2 (g) and (h)) graphically show soliton fission at ~ 9 mm, when $P = 77$ mW (same as the maximum power in the 4.7-mm-fiber case of the experiment). P is the average power of SC. Analytically calculated soliton fission length is close: $L_{fiss} = 10.2$ mm (using Eq. 2.3.17), when $P = 77$ mW. In the measurements, soliton fission happens between 3.9 and 4.7 mm, when $P = 77$ mW.

To fix this mismatch in the soliton fission length, the simulated L_{fiss} needs to be shortened by about a half. Considering $L_{fiss} = \sqrt{T_0^2 / |\beta_2| \gamma P_0}$ (Eq. 2.3.17), in which the duration of the pump pulses $T_0 = T_{FWHM} / 1.763$, $|\beta_2| = |\beta_2(\omega_0)|$, and the peak power of the pump pulse $P_0 = 0.88 \cdot P / (f_{rep} \cdot T_{FWHM})$, there is

$$L_{fiss} = 0.6 \sqrt{T_{FWHM}^3 f_{rep} / |\beta_2| \gamma P} \quad (5.1.1).$$

Tuning down T_{FWHM} and tuning up P , γ , and $|\beta_2|$ in the simulations can help fixing the mismatch in L_{fiss} . Tuning the chirp of the pump C is also considered, because it affects the beginning stage of the evolution and the soliton fission length too.

The simulations can be optimized by iteratively tuning parameters and manually comparing features with experiments. The parameters can be tuned in 3 steps: (1) duration of pump pulses T_{FWHM} , (2) the average power of SC P , the nonlinearity of the fiber γ , and GVD of the fiber $|\beta_2|$, (3) the chirp of the pump C . Tuning in this order allows for easier comparison of features.

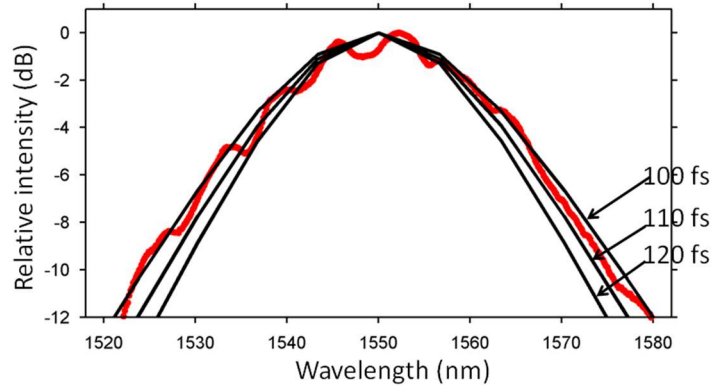


Fig. 5.3. Optimization of the duration of the pump pulse T_{FWHM} . Red curve: measured output spectrum at $P = 2$ mW and $L_{fiber} = 3.9$ mm. Black curves: simulated output spectrum using a pump of transform-limited sech^2 pulses of $T_{FWHM} = 100, 110,$ and 120 fs, respectively, also at $P = 2$ mW and $L_{fiber} = 3.9$ mm.

The duration of the pump pulse T_{FWHM} was optimized by inspecting the output bandwidth. T_{FWHM} determines the pump bandwidth, which in turn affects the output bandwidth. It is ideal to inspect cases of low SC powers and short fibers, because there is little broadening, other parameters are less involved, and thus the output bandwidth is highly dependent on T_{FWHM} in these cases. Here the case of $P = 2$ mW and $L_{fiber} = 3.9$ mm is investigated, and the measured output spectrum is between the simulated output spectra using transform-limited sech^2 pulses of $T_{FWHM} = 110$ fs and 100 fs as the pump (Fig. 5.3). So T_{FWHM} was modified from 110 to 105 fs. In fact the simulations show no appreciable broadening from the pump to the output. Although it is more straightforward to experimentally measure the pump duration and the chirp, our goal is to determine as many parameters as possible and avoid experimentally measuring them.

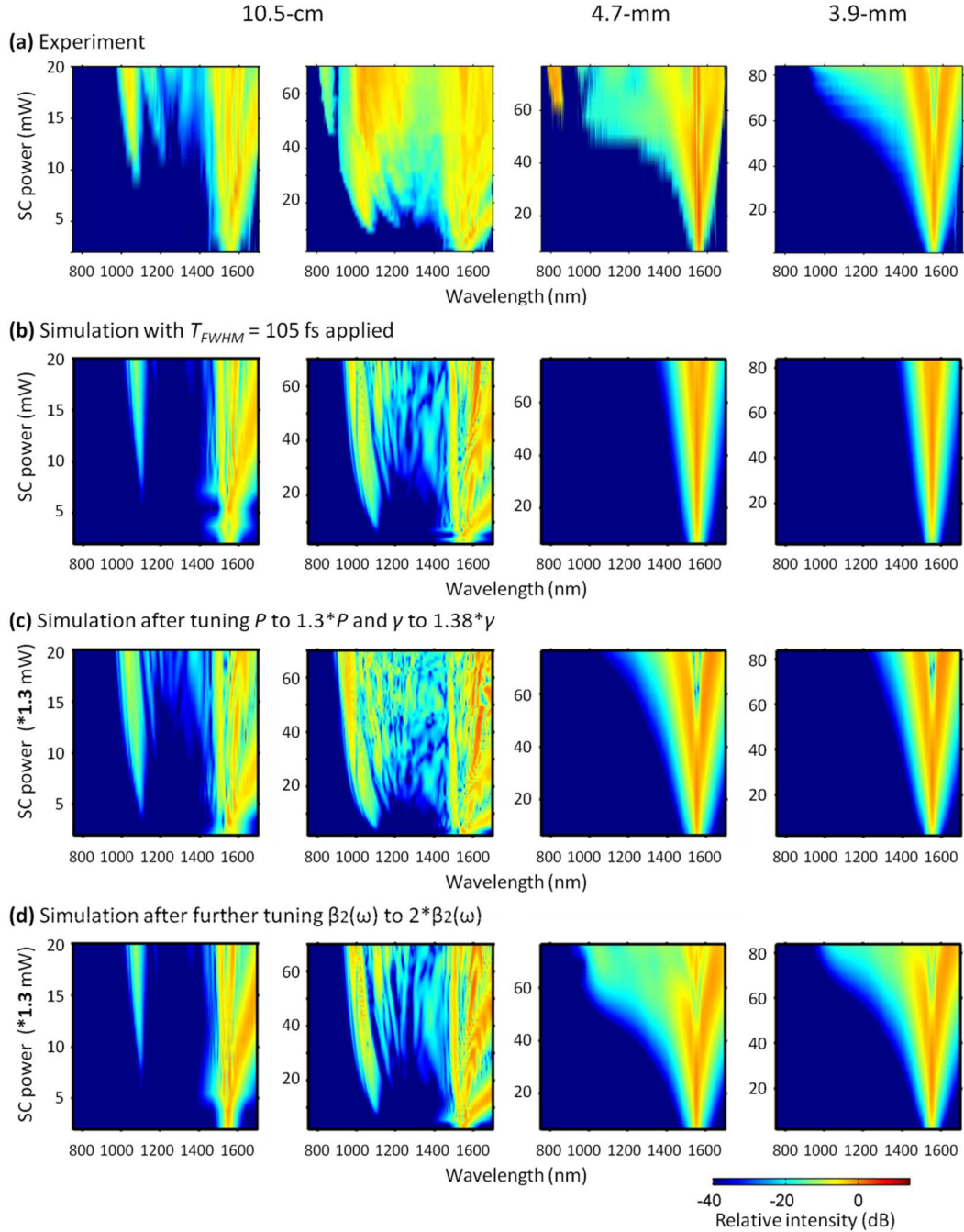


Fig. 5.4. Optimization of the simulated spectral evolution. Each line includes four plots of spectral evolution: the beginning (low power) part of the 10.5-cm-fiber case, the 10.5-cm-fiber case, the 4.7-mm-fiber case, and the 3.9-mm-fiber case. (a) Experimental data. (b) Simulations with $T_{FWHM} = 105$ fs has been applied. (c) Simulations after further tuning P to $1.3 \cdot P$ and γ to $1.38 \cdot \gamma$. (d) Simulations after further tuning $\beta_2(\omega)$ to $2 \cdot \beta_2(\omega)$.

The product of $P \cdot \gamma$ can be considered as one parameter to tune. For any pair of positive coefficients a and b of a fixed product ($a \cdot b = \text{constant}$), tuning P to $a \cdot P$ and γ to $b \cdot \gamma$ yields

invariant SC spectrum, up to a calibration constant. This can be seen in the GNLSE (Eq. 2.2.30 and 31) by considering $P \propto |A|^2$. Tuning up $P \cdot \gamma$ enhances SPM, and causes soliton fission to happen earlier. One major feature of the SPM-based broadening is the spectral lobes at both sides of the pump wavelength (e.g., see the changes from Fig. 5.4 (b) to (c), 4.7- and 3.9-mm-fiber cases).

Tuning $|\beta_2|$ ($=|\beta_2(\omega_0)|$) was implemented by multiplying the whole curve of $\beta_2(\omega)$ by a constant. For example, tuning $\beta_2(\omega)$ to $a \cdot \beta_2(\omega)$ was applied when tuning $|\beta_2|$ to $a \cdot |\beta_2|$ is needed; a is a real coefficient. The reason is that tuning $|\beta_2|$ alone will change the shape of the $\beta_2(\omega)$ curve. For example, the ZDW will be changed. Multiplying $\beta_2(\omega)$ by a constant avoids this issue. Simulations show tuning up $|\beta_2|$ has a small impact on the two spectral lobes at both sides of the pump wavelength, but causes soliton fission to happen earlier (see e.g., the changes from Fig. 5.4 (c) to (d), 4.7- and 3.9-mm-fiber cases).

The above dynamics of tuning $P \cdot \gamma$ and $|\beta_2|$ can be understood physically as follows. SPM is based on the nonlinear refractive index $n = n_0 + n_2 I$. Considering $I \propto P$ and $n_2 \propto \gamma$, tuning up P or γ similarly enhances SPM. On the other hand, soliton fission happens when the pulse evolves to the shortest duration, and this timing depends on both SPM and dispersion. As a result, the soliton fission length depends on P , γ , and $|\beta_2|$.

Tuning $P \cdot \gamma$ to $\sim 1.8 \cdot P \cdot \gamma$ optimizes the SPM-based broadening (Fig. 5.4 (c) to (d)). Assuming tuning P to $1.3 \cdot P$, which indicates a 23% collimation loss in the experiment, γ should be tuned to $1.8/1.3 \cdot \gamma = 1.38 \cdot \gamma = 120.9/\text{km} \cdot \text{W}$. Further tuning $\beta_2(\omega)$ to $\sim 2 \cdot \beta_2(\omega)$ yields similar soliton fission lengths as in the experiment (Fig. 5.4 (c) to (d)).

The effect of adding a linear chirp C in the pump is illustrated in Fig. 5.5, using the 4.7-mm-fiber case. SPM induces positive chirps at the central parts of the spectrum. A positive initial chirp ($C > 0$) adds up with the SPM-induced chirp, and enhances spectral broadening. As a result, soliton fission happens earlier. In this case, there is a feature in the spectral evolution: the flattened central part of the spectrum. A negative initial chirp ($C < 0$) has opposite effects, causing soliton fission to happen later. The spectral features are enhanced oscillation structures, and narrowing or lack of broadening at the beginning of the spectral evolution. Fig. 5.5 shows the change in the soliton fission power (represented by the power where the Cherenkov radiation occurs) and in the features, depending on the initial chirp.

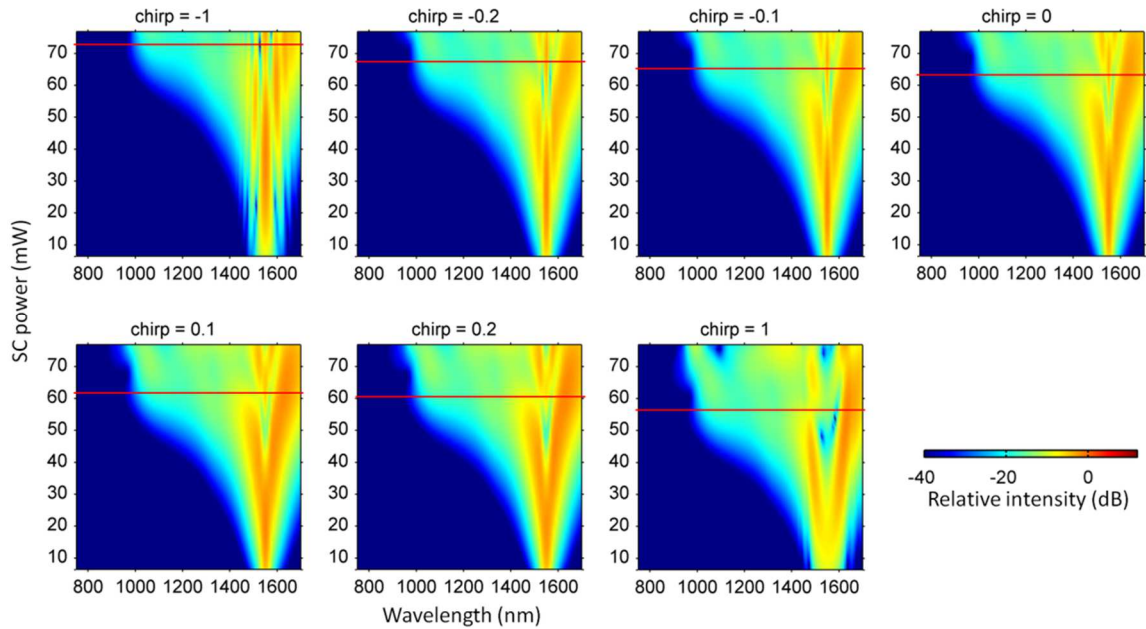


Fig. 5.5. Simulated spectral evolution with varying initial chirps, in the case of the 4.7-mm SF6 PCF. Adding positive or negative initial chirps causes features in the spectra, and changes the power at which soliton fission happens. Emergence of the Cherenkov peak is marked with red lines to represent the powers at which soliton fission happens.

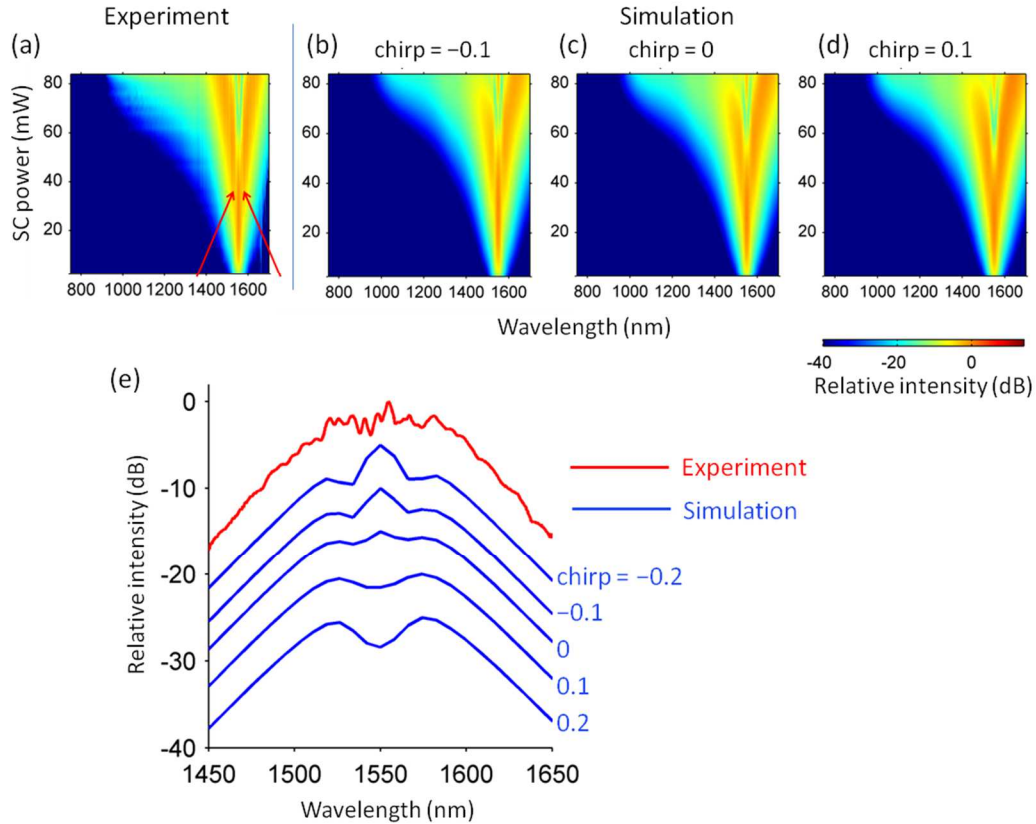


Fig. 5.6. Comparison between (a) the measured spectral evolution and (b)–(d) corresponding simulations using varying initial chirps, for the case of the 3.9-mm SF6 fiber. (a) shows gaps (marked with arrows) between the central peak and the spectral lobes. (b) and (c) also have these gaps, while in (d) a positive chirp ($C = 0.1$) flattens the central parts of the spectrum and causes the gaps to disappear. Spectra at $P = 40$ mW are stacked in (e) to show the features clearly.

It is possible to determine the initial chirp C based on the soliton fission power (Fig. 5.5 vs. Fig. 5.2 (b)). It was found that the features mentioned above are more subtle indicators. The case of the 3.9-mm fiber was investigated for this step, since the measured data using the 4.7-mm fiber is not ideal in resolution. In the measurements of the 3.9-mm-fiber case, there are gaps (marked with arrows in Fig. 5.6 (a)) between the central peak and the spectral lobes at both sides. Simulations with $C = -0.1$ and 0 have these gaps, while adding $C = 0.1$ flattens the central parts of the spectrum and causes the gaps to disappear. Spectra at $P = 40$ mW are stacked up in Fig. 5.6 (e) to better show

these features. Based on this, it can be decided that the pump has $C < 0.1$ in the experiment.

The lower limit of the chirp C can be determined by investigating the broadening at the beginning (low SC power) part of the evolution. As in Fig. 5.7, the experiments do not show the lack of broadening as in the simulated case of $C = -0.1$. So the pump has $C > -0.1$ in the experiment.

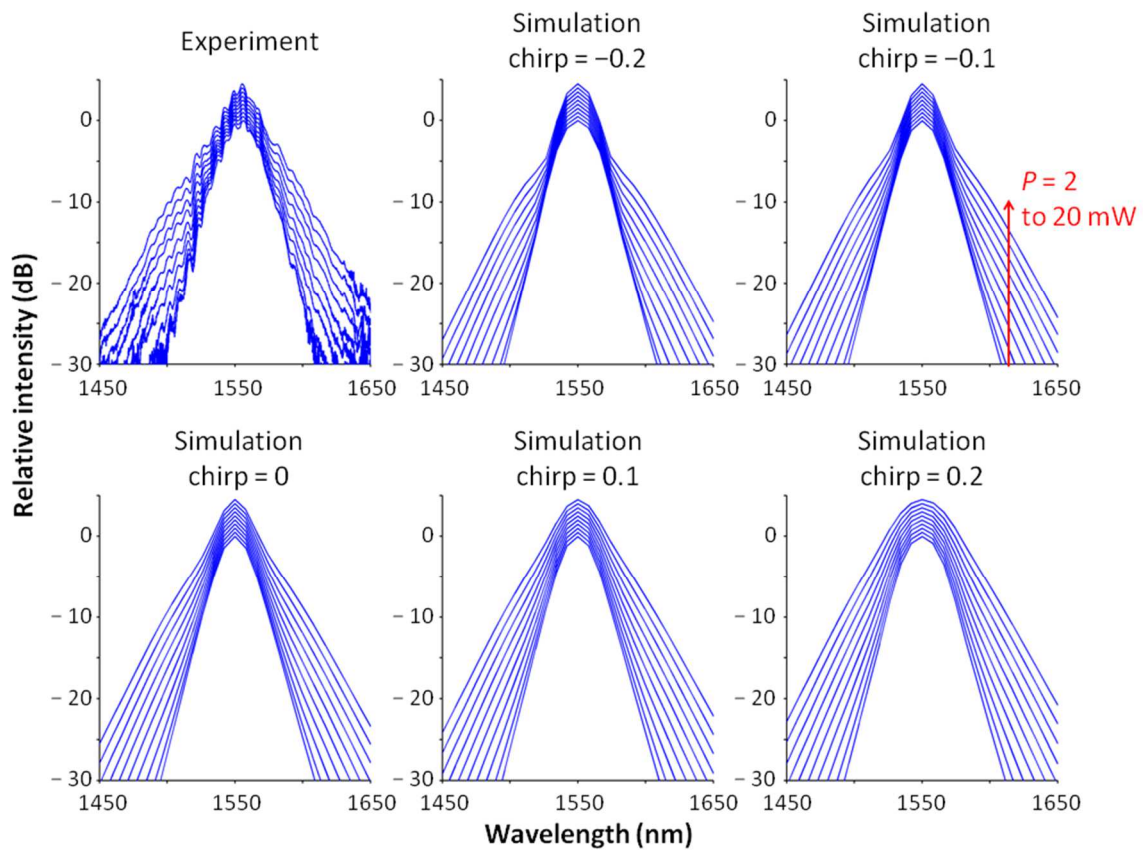


Fig. 5.7. Comparison of the broadening trends at the beginning (low SC power) part of the spectral evolution. The case of 3.9-mm SF6 PCF is used. Output spectra at $P = 2, 4, 6, 8, 10, 12, 14, 16, 18,$ and 20 mW are stacked in each plot. The simulations with initial chirp = -0.2 and -0.1 show narrowing or lack of broadening. This is not seen in the experiments. So the chirp in the experiment was > -0.1 .

By now it has been shown that the pump has a small or no chirp ($-0.1 < C < 0.1$) in the experiment. $C = 0$ was chosen as the optimal. The uncertainty in the chirp yields a small uncertainty in the soliton fission length or power. The examples in Fig. 5.5 show a change of about 5% in the soliton fission power when tuning C from -0.1 to 0.1 .

The above steps (1)–(3) of parameter tuning should be repeated to approach optimal match. In the above case, repeating step (1) still shows T_{FWHM} should be 105 fs. Repeating (2) and (3) still yields the same results.

So Fig. 5.4 (d) shows the optimized simulations. Comparisons with the measurements (compare Fig. 5.4 (d) with (a)) show agreement in the broadening extents, in the soliton fission powers, and in the emergence of Cherenkov radiation. The analytically calculated L_{fiss} is now ~ 5.4 mm when $P = 77$ mW, matching the experimental results where L_{fiss} should be between 3.9 and 4.7 mm.

There are some mismatches in the wavelengths of solitons (in the 10.5-cm case) and of the Cherenkov radiation (in the 10.5-cm and the 4.7-mm cases). The soliton wavelength is determined by the Raman-induced frequency shift $\Omega \propto |\beta_2|z/T_0^4$, in which T_0 is the duration of the soliton. In the 10.5-cm case, the experiments and the simulations show agreement in the trajectory of the first soliton, but some discrepancies in the trajectories of the second and the third ones. Tuning the dispersion curve should affect all solitons at the same time, and thus may not be the cure for these discrepancies. Inaccuracy in the soliton duration could be responsible for the mismatches, especially considering the inverse quartic dependence. Cherenkov radiation is phase matched with solitons, so

inaccuracy in the soliton wavelengths and in the dispersion should be both responsible for the mismatches in the wavelengths of the Cherenkov radiation.

The above process demonstrates in principle that, given a spectral evolution, the fiber length, and the average power of SC, all other parameters can be determined unambiguously, and the spectral evolution can be reproduced in simulations. Most importantly, the soliton fission length or power was reproduced quantitatively. Such optimization allows parameters to be estimated, and avoids experimentally measuring them.

In future research, a cost function should be developed to quantify the match of features. Then iterative optimization can be easily implemented by computer. More sophisticated tuning of parameters, for example tuning the shape of the dispersion curve, can be added for more subtle optimization.

5.1.3 Simulated coherence and discussions

After the above optimization, the pulse-to-pulse fluctuation of the pump power Δ_P is the only parameter to tune in order to match the simulated and the measured coherence. Tuning Δ_P could not match the coherence in the three fiber lengths at the same time. 5% fluctuation was chosen for optimal match in the 3.9-mm-fiber case. Simulated coherence is plotted in Fig. 5.8, in comparison with the experimental results. Fig. 5.8 (a)–(d) are power-dependent evolution, and (e) and (f) are spectrally-averaged coherence depending on the power.

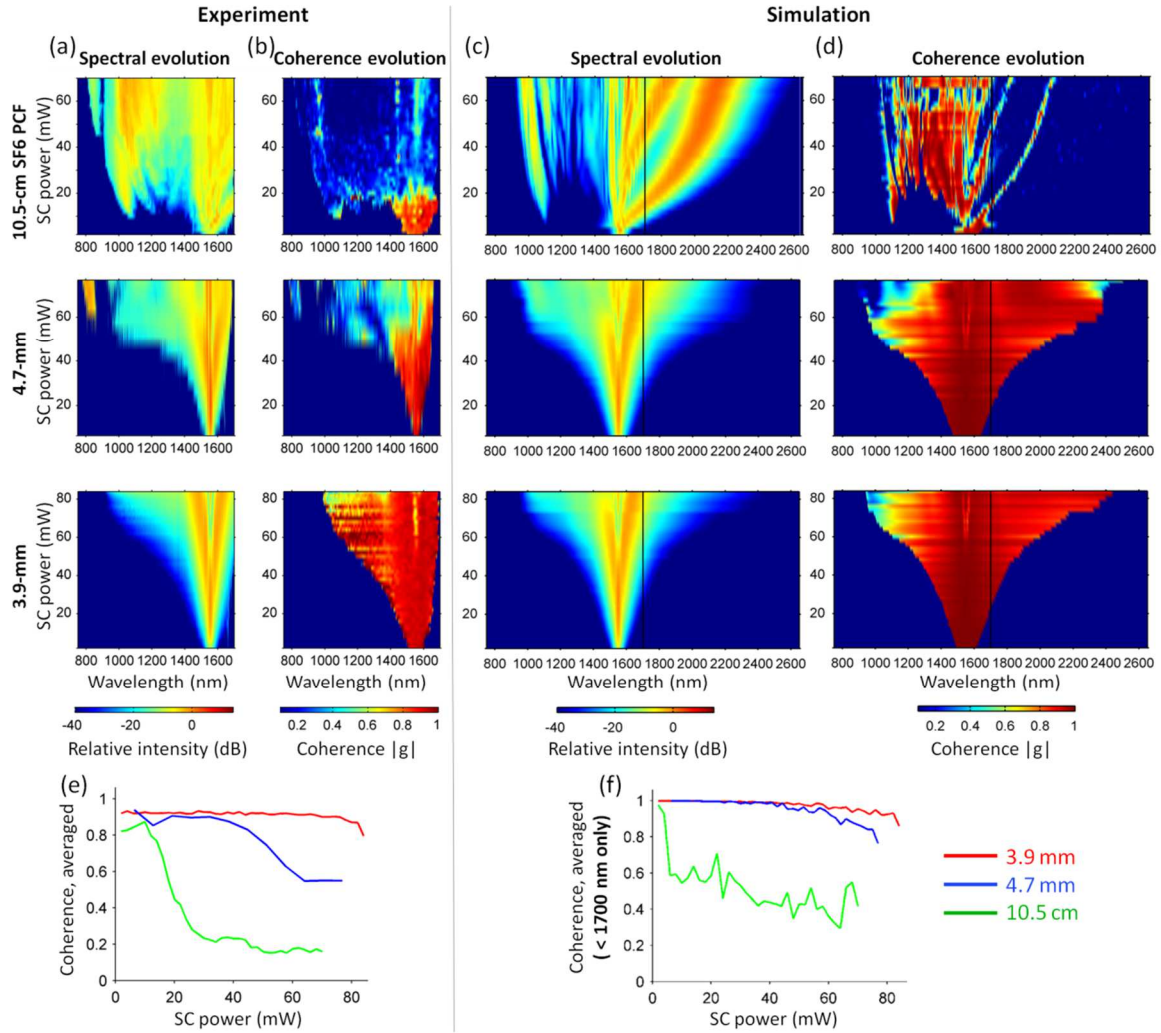


Fig. 5.8. Simulated coherence of SC generated in three different lengths of SF6 PCFs, in comparison with the experimental results. Column (a): three plots of measured spectral evolution using different fiber lengths. Column (b): measured coherence evolution. Column (c): simulated spectral evolution. Column (d): simulated coherence evolution. The simulation plots have black lines at 1700 nm to help visual comparison with experiments. In the experiment, radiation of relative intensity lower than about -40 dB was not measurable due to the sensitivity limitation; and in the simulations this part of radiation was also ignored. (e) and (f): spectrally-averaged coherence as functions of the average SC power. In the simulations, shot noise and 5% pulse-to-pulse power fluctuation in the pump were added. In (a), the color bars for the 10.5-cm and the 4.7-mm cases are omitted for clarity, and can be found in Fig. 5.1. In (b)–(d), each color bar works for three plots in the column.

The simulated and the experimental coherence show qualitative agreement which confirms the association between coherence degradation and soliton fission. There is

some discrepancy, primarily in the extent and rate of degradation. For the short-fiber (4.7 and 3.9 mm) cases, the experiments show quicker degradation at soliton fission than the simulations. This can be seen in the average coherence (compare Fig. 5.8 (e) with (f) , the 4.7- and 3.9-mm cases), and also in the evolution where the experiments show relatively abrupt drop of coherence starting at certain powers, whereas the simulations show coherence degradation starting earlier at the edges of bandwidth and gradually spreading to larger ranges of wavelength (compare Fig. 5.8 (b) with (d), the 4.7- and 3.9-mm cases). For the 10.5-cm-fiber case, the average coherence drops to below 0.2 after soliton fission in the experiments, while to 0.6–0.4 in the simulations (compare Fig. 5.8 (e) with (f), the 10.5-cm cases). In the evolution (compare Fig. 5.8 (b) with (d), the 10.5-cm cases), the experiments shows surviving coherence at very limited wavelengths after soliton fission, while in the simulations some coherence is maintained in the non-solitonic region and along solitons.

The pulse-to-pulse stability of spectral intensity ($-C_V$, defined in Eq. 4.2.16) and coherence ($|g|$) are both figures of merit of SC stability. They might be expected to show similar trends. $-C_V$ is related to coherence, according to the definition of coherence (Eq. 4.2.12). It has been shown that $-C_V$ has minor contribution in determining coherence [Dudley et al., 2006]. Here following simulations show that $-C_V$ has low correlation with coherence, and with the pulse-to-pulse stability of spectral phase ($|g_{PHASE}|$ defined in Eq. 4.2.15).

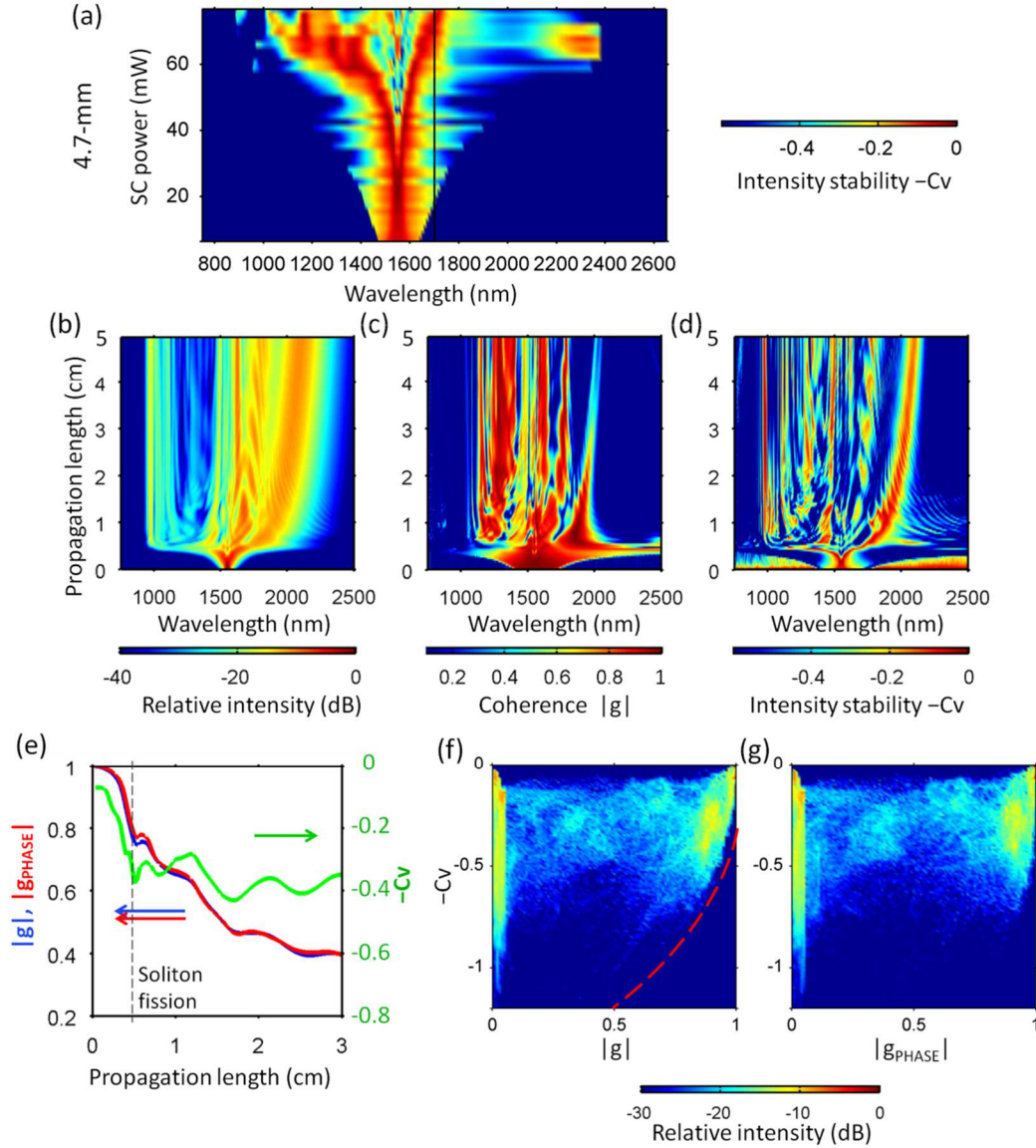


Fig. 5.9. Comparison between pulse-to-pulse stability of spectral intensity ($-Cv$) and coherence. (a) Power-dependent evolution of $-Cv$, using the 4.7-mm SF6 PCF. This can be compared with the 4.7-mm coherence evolution in Fig. 5.8 (d). (b) The spectral evolution, (c) the evolution of coherence $|g|$, and (d) the evolution of $-Cv$ depending on the propagation length, using a 5-cm SF6 PCF and an average power of 70 mW. (e) Averaged coherence $|g|$ (blue), phase stability $|g_{PHASE}|$ (red), and $-Cv$ (green) as functions of the propagation length. The soliton fission length (4.8 mm) is marked with a dashed line. (f) Distribution of SC radiation as a function of $|g|$ and $-Cv$, where the radiation at all the lengths in (b) is included. (g) Distribution of SC radiation as a function of $|g_{PHASE}|$ and $-Cv$. (g) shows low correlation between $-Cv$ and $|g_{PHASE}|$. (f) shows similar trends except for a forbidden area to the right-bottom of the dash red curve, because $-Cv$ is coupled in $|g|$.

Fig. 5.9 (a) is the power-dependent evolution of $-C_V$ using the 4.7-mm SF6 PCF. Comparisons with the corresponding coherence evolution (Fig. 5.8 (d), 4.7-mm case) show that $-C_V$ starts degrading earlier than coherence. Before soliton fission, high (nearly zero) $-C_V$ is maintained only along the pump peak and along the peaks of the two spectral lobes when the pump peak splits into these lobes. This is similar to results in the picosecond regime [Wetzel et al, 2012]. Such difference between $-C_V$ and coherence can also be seen in the evolution along the propagation length (Fig. 5.9 (c) vs. (d)), and in the average values depending on the propagation length (Fig. 5.9 (e)). Fig. 5.9 (e) also shows that $-C_V$ becomes relatively stable after soliton fission, while coherence $|g|$ and the phase stability $|g_{PHASE}|$ continue to degrade. The $|g|$ and the $|g_{PHASE}|$ curves are nearly the same, confirming that $-C_V$ plays a small role in determining coherence.

Low correlation between $-C_V$ and $|g|$ or $|g_{PHASE}|$ can be directly seen in Fig. 5.9 (f) and (g). Fig. 5.9 (g) shows low correlation between $-C_V$ and $|g_{PHASE}|$. Fig. 5.9 (f) shows similar trends except for a forbidden area to the right-bottom of the dash red curve, because $-C_V$ is coupled in $|g|$.

There is fluctuation of coherence and $-C_V$ in the regions where they start to degrade. In the experimental data, the fluctuation occurs along both the wavelength and the power axes (Fig. 5.8 (b), 3.9-mm case, below 1400 nm); in the simulations, it occurs along the power axis (Fig. 5.8 (d), 4.7- and 3.9-mm cases, and Fig. 5.9 (a)). The fact that it occurs in both experiments and simulations indicates that it is not due to experimental errors. Rather, it should be due to the randomness of the noise, which occurs both in experiments and in simulations.

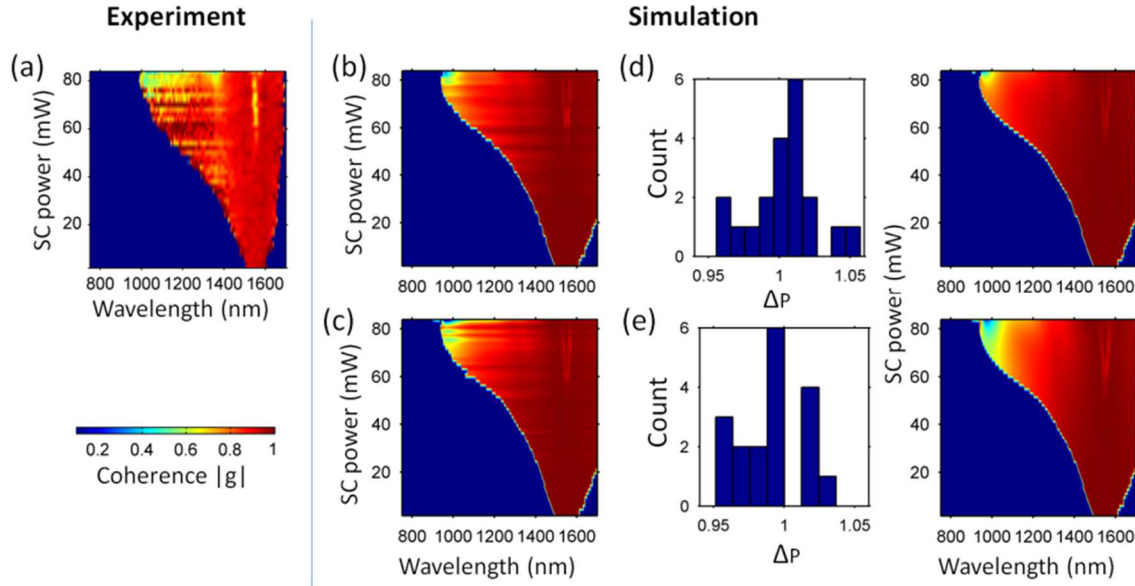


Fig. 5.10 (a) Measured coherence evolution of the 3.9-mm-fiber case. (b) Simulated coherence with independent noise at each power, including shot noise and pump power fluctuation ΔP . (c) Simulation result by fixing shot noise (meaning using the same shot noise at each power). (d) and (e) are two runs of simulation by fixing ΔP (meaning using the same set of ΔP at each power). (d) and (e) use two random sets of ΔP (as in the histograms) and thus have different coherence. These results show that the randomness of ΔP is the cause of the coherence fluctuation.

Specifically, in the simulations, each level of power uses a different set of noise seeds, including shot noise and pump power fluctuation ΔP . The effect of such configuration can be tested by “fixing” the noise, namely using the same set of noise for all powers. When shot noise is fixed (Fig. 5.10 (c)), there is still fluctuation of coherence. When the pump power fluctuation (ΔP) is fixed (Fig. 5.10 (d) and (e)), the coherence fluctuation disappears. Different sets of ΔP (shown in the histograms) yield different degradation of coherence. These results show that random ΔP is the cause of coherence fluctuation.

In the experiment, measurements were taken at one power after another, and the OSA measured spectra by scanning through wavelengths. Thus each power and each wavelength sees a different set of ΔP , which causes coherence fluctuation along both the

power and the wavelength axes. If a grating plus a line CCD was used to measure the spectrum of all wavelengths at the same time, the coherence fluctuation along the wavelength axis should have disappeared.

Fig. 5.10 (d) and (e) show that two different sets of Δ_P yield different coherence, with a repetition of $N = 20$. When N is large, the set of N Δ_P 's will approach a normal distribution. Thus any random sets of Δ_P will be nearly the same, causing the coherence fluctuation to be negligible. In our experiment, for example, the integration time is 2 ms for each wavelength, yielding $N = 2 \text{ ms} / f_{rep} = 160,000$, which means a sum of $N = 160,000$ pulses was measured for each wavelength in the spectrum. This N is large enough so that random sets of Δ_P are nearly the same. But coherence fluctuation still exists in our experimental results. This is because each pulse interferes only with the next one in the experiment:

$$|g_{12}(\omega)|_{\text{exp}} = \left| \left\langle \tilde{A}_m^*(\omega) \tilde{A}_{m+1}(\omega) \right\rangle_{m=1,2,\dots,N-1} \right| / \left| \left\langle |\tilde{A}_m(\omega)|^2 \right\rangle_m \right| \quad (5.1.2),$$

unlike in the simulations where each pulse interferes with all others (Eq. 4.2.12). So the experimental coherence actually depends on the sequence of Δ_P . This sequence is random, independent of how large N is, which causes the fluctuation of coherence in the experiments.

The fluctuation of $-C_V$ (Fig. 5.9 (a)) can be explained similarly.

5.1.4 Conclusions

Experimentally measured spectral and coherence evolution of SC generated in different lengths of SF6 PCFs are presented. Numerical simulations were carried out to match the measurements. The following conclusions can be drawn.

(1) Spectral evolution contains a wealth of data, allowing for detailed comparison between simulation and measurement. The simulations can be optimized to match measurements by iteratively tuning parameters and comparing features. It is demonstrated that, given a spectral evolution, the fiber length, and the average power of SC, all other parameters can be determined unambiguously, and the spectral evolution can be reproduced in simulations. The soliton fission length or power was used as the primary criterion, and was reproduced quantitatively. Such optimization allows parameters to be estimated, and avoids experimentally measuring them.

(2) The simulated and the measured coherence show qualitative agreement, both confirming that coherence degradation is associated with soliton fission. There is some discrepancy, mostly in the extent and rate of degradation.

Coherent SC was generated experimentally using fibers slightly shorter than the soliton fission length, with little sacrifice in the bandwidth. This is a relatively easy way to enhance coherence, compared to other ways, e.g., using shorter pump pulses, or redesigning dispersion properties [Chen et al., 2009; Hooper et al., 2011].

(3) Simulations show that the stability of spectral intensity has different dynamics than coherence. Being two figures of merit of SC stability, they have low correlation.

(4) The measurements and the simulations both show fluctuation of coherence and spectral intensity stability, in the regimes where they start to degrade. It is shown that this is caused by random pulse-to-pulse fluctuation of the pump power.

5.2 Using Tellurite PCF

5.2.1 Experimental data

Fig. 5.11 (a) shows the measured spectral evolution of the SC generated in the 2.7-cm highly nonlinear tellurite PCF. It shows a soliton-fission-dominated pattern with Raman-induced red shift of the solitons and Cherenkov radiation at the blue edge. As expected, it is similar to the 10.5-cm SF6 PCF case (Fig. 5.1 (a)), except for an earlier soliton fission.

The coherence properties are shown in Fig. 5.11 (b) and (c). The overall coherence is high ($> \sim 0.9$) before soliton fission (~ 2 mW), and degrades quickly after that. In contrast, the solitonic region (> 1550 nm) has slow linear-like degradation of coherence, which is less sensitive to soliton fission. More details can be seen in Fig. 5.11 (d) and (e), where a longer temporal delay in the interferometer was used to yield shorter periods in the interferometric fringes (see Eq. 2.4.13), thus allowing higher resolutions in wavelength in the coherence evolution. Traces of high coherence can be seen to follow corresponding soliton trajectories (marked with arrows 1–7). Only small degradation of coherence occurs at the solitons when the power increases (along y axis). At around 32 mW of Fig. 5.11 (d) and (e), the data have an interruption due to disturbance of the alignment in the experiment. But this does not affect the trends we discuss about.

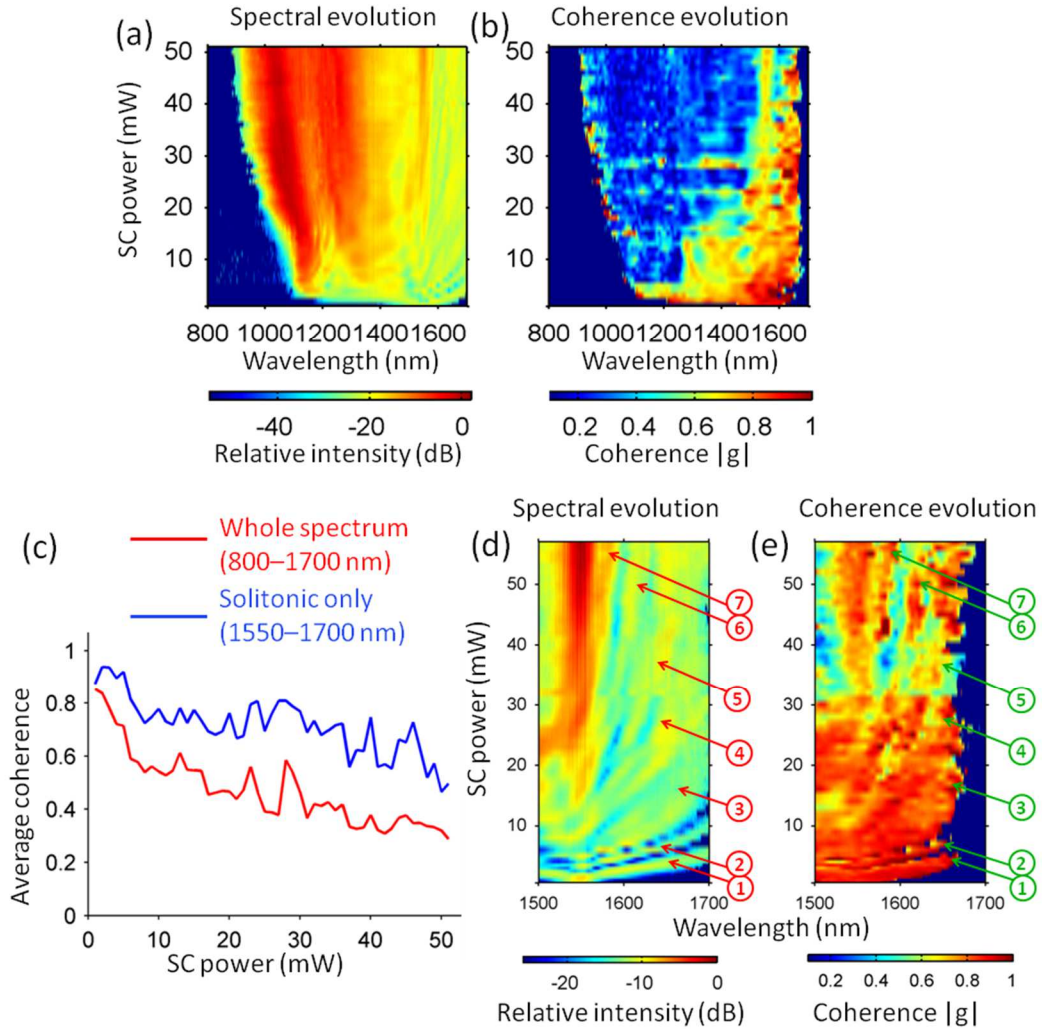


Fig. 5.11. (a), (b): Measured spectral and coherence evolution of SC generated in a 2.7-cm tellurite PCF. (c) Spectrally-averaged coherence of the whole measured spectrum (800–1700 nm, red curve) and of the solitonic region (1550–1700 nm, blue curve). (d), (e): Closeup spectral and coherence evolution for the solitonic region. Solitons and corresponding high-coherence traces are marked with arrows (1–7). Each pair of arrows is placed at the same places in the plots, showing the correspondence between the solitons and the high-coherence traces.

5.2.2 Simulated spectral evolution and discussions

The measured spectral evolution (Fig. 5.11 (a)) covers a wavelength range of ~900–1700 nm. Since the reported dispersion curve covers only 1000–1600 nm [Domachuk et al.,

2008], estimation of the dispersion over a broader bandwidth is needed. The dispersion curve for the whole SC span (about 900–5500 nm) can be estimated based on a complete SC spectrum (Fig. 5.12 (a)) generated in an 8-mm piece of the same tellurite PCF [Domachuk et al., 2008].

As in Fig. 5.12 (b), the corner region of the dispersion curve (1600–2200 nm) was empirically estimated, and the remaining parts were modeled to be linear ($\lambda < 1300$ nm and > 2200 nm). Tuning the slopes of the linear parts causes wavelength shifting in some peaks in the spectrum (e.g., see red arrows in Fig. 5.12 (b) and (c)). The slopes were optimized (Fig. 5.12 (d)) by simply matching the reddest (~ 900 nm) and the bluest (~ 4700 nm) spectral peaks between simulation and experiment (Fig. 5.12 (e) red arrows). As a result, the simulated spectrum agrees with the measured one well in most features (e.g., see green arrows in Fig. 5.12 (e)). The simulated spectrum has deeper valleys than the measured one, because the measured one is an average and also has a lower resolution in wavelength.

Using the dispersion curve above, the spectral evolution was simulated for the 2.7-cm tellurite PCF (Fig. 5.13). The average SC power P was tuned to $1.4*P$ to match the measured results, which indicates a collimation loss of 29% in the experiment. The simulations agree with the experimental results well, especially in the soliton fission power. Both show the first soliton occurring at about 3 mW, and Cherenkov radiation emerging at about 3 mW at about 1100 nm.

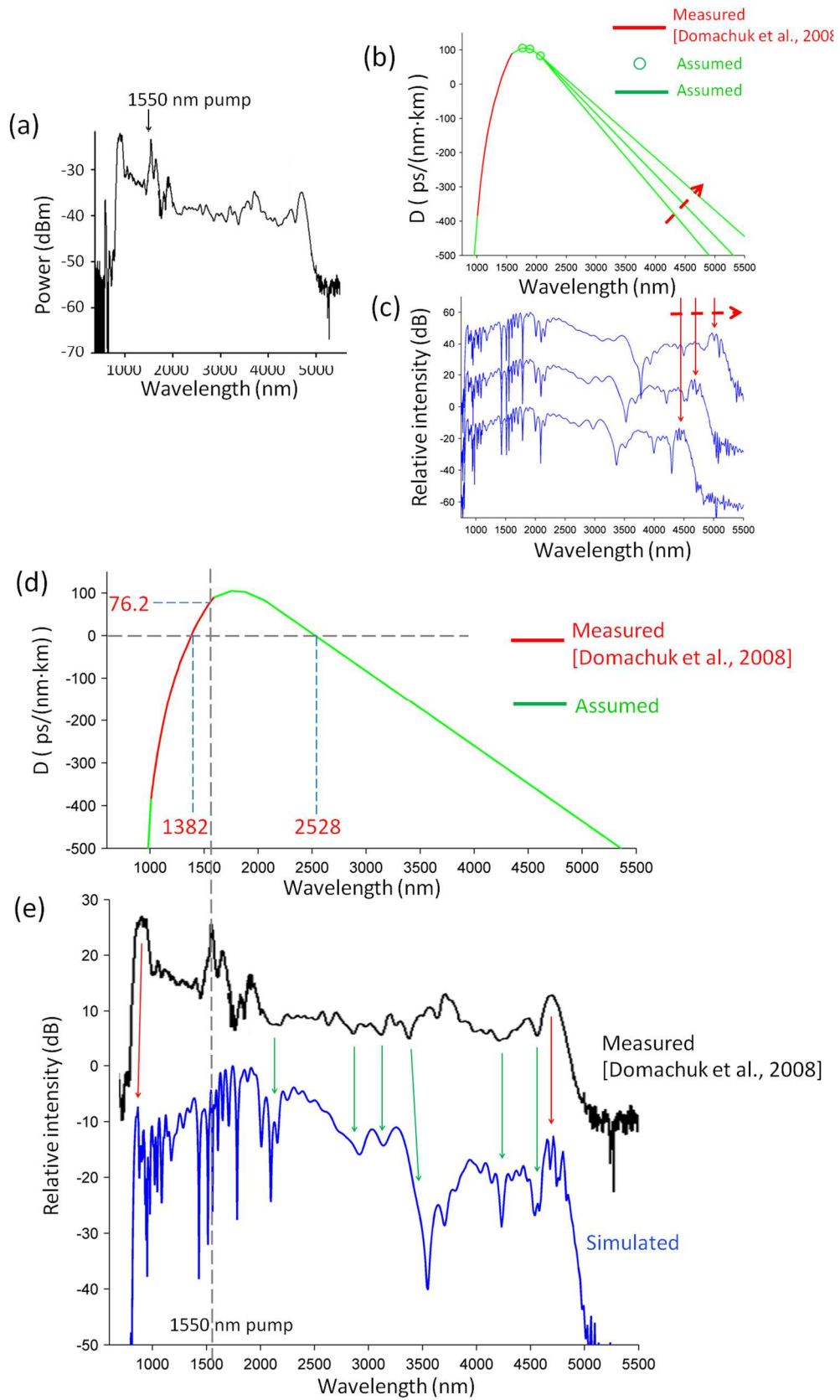


Fig. 5.12. Optimization of the simulated SC spectrum by tuning the dispersion. (a) Measured SC spectrum, excerpted from [Domachuk et al., 2008]. 8-mm tellurite PCF was used. (b) Tests with varying slopes in the dispersion curve. The red-color part of the curve was experimentally measured [Domachuk et al., 2008]. The green circles mark estimated corner part (1600–2200 nm). The remaining parts were assumed to be linear (green lines). (c) Simulated SC spectra using the dispersion curves in (b). Changing the slopes of the linear parts in the dispersion in (b) causes wavelength shift of some spectral peaks in (c) (see red arrows). (d) The dispersion curve for the optimized spectrum in (e). The dispersion at the pump wavelength is 76.2 ps/(nm·km). ZDWs are 1382 and 2528 nm. (e) Measured SC spectrum [Domachuk et al., 2008] vs. the optimized simulation using the dispersion curve in (d). The criterion of optimization is matching the reddest (~900 nm) and the bluest (~4700 nm) peaks between simulation and experiment, respectively. These two peaks are marked with red arrows. Green arrows mark some of the spectral features that match.

At the maximum average power $P = 51 \times 1.4$ mW, spectral and temporal evolution along the propagation length (not plotted here) shows a soliton fission length $L_{fiss} = \sim 3$ mm. Analytical calculation yields $L_{fiss} = 3.6$ mm and a soliton number $N = 11$. So to generate SC based on almost pure SPM (similar to the cases of 3.9- and 4.7-mm SF6 PCFs), a 3–4-mm-long tellurite PCF should be used.

There are some minor mismatches in the wavelengths of the solitons and the Cherenkov radiation. Considering the Raman-induced frequency shift of solitons $\Omega \propto |\beta_2|z/T_0^4$ in which T_0 is the duration of solitons, inaccuracy in T_0 should be the dominant source of error. The wavelength of Cherenkov radiation is determined by phase matching with solitons; therefore, errors in the soliton wavelengths and inaccuracy of the dispersion curve should be responsible for the mismatches in the Cherenkov radiation wavelengths. The measured spectral evolution has an overall slope in intensity vs. wavelength, where shorter wavelengths are in general brighter than longer wavelengths. This is potentially due to alignment errors.

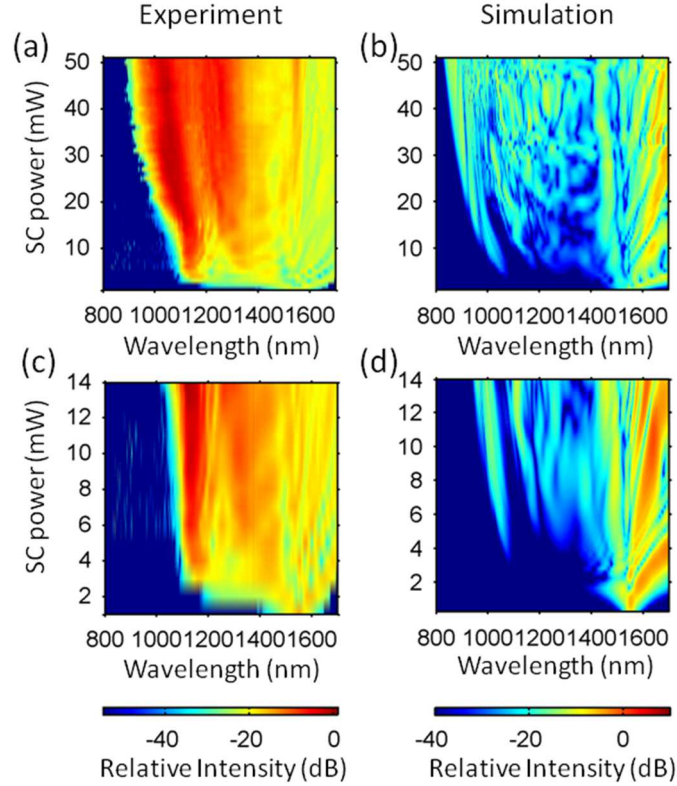


Fig. 5.13. Comparison of (a), (c) measured and (b), (d) simulated spectral evolution using the 2.7-mm tellurite PCF. (c) and (d) are closeups of the beginning (low SC power) stage, showing the first a few solitons and the emergence of the Cherenkov radiation. The lower and the upper limits of the color bars are set for visualization of features.

5.2.3 Simulated coherence evolution and discussions

Simulated coherence evolution is plotted in Fig. 5.14. (f) and (h). Simulated spectral evolution and measured results are also plotted here for comparison. The simulated coherence (Fig. 5.14. (f)) shows similar trends as the measured (Fig. 5.14. (b)), that low coherence firstly occurs in the Cherenkov radiation and then spreads over the non-solitonic region. In the solitonic region, the simulations (Fig. 5.14. (h)) also show high-coherence traces following the soliton trajectories (Fig. 5.14. (g)) (marked with arrows A–E), as the measurements do (Fig. 5.14. (d)).

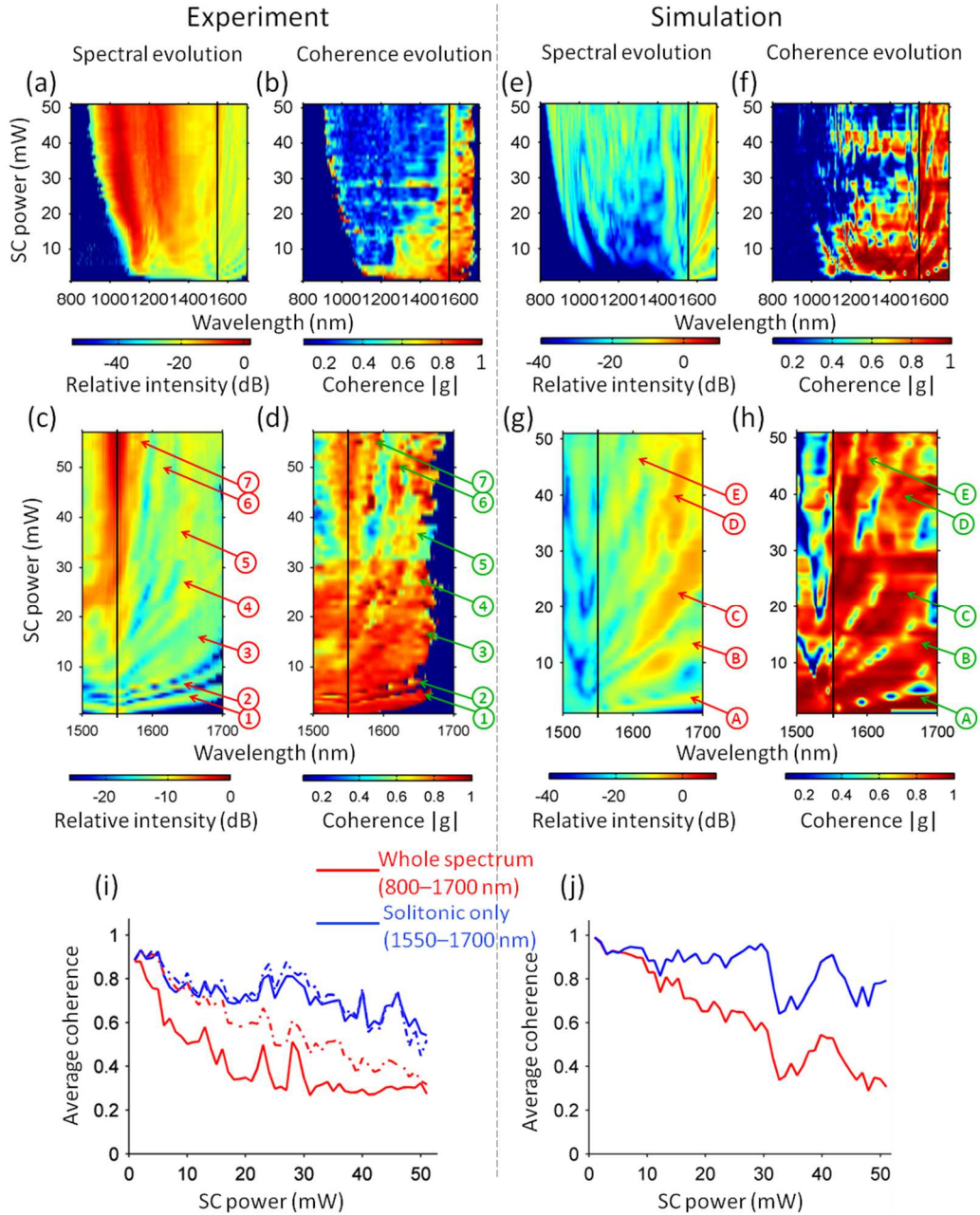


Fig. 5.14. (a)–(d) Measured and (e)–(h) simulated spectral and coherence evolution of SC generated in the 2.7-cm tellurite PCF. The plots in the second line ((c), (d), (g), and (h)) are closeups of the solitonic region (1550–1700 nm). The pump wavelength is marked with black lines. Arrow pairs 1–7 and A–E mark soliton trajectories (in (c) and (g)) and corresponding high-coherence traces (in (d) and (h)). (i) and (j) show spectrally-averaged coherence of the whole measured spectrum (800–1700 nm, red curves) and of the solitonic region (1550–1700 nm, blue curves). The dashed curves in (i) show average coherence based on the measured coherence and the simulated spectra. Shot noise and 5% pulse-to-pulse power fluctuation in the pump were used in the simulations.

The solid curves in Fig. 5.14. (i) and (j) show measured and simulated spectrally-averaged coherence, respectively. The measured and the simulated spectra have major difference in the energy fraction of the low-coherence Cherenkov radiation, which can cause difference in the average coherence, even if the coherence properties are the same between experiment and simulation. To rule out this factor, average coherence based on the measured coherence and the simulated spectra is used to quantify the measured coherence (dashed curves in Fig. 5.14. (i)). After this calibration, the dashed curves in Fig. 5.14. (i) show approximately linear degradation, similar to the simulations in Fig. 5.14. (j). Comparisons between the solid and the dashed curves in Fig. 5.14. (i) show that the fast drop in the solid red curve at 0–20 mW is due to the bright Cherenkov radiation in the measured SC spectra.

Standard deviation of the fluctuation in the pump power was tuned to control the coherence degradation in the simulations. Based on the criterion of matching the average coherence of the whole spectrum at the maximum power, 5% fluctuation was chosen such that the dashed red curve in Fig. 5.14. (i) and the red curve in (j) both arrive at ~ 0.3 at the maximum power.

Simulated coherence of the spectrum up to $5 \mu\text{m}$ is plotted in Fig. 5.15. The red-shifted Cherenkov radiation maintains some coherence, while the blue-shifted Cherenkov radiation completely loses its coherence. This is interesting, because the blue-shifted and the red-shifted Cherenkov radiation are generated based on the same mechanism. They are both phase-matched to the solitons, and are supposed to show same coherence properties.

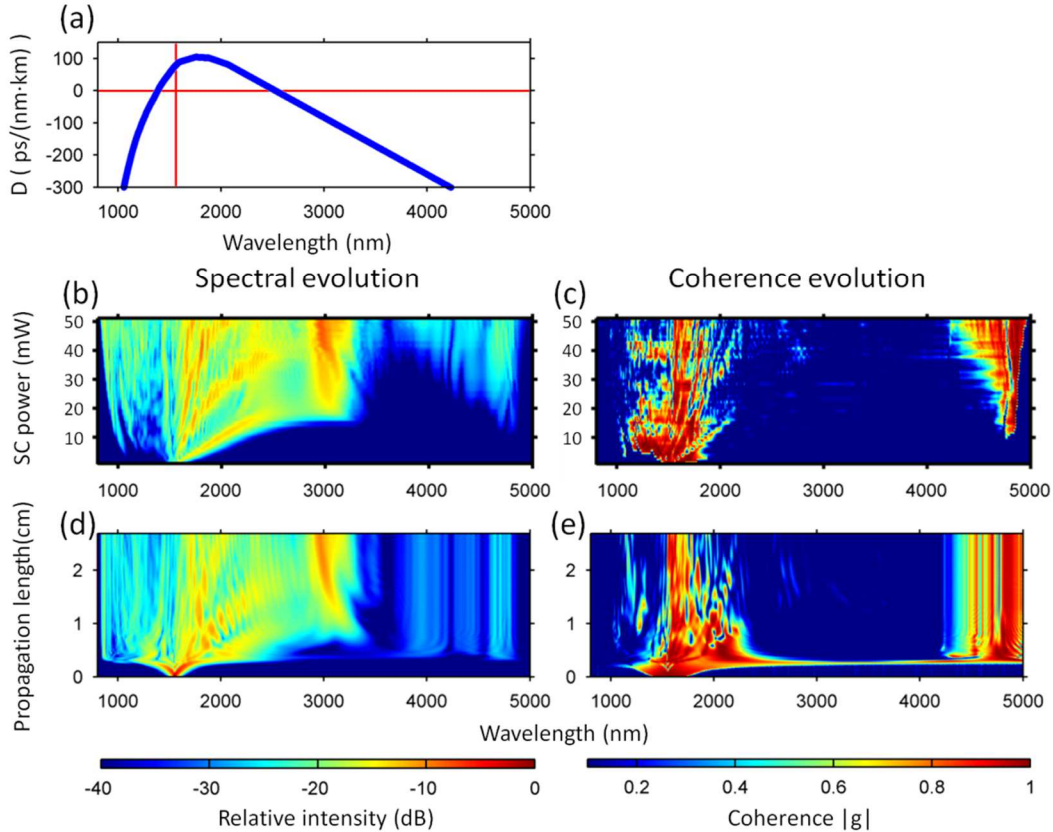


Fig. 5.15. Simulated spectral and coherence evolution of SC generated in a 2.7-cm tellurite PCF. (a) is a reminder of the GVD. (b) and (c) are evolution depending on the SC power. (d) and (e) are evolution depending on the propagation length ($P = 71.4\text{ mW}$). Shot noise and 5% fluctuations of the pump power were added.

There have been some studies of the coherence of the Cherenkov radiation (usually blue-shifted). With shot noise alone, the Cherenkov radiation tends to maintain higher coherence than most parts of the spectrum [see Dudley et al., 2006, Fig. 20 (a)]. With shot noise and pump power fluctuation, it suffers coherence degradation immediately after soliton fission (e.g., see Fig. 5.15). [Kobtsev et al., 2005] explained that, there are fine spectral fringes (period $\Delta\omega = 0.5\text{--}1\text{ Hz}$) in the non-solitonic regime. These fringes shift depending on fluctuation of the pump power, and the lack of spectral overlapping causes coherence degradation. [Türke, et al., 2007] explained that each Cherenkov peak interacts with the sum of all solitons through XPM. The sum of all solitons has

interference which changes when the pump power fluctuates, causing coherence degradation in the Cherenkov radiation.

These theories do not explain the results in Fig. 5.15, where the red-shifted Cherenkov radiation has higher coherence than the blue-shifted, although they are pumped by the same solitons. Investigation of the actual cause will be a subject of future work.

5.2.4 Conclusions

In summary, this section presents measured and simulated spectral and coherence evolution of SC generated in a 2.7-cm tellurite PCF. Major conclusions are as follows:

(1) The measured spectral evolution shows a soliton-fission-dominated pattern. Raman-induced red shift in the solitons and the generation of Cherenkov radiation are seen. The evolution has a very quick initial broadening and early soliton fission, due to the high nonlinearity of the fiber.

After optimization, the simulated spectral evolution shows good agreement with the measurements. The unknown part of the dispersion curve was determined based on a SC spectrum generated in an 8-mm-long piece of the same Tellurite PCF [Domachuk et al., 2006].

(2) The measured and the simulated coherence show nearly quantitative agreement. The average coherence of the whole measured spectrum (800–1700 nm) has approximately

linear degradation as a function of the average power, whereas that of the solitonic region (1500–1700 nm) shows considerably slower degradation.

The measured and the simulated coherence evolution show coherence degradation firstly occurring at the Cherenkov radiation and then spreading over the non-solitonic region. There are high-coherence traces following the soliton trajectories.

(3) Simulations show that the red-shifted Cherenkov radiation is less vulnerable to coherence degradation than the blue-shifted Cherenkov radiation.

6. CONCLUSIONS AND OUTLOOK

In this dissertation, experimentally measured spectral and coherence evolution of SC was presented, and numerical simulations based on the GNLSE were performed to match the experimental results. Highly nonlinear soft-glass PCFs were used for SC generation, including a lead-silicate (Schott SF6) PCF and a tellurite PCF. Different lengths of the SF6 PCF were used to investigate the dependence of coherence on the fiber length. The pump is at 1550 nm, with pulse energy in the order of nJ and duration of 105 fs. The coherence of SC was measured using the delayed-pulse method.

Spectral evolution shows rich features which allow for detailed comparison between measurement and simulation. Simulated spectral evolution was optimized by iteratively tuning parameters and comparing features with experimental data. It was demonstrated in principle that, given a spectral evolution, the fiber length, and the average power of SC, all other parameters can be determined unambiguously through the optimization, and the spectral evolution can be reproduced in simulations. Most importantly, the soliton fission length or power was reproduced quantitatively. Such optimization allows avoiding experimental measurement of some parameters.

For the coherence evolution of SC generated in different lengths of SF6 PCFs, the measurements and the simulations show qualitative agreement which confirms the association between coherence degradation and soliton fission. Using fibers slightly shorter than the soliton fission length, coherent SC was generated with little sacrifice in the bandwidth. This is a relatively easy way to enhance coherence, compared to others

such as using shorter pump pulses or redesigning the dispersion [Chen et al., 2009; Hooper et al., 2011].

Besides coherence, the pulse-to-pulse stability of spectral intensity is another characterization of SC stability. It is shown by simulations that it has different dynamics than coherence, and has low correlation with the latter.

Some fluctuation of coherence and the pulse-to-pulse stability of spectral intensity occurs in both the measurements and the simulations. It is shown to be a result of the pulse-to-pulse power fluctuation in the pump.

For the coherence of the SC generated in the tellurite PCF, the measurements and the simulations show nearly quantitative agreement. The average coherence of the whole measured spectrum (800–1700 nm) has approximately linear degradation as a function of the average power, whereas that of the solitonic region (1500–1700 nm) shows considerably slower degradation. The measured and the simulated coherence evolution show coherence degradation firstly occurring at the Cherenkov radiation and then spreading over the non-solitonic region. There are high-coherence traces following the soliton trajectories.

Some interesting issues are not fully solved, and will be subjects of future research.

(1) There are some discrepancies between measurement and simulation. In the spectral evolution of both the SF6- and the tellurite-PCF cases, there are discrepancies in the wavelengths of the Cherenkov radiation, and in the trajectories of solitons (see Fig. 5.8 (a) vs. (c), and Fig. 5.13 (a) and (c) vs. (b) and (d)).

In the coherence results using the SF6 PCFs, the measurements typically show faster or greater degradation than the simulations for the 4.7-mm- and the 10.5-cm-fiber cases, whereas there is good agreement for the 3.9-mm-fiber case (see Fig. 5.8 (b) vs. (d) and (e) vs. (f)). Investigating the cause of these discrepancies and fixing them will be a future subject.

(2) In the optimization of the simulated spectral evolution, manual comparison was implemented between measurement and simulation. In future research, a cost function should be developed to quantify the match of features, and then iterative optimization can be easily implemented by computer. Sophisticated tuning of parameters can be added, for example tuning the shape of the dispersion curve. This should help fixing some of the discrepancies in (1).

(3) Simulations also show that the red-shifted Cherenkov radiation has different coherence properties than the blue-shifted Cherenkov radiation. Considering the blue-shifted and the red-shifted Cherenkov radiation are generated based on the same mechanism, the cause of this difference is an interesting topic to investigate. To consider this question in broader view, I am interested in investigating how the specific coherence at each wavelength or in each component of SC is determined.

REFERENCES

- Aber, Janice E., Maurice C. Newstein, and Bruce A. Garetz. "Femtosecond optical Kerr effect measurements in silicate glasses." *JOSA B* 17.1 (2000): 120–127.
- Akhmediev, Nail, and Magnus Karlsson. "Cherenkov radiation emitted by solitons in optical fibers." *Physical Review A* 51.3 (1995): 2602–2607.
- Agrawal, G. P., *Nonlinear Fiber Optics*, 4th edition, Academic Press, 2006.
- Alfano, R. R., *The Supercontinuum Laser Source*, 2nd edition, Springer, 2005.
- Alfano, R. R., and S. L. Shapiro. "Emission in the region 4000 to 7000 Å via four-photon coupling in glass." *Physical Review Letters* 24 (1970a): 584–587.
- Alfano, R. R., and S. L. Shapiro. "Observation of self-phase modulation and small-scale filaments in crystals and glasses." *Physical Review Letters* 24 (1970b): 592–594.
- Born, M. and E. Wolf, *Principles of Optics: Electromagnetic Theory of Propagation, Interference and Diffraction of Light*, 7th edition, Cambridge University Press, 1999.
- Bellini, Marco, and Theodor W. Hänsch. "Phase-locked white-light continuum pulses: toward a universal optical frequency-comb synthesizer." *Optics Letters* 25.14 (2000): 1049–1051.
- Birks, Tim A., Jonathan C. Knight, and P. St J. Russell. "Endlessly single-mode photonic crystal fiber." *Optics Letters* 22.13 (1997): 961–963.
- Birks, T. A., W. J. Wadsworth, and P. St J. Russell. "Supercontinuum generation in tapered fibers." *Optics Letters* 25.19 (2000): 1415–1417.
- Chen, Zhigang, Antoinette J. Taylor, and Anatoly Efimov. "Coherent mid-infrared broadband continuum generation in non-uniform ZBLAN fiber taper." *Optics Express* 17.7 (2009): 5852–5860.
- Cherif, R., et al. "Supercontinuum generation by higher-order mode excitation in a photonic crystal fiber." *Optics Express* 16.3 (2008): 2147–2152.
- Corwin, K. L., et al. "Fundamental noise limitations to supercontinuum generation in microstructure fiber." *Physical Review Letters* 90.11 (2003): 113904.
- Cundiff, Steven T., and Jun Ye. "Colloquium: Femtosecond optical frequency combs." *Reviews of Modern Physics* 75.1 (2003): 325.
- Doke, J., "GRABIT", A MATLAB application to retrieve data from curves in an image. < <http://www.mathworks.com/matlabcentral/fileexchange/7173-grabit> > (2007).

- Domachuk, P., et al. "Over 4000 nm bandwidth of mid-IR supercontinuum generation in sub-centimeter segments of highly nonlinear tellurite PCFs." *Optics Express* 16.10 (2008): 7161–7168.
- Drummond, P. D., and Joel Frederick Corney. "Quantum noise in optical fibers. I. Stochastic equations." *JOSA B* 18.2 (2001): 139–152.
- Dudley, J. M. and J. R. Taylor, *Supercontinuum Generation in Optical Fibers*, 1st edition, Cambridge University Press, 2010.
- Dudley, J. M., and S. Coen. "Coherence properties of supercontinuum spectra generated in photonic crystal and tapered optical fibers." *Optics Letters* 27, 13 (2002): 1180–1182.
- Dudley, J. M., and S. Coen. "Fundamental limits to few-cycle pulse generation from compression of supercontinuum spectra generated in photonic crystal fiber." *Optics Express* 12. 11 (2004): 2423–2428.
- Dudley, John M., Goëry Genty, and Stéphane Coen. "Supercontinuum generation in photonic crystal fiber." *Reviews of Modern Physics* 78.4 (2006): 1135.
- Genty, Goëry, Stéphane Coen, and John M. Dudley. "Fiber supercontinuum sources." *JOSA B* 24.8 (2007): 1771–1785.
- Genty, Goëry, et al. "Complete characterization of supercontinuum coherence." *JOSA B* 28.9 (2011): 2301–2309.
- Gordon, James P. "Theory of the soliton self-frequency shift." *Optics Letters* 11.10 (1986): 662–664.
- Gu, Xun, et al. "Experimental studies of the coherence of microstructure-fiber supercontinuum." *Optics Express* 11.21 (2003): 2697–2703.
- Hasegawa, Akira, and Frederick Tappert. "Transmission of stationary nonlinear optical pulses in dispersive dielectric fibers. I. Anomalous dispersion." *Applied Physics Letters* 23.3 (1973): 142–144.
- Heidt, Alexander M., et al. "Coherent octave spanning near-infrared and visible supercontinuum generation in all-normal dispersion photonic crystal fibers." *Optics Express* 19.4 (2011): 3775–3787.
- Heidt, Alexander M., et al. "High quality sub-two cycle pulses from compression of supercontinuum generated in all-normal dispersion photonic crystal fiber." *Optics Express* 19.15 (2011): 13873–13879.
- Heiman, D., R. W. Hellwarth, and D. S. Hamilton. "Raman scattering and nonlinear refractive index measurements of optical glasses." *Journal of Non-Crystalline Solids* 34.1 (1979): 63–79.

- Hollenbeck, Dawn, and Cyrus D. Cantrell. "Multiple-vibrational-mode model for fiber-optic Raman gain spectrum and response function." *JOSA B* 19.12 (2002): 2886–2892.
- Hooper, Lucy E., et al. "Coherent supercontinuum generation in photonic crystal fiber with all-normal group velocity dispersion." *Optics Express* 19.6 (2011): 4902–4907.
- Humbert, Georges, et al. "Supercontinuum generation system for optical coherence tomography based on tapered photonic crystal fibre." *Optics Express* 14.4 (2006): 1596–1603.
- Islam, Mohammed N., et al. "Femtosecond distributed soliton spectrum in fibers." *JOSA B* 6.6 (1989): 1149–1158.
- Kalashnikov, V. L., E. Sorokin, and I. T. Sorokina. "Raman effects in the infrared supercontinuum generation in soft-glass PCFs." *Applied Physics B* 87.1 (2007): 37–44.
- Knight, Jonathan C. "Photonic crystal fibres." *Nature* 424.6950 (2003): 847–851.
- Kobtsev, S. M., et al. "Coherent, polarization and temporal properties of self-frequency shifted solitons generated in polarization-maintaining microstructured fibre." *Applied Physics B* 81.2-3 (2005): 265–269.
- Kodama, Yuji, and Akira Hasegawa. "Nonlinear pulse propagation in a monomode dielectric guide." *Quantum Electronics, IEEE Journal of* 23.5 (1987): 510–524.
- Kumar, V. V., et al. "Extruded soft glass photonic crystal fiber for ultrabroad supercontinuum generation." *Optics Express* 10.25 (2002): 1520–1525.
- Kumar, V. V., et al. "Tellurite photonic crystal fiber." *Optics Express* 11.20 (2003): 2641–2645.
- Lu, Fei, and Wayne Knox. "Generation of a broadband continuum with high spectral coherence in tapered single-mode optical fibers." *Optics Express* 12.2 (2004): 347–353.
- Moeser, Jamison T., et al. "Initial dynamics of supercontinuum generation in highly nonlinear photonic crystal fiber." *Optics Letters* 32.8 (2007): 952–954.
- Mollenauer, Linn F., Roger H. Stolen, and James P. Gordon. "Experimental observation of picosecond pulse narrowing and solitons in optical fibers." *Physical Review Letters* 45 (1980): 1095–1098.
- Newbury, N. R., et al. "Noise amplification during supercontinuum generation in microstructure fiber." *Optics Letters* 28.11 (2003): 944–946.

- Nicholson, J., and M. Yan. "Cross-coherence measurements of supercontinua generated in highly-nonlinear, dispersion shifted fiber at 1550 nm." *Optics Express* 12.4 (2004): 679–688.
- Nicholson, J. W., et al. "Coherence of supercontinua generated by ultrashort pulses compressed in optical fibers." *Optics Letters* 33.18 (2008): 2038–2040.
- Omenetto, F. G., et al. "Spectrally smooth supercontinuum from 350 nm to 3 μ m in sub-centimeter lengths of soft-glass photonic crystal fibers." *Optics Express* 14.11 (2006): 4928–4934.
- Plotnichenko, V. G., et al. "Raman band intensities of tellurite glasses." *Optics Letters* 30.10 (2005): 1156–1158.
- Price, Jonathan H.V., et al. "Mid-IR supercontinuum generation from nonsilica microstructured optical fibers." *Selected Topics in Quantum Electronics, IEEE Journal of* 13.3 (2007): 738–749.
- Qin, Guanshi, Rajan Jose, and Yasutake Ohishi. "Stimulated Raman scattering in tellurite glasses as a potential system for slow light generation." *Journal of Applied Physics* 101.9 (2007): 093109.
- Ramsay, Jacob, et al. "Generation of infrared supercontinuum radiation: spatial mode dispersion and higher-order mode propagation in ZBLAN step-index fibers." *Optics Express* 21.9 (2013): 10764–10771.
- Ranka, Jinendra K., Robert S. Windeler, and Andrew J. Stentz. "Visible continuum generation in air-silica microstructure optical fibers with anomalous dispersion at 800 nm." *Optics Letters* 25.1 (2000): 25–27.
- Reeves, William, et al. "Demonstration of ultra-flattened dispersion in photonic crystal fibers." *Optics Express* 10.14 (2002): 609–613.
- Russell, Philip. "Photonic crystal fibers." *Science* 299.5605 (2003): 358–362.
- Russell, Philip St J. "Photonic-crystal fibers." *Journal of Lightwave Technology* 24.12 (2006): 4729–4749.
- Schenkel, Birgit, Rüdiger Paschotta, and Ursula Keller. "Pulse compression with supercontinuum generation in microstructure fibers." *JOSA B* 22.3 (2005): 687–693.
- Shabat, A., and V. Zakharov. "Exact theory of two-dimensional self-focusing and one-dimensional self-modulation of waves in nonlinear media." *Soviet Physics JETP* 34 (1972): 62–69.
- Skryabin, D. V., et al. "Soliton self-frequency shift cancellation in photonic crystal fibers." *Science* 301.5640 (2003): 1705–1708.

- Stegeman, G. I., et al. "Glasses for Raman nonlinear optics." *Laser Physics* 16.6 (2006): 902–910.
- Stolen, Roger H., W. J. Tomlinson, and L. F. Mollenauer. "Observation of pulse restoration at the soliton period in optical fibers." *Optics Letters* 8.3 (1983): 186–188.
- Tao, Guangming, Alexander M. Stolyarov, and Ayman F. Abouraddy. "Multimaterial fibers." *International Journal of Applied Glass Science* 3.4 (2012): 349–368.
- Türke, D., et al. "Coherence of subsequent supercontinuum pulses generated in tapered fibers in the femtosecond regime." *Optics Express* 15.5 (2007): 2732–2741.
- Udem, Th, R. Holzwarth, and Theodor W. Hänsch. "Optical frequency metrology." *Nature* 416.6877 (2002): 233–237.
- Wetzel, B., et al. "Real-time full bandwidth measurement of spectral noise in supercontinuum generation." *Scientific Reports* 2 (2012).
- Yan, Xin, et al. "Transient Raman response and soliton self-frequency shift in tellurite microstructured fiber." *Journal of Applied Physics* 108.12 (2010): 123110.
- Zeylikovich, Iosif, Vladimir Kartzaev, and R. R. Alfano. "Spectral, temporal, and coherence properties of supercontinuum generation in microstructure fiber." *JOSA B* 22.7 (2005): 1453–1460.

APPENDIX A. SYSTEMATIC CHECK OF NUMERICAL SIMULATIONS

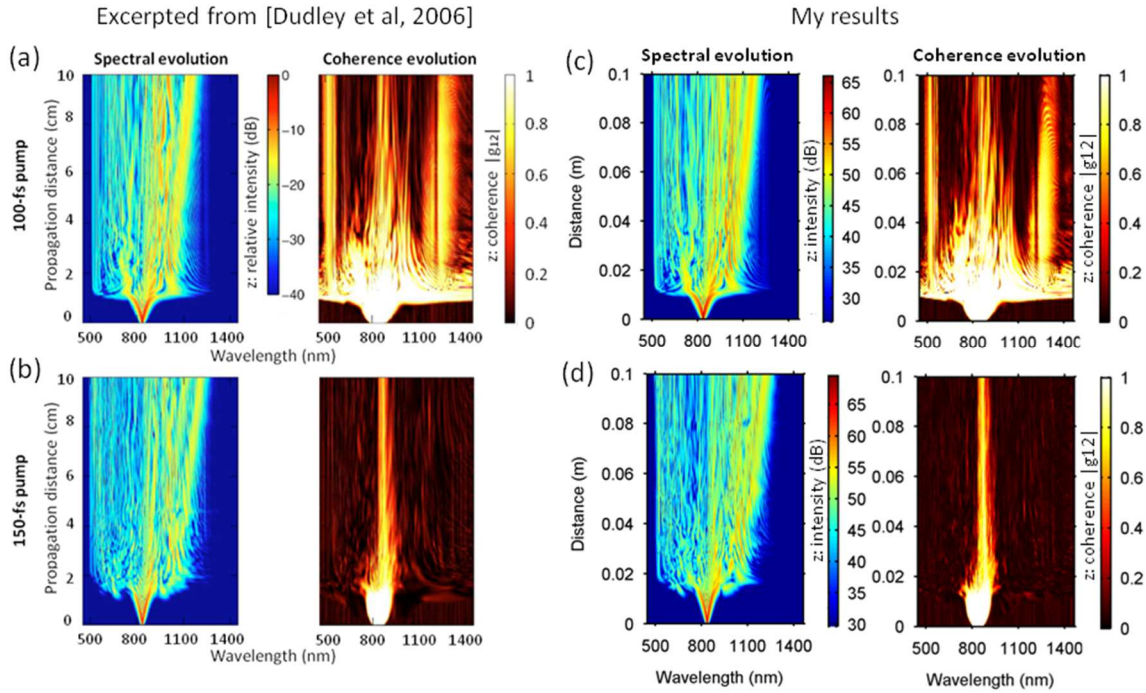


Fig. A.1 A systematic check of the simulations of SC and its coherence. (a) and (b) are results excerpted from [Dudley et al., 2006]. (c) and (d) are my results using the same parameters.

Fig. A.1 shows a systematic check of my simulation methods. (a) and (b) are results excerpted from [Dudley et al., 2006]. (c) and (d) are my results using the same parameters. My results agree with those in the literature.

APPENDIX B. PARAMETERS FOR SIMULATIONS IN SECTION 2.3

The following parameters are invariant for all the simulations in Section 2.3.

The pump wavelength is $\lambda_0 = 1500$ nm. The pump pulse duration is $T_{FWHM} = 105$ fs. The average power of pump, which is also average output power because loss is not considered here: $P_{ave} = 70$ mW.

The nonlinearity of the fiber is $\gamma = 100$ /km·W. The fiber length is $L_{fiber} = 4.82$ cm. This length was chosen so that Fig. 2.1 (b) shows two soliton periods.

The parameters in the Raman response function are: $\tau_1 = 5.5$ fs, $\tau_2 = 32$ fs (see Eq. 2.2.61).

The parameters of different values in each simulation in Section 2.3 are listed in Table B.1.

Fig.	$\beta_2(\omega_0)$ (ps ² /km)	$\beta_3(\omega_0)$ (ps ³ /km)	f_R	N
2.1 (a)	100	0	0	N.A.
2.1 (b)	-289	0	0	3
2.1 (c)	-2601	0	0	1
2.2 (a)	-212	0	0.1	3.5
2.2 (b)	-212	0.3	0.1	3.5

Table B.1 Parameter values for each simulation in Fig. 2.1 and 2.2.

APPENDIX C. COMPUTER CODE FOR DATA PROCESSING AND NUMERICAL SIMULATIONS

The computer code for data processing and numerical simulations is written in Matlab. All code including 7 functions is combined in the pdf file attached, where the function names are at the header of each page.

‘SC_sim_main.m’ simulates SC generation based on the generalized nonlinear Schrödinger equation, and then calculates its coherence. Most parameters are defined in this function, and then ‘SC_sim_calculate.m’ is called to perform calculation. These two files are modified from the original code by J. C. Travers, M. H. Frosz, and J. M. Dudley (2009) at www.scgbook.info. See Section 2.2 for details.

‘plot_evolution_1.m’ and ‘plot_evolution_as_experiment.m’ plot spectral and coherence evolution. The latter one draws plots in a style the same as the experimental data. For example, the wavelength limit is set to be within 650 to 1700 nm which is the limit in my experiment, and the power is set to be same as in experimental data.

‘Raman_calculation_main.m’ calculates the Raman response function $h_R(t)$ and the Raman fraction f_R , based on the Raman gain spectrum $g_R(\omega)$. ‘Raman_cal.m’ is called to perform the calculation. See Section 2.2.3 and 2.4.3 for details.

‘SC_data_processing_get_coherence_evolution_n_spectral_evolution.m’ performs data processing. Spectral and coherence evolution was calculated based on short-arm spectrum, long-arm spectrum, and interferometric spectrum. See Section 4.1 for details.